Geochronology, Isotope Geochemistry, and Molybdenum Distribution in the Central African Copperbelt: Examples from Chibuluma West, Kamoa, and Kipushi

by

Samuel Bowman

A thesis submitted in partial fulfilment of the requirements for the degree of

Master of Science

Department of Earth and Atmospheric Sciences
University of Alberta

© Samuel Bowman, 2018

Abstract

The Chibuluma West, Kamoa, and Kipushi stratiform deposits of the Central African Copperbelt have been evaluated using a series of geochemical techniques to better constrain the timing and origin of these deposits, with relevance to the origin of the Copperbelt as a whole. Petrographic, isotopic (Os, Pb, and O), and Mo distribution analyses have determined four mineralization events, occurring before, during, and after the Lufilian orogeny.

A possible preenrichment event occurred throughout deposition of the Sturtian glaciation. The glacier scoured and carried U-rich lithic clats from the basement before depositing the Grand Conglomerate (host rock of Kamoa deposit). Radiogenic lead is likely the cause of apparent diagenetic model lead ages for other deposits throughout the Central African Copperbelt.

The second mineralization event occurred during the Lufilian orogeny. The Chibuluma West and Kamoa deposits experienced the majority of ore mineralization ~550 to 540 Ma and ~510 to 480 Ma respectively. The Kamoa deposit is unfolded and unmetamorphosed, allowing the true age of the stratiform mineralization to be placed in the late stage of the Lufilian orogeny. The ores of these deposits were likely sourced from the crust.

The third mineralization event occurred after the Lufilian orogeny. The ores of the Kipushi deposit mineralized <430 Ma. A new geothermometric approach, using oxygen diffusion in syn-ore dolomite has been successfully shown to estimate fluid temperatures. The ore fluid for the Kipushi deposit is constrained to temperatures between 350°C to 500°C, and over a time less than or equal to 10 Ma.

A fourth and final mineralization event occurred in the Late Paleozoic ~ 330 to 300 Ma at the Kamoa and Kipushi deposits. Some amount of ore must have mineralized at this time, as model Pb ages are equivalent with Re-Os ages from molybdenite. This molybdenite is found in

fractures crosscutting Lufilian ore. While this timing is highly unusual, it may reflect a collisional event at the southern margin of the Gondwana supercontinent. This previously unknown mineralization event further complicates the ores of the Central African Copperbelt, and the stratiform ore model as a whole.

Acknowledgements

I wish to thank my wonderful parents for their unwavering support of my academic pursuits since enrolling in college in 2010. I cannot accurately express how lucky I am to have them as parents. I hope that I will be able to return in-kind the support you have so selflessly given to me. I love you both so much.

Thank you to my Supervisor, Dr. Robert Creaser, for his superior knowledge of radiogenic isotopes and geochronology. I am so grateful to have been one of your students, and to work on such a high quality research project with one of the giants in our discipline.

Thank you to my two Committee Members, Dr. Pilar Lecumberri-Sanchez, and to Dr. Long Li. You both have provided such valuable geochemical insight. I always appreciated y'all's enthusiasm to meet with me and share your in-depth understanding of complex problems. I hope this work reflects our time together, as I enjoyed collaborating with you both, and hope to do so in the future.

To my labmates, (the now Dr.) Danny Hnatyshin and Jon Toma, thank you. You have been more than labmates-you have been my friends. I also wish to thank the hard work of our lab technicians, lab coordinators, and support staff; you all make life much more bearable and have my gratitude.

Finally, thank you to Dr. Amy Weislogel at my alma mater, West Virginia Univerity. Thank you for sharing your expertise in geochronology and sedimentology with me, and for giving an average undergraduate student an opportuinity that truly changed my life. You introduced me to the world of geochronology via U-Pb in detrital zircons. Laser ablation is a blast!

Thank you all.

Table of Contents

Page

1) Introduction 1

1.1 Geological Background of Central African Copperbelt 1

1.1.1 Age of Sediments and Basement 1

1.1.2 Basin Inversion 2

1.1.3 Genetic Hypotheses and Preexisting Age Constraints of the CAC 2

1.2 Chibuluma West Deposit Geology 7

1.3 Kamoa Deposit Geology 8

1.4 Kipushi Deposit Geology 9

1.5 Purpose 10

1.5.1 Age of Sediments and Basement 10

1.5.2 Geochronology 11

1.5.3 Elemental Distribution 12

1.5.4 Stable Isotopes 12

1.5.5 Summary 13

1.6 References 13

2) Sample Description and Geological Context 21

2.1 Introduction 21

2.2 Petrography of Kamoa and Kipushi 21

2.2.1 Temperature Constraint at Kipushi 21

2.3 Sample Description and Parageneis of Chibuluma West, Kamoa, and Kipushi 23

2.3.1 Generalized Paragenesis of CAC deposits 23

2.3.2 Chibuluma West 23

2.3.3 Kamoa 24

2.3.4 Kipushi 25

2.4 Conclusion *26*

2.5 References *27*

3) Re-Os Geochronology 38

3.1 Background *38*

3.1.1 Introduction 38

3.1.2 Previous Re-Os Geochronology at Chibuluma West and Kipushi 39

3.2 Methodology *40*

3.2.1 Physical Separation 40

3.2.2 Chemical Separation 42

3.2.3 Mass Spectrometry 43

3.3 Results *45*

3.3.1 Calculation of Re-Os Ages 45

3.3.2 Chibuluma West 46

3.3.3 Kamoa 47

3.3.4 Kipushi 47

3.4 Discussion *48*

3.4.1 Mineralization at Chibuluma West 49

3.4.2 Mineralization at Kamoa 50

3.4.3 Mineralization at Kipushi 51

3.5 Conclusion *52*

3.6 References *53*

4) Molybdenum Distribution and Elemental Imaging 65

4.1 Background *65*

4.1.1 Introduction and Purpose 65

4.1.2 Choice of Sample Material 65

4.2 Sampling and Methodology 66

3.1.1 EPMA 66

4.2.2 LA-ICP-MS 67

4.3 Results 68

4.3.1 EPMA Results 68

4.3.2 LA-ICP-MS Results 69

4.4 Discussion 70

4.4.1 Chibuluma West Mo Distribution 70

4.4.2 Kamoa Mo Distribution 71

4.4.3 Kipushi Mo Distribution 72

4.4.4 Zoning of Major and Minor Elements 73

4.4.5 Elemental Correlations 74

4.5 Conclusion 74

4.6 References 75

5) Pb-Pb Geochronology 87

5.1 Background 87

5.1.1 Introduction 87

5.1.2 Calculating Model Lead and Pb-Pb Isochron Ages 87

5.1.3 Evaluation of Previous Pb-Isotope Geochronology of CAC 89

5.1.4 Kipushi Deposit 90

5.2 Sampling and Mass Spectrometry 91

5.2.1 Chemical Separation 91

5.2.2 Mass Spectrometry 92

5.3 Results *92*

5.3.1 Kamoa 93

5.3.2 Kipushi 93

5.3.3 Chibuluma West 94

5.4 Discussion *95*

5.4.1 Age Constraints for Kamoa 95

5.4.2 Age Constraints for Kipushi 97

5.4.3 Age Constraints for Chibuluma West 97

5.4.4 Mu and Pb Origin 98

5.5 Conclusion *100*

5.6 References *101*

6) Oxygen Isotopes 119

6.1 Background *119*

6.2 Sampling and Mass Spectrometry *119*

6.3 Results *120*

6.4 Discussion *120*

6.4.1 Oxygen Diffusion 120

6.4.2 Identification of a Separate, Post-Ore Fluid 127

6.4.3 Fluid Source Tracing 129

6.3 Conclusion *131*

6.6 References *131*

7) Synthesis and Summary 151

7.1 Future Development & Improvement *151*

7.2 Final Conclusions *151*

7.3 References *154*

Appendix **167**

Magnetic Separation Notes *167*

Carbonate Dissolution Experiments *168*

Pairwise Elemental Correlation *169*

References *170*

List of Tables

Page

2.1 Carbonate twin results *34*

3.1 Re-Os isotopic results of mono and double-spiked samples *58*

4.1 Co, Mo, and Re elemental correlation *86*

5.1 Pb isotope results *106*

5.2 Compiled values and coefficents for model Pb calculation *110*

6.1 C, O isotopic results *140*

6.2 O diffusion rates for dry and wet carbonate *145*

6.3 Post-ore calcite and syn-ore dolomite $\delta^{18}O$ *values* *149*

6.4 Theoretical $\delta^{18}O$ *values of post-ore calcite* *150*

List of Figures

Page

1.1 Geological map of CAC *18*

1.2 Stratigraphy column of Katangan Supergroup *19*

2.1 Kamoa and Kipushi thin section images *29*

2.2 Chibuluma West, Kamoa, and Kipushi paageneses and sulphide % abundance *31*

2.3 Carbonate twin cartoon *33*

2.4 Carbonate twin temperature estimation *37*

3.1 Physical separation procedure *57*

3.2 Chibuluma West Re-Os isochron diagrams *62*

3.3 Kamoa Re-Os isochron diagrams *63*

3.4 Kipushi Re-OS isochron diagrams *64*

4.1 Kamoa and Kipushi EPMA single grain elemental maps *77*

4.2 Chibuluma West EPMA Pyrite-5 aliquot elemental maps *79*

4.3 Chibuluma West EPMA Pyrite-1 aliquot elemental maps *80*

4.4 Kamoa LA-IC-PMS Mo map overlay *81*

4.5 Kipushi LA-ICP-MS Mo map overlay *83*

4.6 LA-ICP-MS Co, Mo, and Re elemental correlation *85*

5.1 Common lead evolution curve *105*

5.2 Pb evolution Geochron reference line with CAC deposits *111*

5.3 Chibuluma West Pb-Pb isochron diagrams *112*

5.4 Chibuluma West and Kamoa radiogenic Pb *114*

5.5 Effect of μ on Two-Stage reference line with CAC deposits *115*

5.6 Plumbotectonics for $^{206}Pb/^{204}Pb$ *vs* $^{207}Pb/^{204}$ *117*

6.1 Kipushi carbonate sampling locations 136

6.2 Kipushi C, O isotope cross plot 138

6.3 Diffusion profile cartoon.....142

6.4 Measured O diffusion profile.....143

6.5 O diffusion rates in dry dolomite and wet calcite.....144

6.6 Diffusion profiles of measured vs theoretical $\delta^{18}O$ *values in wet calcite* 147

6.7 Diffusion profiles measured vs theoretical $\delta^{18}O$ *values in simulated wet dolomite* 148

Abbreviations

^{o} – Side-slope degrees

$(^{187}Os/^{188}Os)_i$ – Initial $^{187}Os/^{188}Os$

$(^{187}Os/^{188}Os)_p$ – Present $^{187}Os/^{188}Os$

$^{238}U/^{204}Pb$ – μ

α – Angle of twinned carbonate crystal edge

A – Current

Å – Angstrom

$Ba(OH)_2$ – Barium Hydroxide

$Ba(NO_3)_2$ – Barium Nitrate

$Br_{2\ (aq)}$ – Bromine (aqueous)

BSE – Back Scattered Electrons

C – Concentration

c_0 – Oxygen sink (host rock dolomite)

c_1 – Oxygen source (syn-ore dolomite)

CCIM – Canadian Centre for Isotopic Microanalysis

CAC – Central African Copperbelt

$CHCl_3$ – Chloroform

$CO_{2(g)}$ – Carbon dioxide gas

cps – counts per second

CrO_3+H_2SO_4 – Chromium trioxide and sulphric acid

D – Diffusion coefficient

$\delta^{18}O_A$ – syn-ore dolomite

$\delta^{18}O_B$ – post-ore calcite

DRC – Democratic Republic of the Congo

$(\overline{E_p})$ – Mean on-peak measured cps

EPMA – Electron Probe Microanalysis

erf(x) – Error function of x

$H_2O_{(l)}$ – Water

H_2O_2 – Hydrogen peroxide

H_3O_4 – Phosphoric acid

HBr – Hydrobromic acid

$He_{(g)}$ – Helium gas

HNO_3 – Nitric acid

ICP-MC-MS– Inductively Coupled Multicollecter Plasma Mass Spectrometry

ID – Isotope Dilution

IRMS – Isotope Ratio Mass Spectrometry

K_m – Magnetic susceptibility

L – Diffusion Length

LA – Laser Ablation

LLHR – Low-Level Highly Radiogenic

m/z – Mass to charge ratio

MI – Methylene Iodide

MI_h – Methylene Iodide heavy fraction

N-TIMS – Negative Thermal Ionisation Mass Spectrometry

$O_{2(g)}$ – Oxygen gas

Ppb – Part per billion ($1/10^9$ or ng)

Ppm – Part per million ($1/10^6$ or μg)

Ppt – Part per trillion ($1/10^{12}$ or pg)

QICPMS – Quadrupole Inductively Coupled Plasma Mass Spectrometry

ROI – Region of Interest

S_E – Elemental Sensitivity

T – Temperature, Celsius or Kelvin (denoted)

t_r – Residence time of hydrothermal fluid

t_n – Carbonate twin

w_c – Width of a carbonate crystal

w_n – Width of a carbonate twin (t_n)

XRD – X-Ray Diffraction

1) Introduction

1.1 Geological Background of the Central African Copperbelt

The Central African Copperbelt (CAC) is located in the southern Democratic Republic of the Congo (DRC), and northern Zambia (Figure 1.1). The CAC consists of over 30 sediment-hosted stratiform Cu-Co deposits and numerous other prospects (Annels et al., 1983; Selley et al., 2005). The host sedimentary rocks are lithologically varied and include conglomerate, dolomite, arenite, shale, and siltstone (Whyte, 1971; Cailteux et al., 2005; Selley et al., 2005; Schmandt et al., 2013; Rooney et al., 2015). These host sedimentary rocks were deposited in the Katangan Basin and are referred to as the Katangan Supergroup (Figure 1.2)-a Neoproterozoic epicontinental marine to near-marine package (De Magnée and Francois, 1988; Jackson et al., 2003; Kampunzu et al., 2009; Sillitoe et al., 2010; Haest and Muchez, 2011). The Katangan Basin and the Katangan Supergroup sediments are the result of rifting of the supercontinent Rodinia in the Neoproterozoic (Porada and Berhorst, 2000; Jackson et al., 2003; Batumike et al., 2007; Kampunzu et al., 2009; Sillitoe et al., 2010).

1.1.1 Age of Sedimentary Rock and Basement

Whereas the age of the sedimentary rocks of the Katangan Supergroup are fairly poorly constrained, direct radiometric dating of the shale immediately underlying the Grand Conglomerate in the Nguba Group yielded a Re-Os depositional age of 727 ± 4.9 Ma (Rooney et al., 2015). The Petit Conglomerate, which separates the Nguba and Kundelungu Groups, has been lithostratigraphically constrained to 635 Ma (Kampunzu et al., 2009). The maximum age of the Katangan Supergroup may extend to the youngest known basement age of ~883 Ma, being the age of the Nchanga Granite (Armstrong et al., 2005). The oldest known basement ages are of

Paleoproterozoic time ~2.05 Ga (Rainaud et al., 2005). These Paleoproterozoic basement rocks underlie much of central and southern Africa (Frimmel et al., 2004).

1.1.2 Basin Inversion

The Katangan Basin was uplifted during the Lufilian orogeny, <656-490 Ma (Chabu, 1995; Porada and Berhorst, 2000; Selley et al., 2005). The Lufilian orogeny was the result of the collision between the Congo Craton and the Kalahari Craton (Selley et al., 2005; Kampunzu et al., 2009). The Lufilian orogeny is genetically and temporally related to the Damaran orogeny located in Namibia, and has thus been termed the Damaran-Lufilian fold belt regionally (Kamona et al., 1999). Similarly, the Gariep Belt of Namibia and South Africa is another Pan-African aged orogenic belt with sediment-hosted ores (Frimmel et al., 2004). The Katangan Basin was regionally metamorphosed to greenschist facies, although amphibolite facies is present in the Domes Region of Zambia in the orogen core (Figure 1.1), and deposits in the northwest of the CAC are minimally metamorphosed (if) at all (Annels et al., 1983; Chabu, 1995; Selley et al., 2005; Batumike et al., 2007; Schmandt et al., 2013). Peak metamorphic conditions occurred at 530 Ma (John et al., 2004).

1.1.3 Genetic Hypotheses and Preexisting Age Constraints of the CAC

The CAC has been subjected to several hypotheses regarding ore genesis, and in particular, the timing of ore mineralization has been a contentious issue. A syngenetic-diagenetic (pre-Lufilian) origin has been widely accepted by many workers (Whyte and Green, 1971; Richards et al., 1988a; Richards et al., 1988b; Cailteux, 1994; Cailteux et al., 1994; Kampunzu and Cailteux, 1999; Porada and Berhorst, 2000; Barra et al., 2004; Cailteux et al., 2005; Dewaele et al., 2006; Haest and Muchez, 2011; Hitzman et al., 2012; Schmandt et al., 2013; Muchez et al., 2015). This pre-Lufilian hypothesis is contested by an epigenetic (Lufilian)

origin (Kamona et al., 1999; Torrealday et al., 2000; Haest and Muchez, 2011; Sillitoe et al., 2015; Sillitoe et al., 2017); Saintilan et al., 2018).

In general, Re-Os direct dating of ore minerals (ex: bornite, chalcopyrite, digenite) from CAC deposits has resulted in poor age constraints that may be interpreted as having a diagenetic origin, although a 600 Ma model age span is observed at Kamoto in Muchez et al. (2015). These model ages are contrasted to well constrained Re-Os ages from molybdenite, and are of Lufilian age (Sillitoe et al., 2015; Sillitoe et al., 2017). Pb-Pb ages are also varied, although a diagenetic or pre-Lufilian origin is assigned to much of the CAC (Richards et al., 1988b). A review of previous workers' attempts at dating and thus constraining the timing of ore formation in the CAC is provided below.

Re-Os model ages of ore stage vein-hosted molybdenite from the Kansanshi deposit range from ~ 502 to 513 Ma, with uncertainties of 1.7 Ma (Torrealday et al., 2000). These well constrained, and high precision ages are associated with post-peak metamorphism of the Lufilian orogeny. However, these workers also interpret that older diagenetic ore was remobilized in fluids during the Lufilian Orogeny.

Re-Os dating of a chalcopyrite and bornite phase mixture from the Konkola deposit in the Upper Roan Group produced an isochron age of 816 ± 62 Ma (Barra and Broughton, unpub. data, in Selley et al. 2005). This age was taken as the primary evidence for diagenetic mineralization. However, this age is derived from a bulk sulphide analysis of minerals that are not well understood. Closure temperature, susceptibility of Os diffusion, and common Os integration upon formation are not documented for these minerals. Additionally, the relatively high error is indicative of general isotopic disturbance to the system and underlies the reliability of these chosen sulphide minerals for Re-Os geochronology. Finally, the basal unconformity of

the Lower Roan Group (and the Katangan Supergroup as a whole) contacts the 883 ± 10 Ma Nchanga Granite. Using this time constraint, the Re-Os sulphide age of 816 ± 62 Ma from ore in the Upper Roan Group is unreasonable given that it overlaps with the age of the basement. Instead, the 816 Ma age is possibly the maximum age of mineralization, and may be the result of radiogenic Os incorporating into untested geochronometers.

A second chalcopyrite and bornite bulk analysis was conducted on samples from the Nkana-Mindola, Chibuluma West, and Nchanga deposits. These samples were placed together on the same isochron, yielding an age of 576 ± 41 Ma (Barra and Broughton, unpub. data, in Selley et al. 2005). This age most definitely is a mixing line, and despite having a Lufilian timing, is meaningless as it is an average of the isotopic composition from three deposits.

Evidence for a post-Lufilian ore emplacement at the Kipushi deposit was given by Schneider et al. (2007). These workers analyzed monomineralic renierite and bornite samples separately, and produced a Re-Os isochron with an age of 450 ± 3.4 Ma. Isotopic results from the renierite samples suggest the existence of molybdenite inclusions. These workers however suspect an unidentified cause for the high Re/Os and Os/Os ratios in lieu of molybdenite. Given that no elemental imaging (of Mo) was performed on the renierite samples, the possibility of molybdenite inclusions should not be abandoned, especially in the absence of an explanation for the isotopic results.

Further Re-Os dating of impure mineral separates from Kamoto (Mines Subgroup of Lower Roan) coupled with suspect geochronometers (chalcocite, carrolite, and digenite) has produced ages from 821 ± 51 Ma to 230 ± 36 Ma (El Desouky et al., 2010; Muchez et al., 2015). These samples did not produce an isochron, but were plotted in comparison to an array of reference growth lines in ^{187}Re (ppt) vs ^{187}Os* (ppt) space, assuming an initial Os of 0 ppb.

While there is evidence of molybdenite in three of the 11 samples, it may not be appropriate to plot them in this manner without conclusive evidence of the existence of molybdenite in the samples. By placing all 11 samples on a molybdenite-style Re-Os plot, and by ignoring any initial Os, the model ages will be apparent. In other words, the model ages are forced through the origin (initial Os = 0 ppt), resulting in an older age. As previously mentioned, the inclusion of multiphase, bulk analyses results in Re-Os ages that are difficult to interpret, due to possible mixing or heterogeneity between these phases. In either case, the model ages suggest pre-Lufilian, orogenic (Lufilian), and post-Lufilian timing for the ores at Kamoto.

Sillitoe et al. (2015) have identified two mineralization events throughout various deposits in the CAC. The first event occurred prior to deposition of the Katangan Supergroup, as copper was pre-enriched at the Nyungu prospect. Re-Os molybdenite model ages bracket this pre-enrichment at 1084 to 1059-and is linked to the ~1.1 Ga Irumide orogeny. Interestingly, the second event, occurring during the Lufilian orogeny contained coeval disseminated and vein-hosted molybdenite model ages ranging from 536 to 499 Ma. This observation was made at the Chimiwungu, West Mwombezhi, Mufuka, and Kabikupa deposits. That is, there is no discernible difference depending on the type of mineralization, implying that both styles of mineralization were introduced simultaneously, and providing isotopic support for the hypothesis of Sillitoe et al. (2010).

Additional evidence for a Lufilian ore timing is provided by Sillitoe et al. (2017), where Re-Os molybdenite from the Lufubu South (vein-hosted and disseminated), Chambishi SE (disseminated), Chibuluma South (vein-hosted and disseminated), Mufulira (vein-hosted and disseminated), Konkola West (vein-hosted), Sentinel (disseminated), and Mujimbeji (vein-hosted and disseminated) deposits all return model ages ranging from ~525 to 490 Ma. Similar to the

results obtained from the Sillitoe et al. (2015), and possibly from the Schneider et al. (2007) studies, Re-Os dating of molybdenite has provided no support for the diagenetic ore model.

Recently, Saintilan et al. (2018) provide promising results for the use bornite and carrolite to directly date ore formation at the Kamoto deposit. Unlike previous attempts at using bornite, and copper minerals as a whole, results from this study yielded high precision ages. A multi-stage mineralization is provided as isochrons indicate ore precipitation at 609 ± 5 Ma, ~518 Ma, and 473 ± 4 Ma. Successful direct dating from ore minerals proves mineralization occurred during and after the Lufillian orogeny. These results, as well as those of Schneider et al. (2007), Sillitoe et al. (2015), and Sillitoe et al. (2017) have produced either Lufilian or post-Lufilian timings for ore formation with zero accompanying evidence of a diagenetic timing, or remobilization of pre-existing ore.

In general, results from Pb-Pb geochronology have been interpreted as supporting a pre-Lufilian (>656 Ma) timing for ore emplacement in the CAC (Richards et al., 1988a; Walraven and Chabu, 1994; Kamona et al., 1999; Kampunzu and Cailteux, 1999). These primary, stratiform ores were then remobilized during the Lufilian orogeny (Batumike et al., 2007).

Pb model ages of stratiform sulphides from the Musoshi deposit produced a Stacey and Kramers (1975) Two-Stage isochron age of 645 ± 15 Ma, and is interpreted as an age minimum for ore deposition (Richards et al., 1988a). A diagenetic origin is suggested for the Kabwe deposit with Stacey and Kramers (1975) Two-Stage model Pb ages of 680 Ma, and a μ of 10.31(Kamona et al., 1999). A post-orogenic, two-stage Pb model age of 454 ± 14 Ma, μ of 9.88, is reported by Walraven and Chabu (1994) for Kipushi galena. Finally, Schneider et al. (2007) mention that the homogeneity of Pb isotopes from Kipushi sulphides is suggestive that the crustally derived Cu-Ge, and Zn ore precipitated from a single fluid.

1.2 Chibuluma West Deposit Geology

Relatively little has been published on the Chibuluma West deposit, compared to larger deposits throughout the CAC. The Chibuluma deposit (of which Chibuluma West is a subsidiary deposit) is hosted in the quartz-rich sediments of the Mines Subgroup (R 2) in the Lower Roan Group (Figure 1.2) of Zambia (Figure 1.1) (Winfield, 1961; Whyte and Green, 1971). Ore mineralization is located near the intersection of an extensional fault with the underlying granitic basement (Selley and Cooke, 2001). The basement is metamorphic, consisting of gneiss and schist (Winfield, 1961; Whyte and Green, 1971). The Lufubu Schist underlies Chibuluma, while the Muva Quartzite is located ~2.5 km south (Winfield, 1961).

Lithologically, the Cu-Co ore is hosted in the orebody quartzite located in the footwall (Selley and Cooke, 2001), and is mica rich (Binda and Mulgrew, 1974). The orebody quartzite is overlain by a poorly sorted feldspathic hangingwall sandstone (Selley and Cooke, 2001). The host sediments were subsequently metamorphosed to quartzite (Winfield, 1961; Selley and Cooke, 2001) under greenschist facies conditions (Whyte and Green, 1971). Fracturing resulted in increased permeability, allowing for fluid mobility through the host sediments (Selley and Cooke, 2001).

Bacterial sulphate reduction is a common process throughout many CAC deposits, although it is not interpreted to have occurred at Chibuluma West (Selley and Cooke, 2001). These workers note that considering the range of $\delta^{34}S$ values obtained over a range of depths and the independence of isotopic signatures with sulphide mineralogies, a single sulphur source is unlikely. Instead, minerals such as ilmenite and detrital rutile are suspected as serving as the reductant (Selley and Cooke, 2001) for the oxidized ore fluid-allowing for precipitation of ore metals. Ore mineralization is interpreted as having a syngenetic timing (although Co

mineralization in particular is of metamorphic origin) and is stratiform with both discordant and concordant veinlets (Winfield, 1961; Whyte and Green, 1971; Brown, and Bartholomé, 1972; Sweeney et al., 1991; Selley and Cooke, 2001). Disseminated sulphide is also found in the footwall orebody quartzite, although the highest grade of sulphide mineralization is vein-hosted (Selley and Cooke, 2001). Gangue minerals include biotite, carbonate, molybdenite, and quartz are structurally controlled by faults and shearing (Whyte and Green, 1971; Selley and Cooke, 2001; Sillitoe et al., 2017).

1.3 Kamoa Deposit Geology

With its recent discovery by Broughton and Rogers (2010), the Kamoa deposit has not been the subject of many studies. Originally unexplored due to being located on the fringe of the Lufilian Arc (and outside the mineralised zone), the Kamoa deposit is a sediment-hosted stratiform deposit (Schmandt et al., 2013). The Kamoa deposit is hosted in the Grand Conglomerate of the Lower Nguba Group (Figure 1.2) in the DRC (Figure 1.1), and immediately overlies the Mwashya sediments of the Upper Roan Group (Schmandt et al., 2013); positioning it above the Chibuluma West deposit located in the Lower Roan, and below the Kipushi deposit (see Chapter 1.4). The Grand Conglomerate is a Sturtian-aged (<727 Ma to 660 Ma) glacial diamictite, and was deposited in a shallow-marine environment during glacial mass-wasting events (Kampunzu et al., 2009; Schmandt et al., 2013; Rooney et al., 2015). Globally, this diamictite sedimentation is capped by ca. 660-655 Ma shales, meaning that the duration of sedimentation for this unit is estimated to be ca. 70 Myr. This has important implications for geochronological dating as the Cu ore at Kamoa must have formed after 660 Ma.

The Kamoa deposit has not been metamorphosed by the Lufilian orogeny, and ore mineralization is limited to a single event (Schmandt et al., 2013). Sulphide mineralization is

interpreted as occurring immediately following diagenesis during basin-fill. Sulphide mineralization is stratigraphically controlled as the Grand Conglomerate host rock represents a redoxocline boundary with respect to the underlying (oxidized) Roan sediments (Brown, 1997; Schmandt et al., 2013). Ore-stage sulphide minerals precipitated relatively concurrently, and were associated with ankerite, biotite, muscovite, and quartz (Schmandt et al., 2013). After hydrothermal mineralization, a supergene enrichment event (to a depth of 250 m) occurred precipitating both additional sulphides (sphalerite and chalcocite) as well as carbonates and oxides (chrysocolla, cuprite, and malachite), as well as native copper (Schmandt et al., 2013).

1.4 Kipushi Deposit Geology

The Kipushi deposit is perhaps the most studied of the sediment-hosted deposits in the CAC. Kipushi is located in the DRC, near the Zambian border (Figure 1.1) in the relative centre of the Lufilian Arc. The <600 m thick orebodies are predominately concentrated in the Kakontwe Formation of the Nguba Group (Figure 1.2) (Haest and Muchez, 2011; Van Wilderode et al., 2013; Turner et al., 2018)-former Lower Kundelungu Group (De Magnée and Francois, 1988). The Kakontwe Formation is composed of dolomite and algal material (interpreted as a reef by Turner et al., 2018) and was deposited in a marine environment (Batumike et al., 2007; Van Wilderode et al., 2013; Turner et al., 2018). The Kakontwe Formation was metamorphosed to greenschist facies during the Lufilian orogeny (Heijlen et al., 2008; Haest and Muchez, 2011).

Ore appears to be structurally controlled by the Kipushi Fault (De Magnée and Francois, 1988; Heijlen et al., 2008; Haest and Muchez, 2011; Van Wilderode et al., 2013), where the mineralizing fluid was able to migrate upwards and precipitate at the (redox boundary) contact with the overlying dolomitic shales (Heijlen et al., 2008). The Kipushi Fault cuts across the

breccia of the northwest-southeast trending Kipushi anticline, (Van Wilderode et al., 2013). The breccia is composed of talc-rich dolomite and chloritic silts, derived from the underlying Lower Roan sediments (De Magnée and Francois, 1988).

This hypothesis was recently contested by Turner et al (2018) who favour a stratigraphic control for ore formation. Instead, these workers suggest that the Kipushi Fault is a reef accumulation, whose deformational characteristics were conducive for fluid migration and concentration (Turner et al., 2018). Sulphide ores are present both as vein-hosted (pipes and discordant offshoots) as well as disseminations throughout the host rock (De Magnée and Francois, 1988; Haest and Muchez, 2011; Turner et al., 2018). Ores are vertically zoned, as the upper region of Kipushi is chalcocite dominant, while at the basal region, chalcopyrite is most common (Intiomale and Oosterbosch, 1974; Haest and Muchez, 2011). Supergene enrichment has been found up to depths of 70 m (Van Wilderode et al., 2013). Iron hydroxides are common secondary minerals at Kipushi-specifically limonite replacing pyrite (Lhoest, 1995).

Kipushi has been interpreted as having both a pre-tectonic (pre-Lufilian) (Walraven and Chabu, 1994), and a post-tectonic origin (Kamona et al., 1999; Schneider et al., 2007). Furthermore, ore remobilization ca 450 Ma has been proposed (Walraven and Chabu, 1994: Batumike et al., 2007).

1.5 Purpose

Despite the CAC being studied for nearly a century, many questions regarding the origin and ore-forming conditions remain unanswered (Selley et al., 2005). Conflicting evidence and a wide range of proposed hypotheses have resulted in great debate, perhaps most particularly with respect to the geochronology and timing of the ore mineralization.

1.5.1 Petrography

Petrographic analysis of the Kamoa and Kipushi deposits provides essential geological context in the interpretation of the geochronological results. Constraining when the geochronometer (mineral) formed in relation to the ore minerals is necessary for a meaningful interpretation.

Despite numerous geothermometric studies involving fluid inclusions (Richards et al., 1988a; Dewaele et al., 2006; Muchez et al., 2010; Schmandt et al., 2013), there is much variation in the reported temperatures. While results obtained from fluid inclusions more accurate and precise, fluid temperature may be approximated by calcite twin intensity. In addition, shear strain experienced by the calcite (or dolomite) offers comparative insight into the tectonic conditions.

1.5.2 Geochronology

Since the Chibuluma West deposit is located in the core of the Lufilian orogene, any age constraints should reflect a compressional tectonic setting. That is, age results from Chibuluma West should be similar to the timing of peak metamorphism experienced by the Katangan Supergroup during the Lufilian orogeny, thereby serving as a datum from which to compare other vein-hosted metamorphosed CAC deposits. In addition, there is relatively little published information for this deposit, and additional age constraints are likely to be geologically meaningful.

One confounding problem is in separating stratiform ages from vein ages. While many previous workers have successfully dated vein-hosted ore, little has been published on primary stratiform ore. The significance of the Kamoa deposit is it has not been metamorphosed. This means that the stratiform ore found at Kamoa is unaltered or remobilized. The geochronological

age obtained from this deposit can only pertain to the original stratiform ore, and thus the stratiform ores for other CAC deposits.

Similar to the Chibuluma West deposit, ores from the Kipushi deposit are vein-hosted. The ore from Kipushi is generally associated with a post-orogenic timing. The Kipushi deposit in particular contains arsenopyrite (Chabu, 1995; Schneider et al., 2007), a sulphide mineral that has proven to be a reliable geochronometer (Morelli et al., 2005). In addition, age constraints for the unexplored Big Zinc ore zone may be directly compared to pre-existing results from other regions of this deposit.

1.5.3 Elemental Distribution

The intimate relation between Mo and Re has important geochronological implications (see below). Identifying where the Mo is located in sulphide and gangue mineral grains elucidates complicating geochronological ages and aids in the determination of multiple fluid mineralization events.

1.5.4 Stable Isotopes

Stable isotopes are invaluable in ore deposit research as they provide useful information regarding fluid conditions including temperature and fluid source (Campbell and Larson, 1998). A novel approach to geothermometry has been outlined and successfully applied to the main ore fluid for the Kipushi deposit. Multiple fluid generations may also be proven by equilibration calculations, serving as an independent verification for petrographic observations.

1.5.5 Summary

By applying a multi-faceted approach consisting of petrography, geochronology, high resolution trace element imaging, and stable isotopic analysis, it is hoped that the genesis of the three studied sediment-hosted CAC deposits may be improved.

1.6 References

Annels, A.E., Vaughn, D.J., and Craig, J.R., 1983, Conditions of ore mineral formation in certain Zambian Copperbelt deposits with special reference to the role of cobalt, Mineralium Deposita, v. 18, p. 71-88

Armstrong, R.A., Master, S., and Robb, L.J., 2005, Geochronology of the Nchanga Granite, and constraints on the maximum age of the Katanga Supergroup, Zambian Copperbelt, Journal of African Earth Sciences, v. 42, p. 32-40

Barra, F., Broughton, D., Ruiz, J., and Hitzman, M., 2004, Multi-stage mineralization in the Zambian Copperbelt based on Re-Os isotope constraints, Geological Society of America Abstracts with Programs, v. 36, n. 5., p. 516

Batumike, M.J., Cailteux, J.L.H., Kampunzu, A.B., 2007, Lithostratigraphy, basin development, base metal deposits, and regional correlations of the Neoproterozoic Nguba and Kundelungu rock successions, central African Copperbelt, Gondwana Research, v. 11, p. 432-447

Binda, P.L., and Mulgrew, J.R., 1974, Stratigraphy of copper occurrences in the Zambian copperbelt, *In:* Bartholomé, P (Ed), Gisements Stratiformes et Provinces Cupriféres. Soc. Géol., Liège, Belgique, p. 215-233

Broughton, D., and Rogers, R., 2010, Discovery of the Kamoa copper district, Central Africa Copperbelt, DRC, Society of Economic Geologists Special Publication 15, v. 1, p. 287-298

Brown, A.C., 1997, World-class sediment-hosted stratiform copper deposits: Characetistics, genetic concepts and metallotects, Australian Journal of Earth Sciences, v. 44, p. 317-328

Brown, A.C., and Bartholomé, P., 1972, Inhomogeneities in cobaltiferous pyrite from the Chibuluma Cu-Co deposit, Zambia, Mineralium Deposita, v. 7, p. 100-105

Cailteux, J., 1994, Lithostratigraphy of the Neoproterozoic Shaba-type (Zaire) Roan Supergroup and metallogenesis of associated stratiform mineralization, Journal of African Earth Sciences, v. 19, p. 279-301

Cailteux, J., Binda, P.L., Katekesha, W.M., Kampunzu, A.B., Intiomale, M.M., Kapenda, D., Kaunda, C., Ngongo, K., Tshiauka, T., and Wendorff, M., 1994, Lithostratigraphical correlation of the Neoproterozoic Roan Supergroup from Shaba (Zaire) and Zambia, in

the central African copper-cobalt metallogenic province, Journal of African Earth Sciences, v. 19, n. 4., p. 265-278

Cailteux, J.L.H., Kampunzu, A.B., Lerouge, C., Kaputo, A.K., and Milesi, J.P., 2005, Genesis of sediment-hosted stratiform copper-cobalt deposits, central African Copperbelt, Journal of African Earth Sciences, v. 42, p. 134-158

Campbell, A.R., and Larson, P.B., 1998, Introduction to stable isotope applications in hydrothermal systems, *In:* Richards, J.P., and Larson, P.B., (Eds), Reviews in Economic Geology, v. 10, Society of Economic Geologists, Littleton, USA, p. 173-195

Chabu, M., 1995, The geochemistry of phlogopite and chlorite from the Kipushi Zn-Pb-Cu deposit, Shaba, Zaire, The Canadian Mineralogist, v. 33, p. 547-558

De Magnée, I., and Francois, A., 1988, The origin of the Kipushi (Cu, Zn, Pb) deposit in direct relation with a Proterozoic salt diaper, Copperbelt of Central Africa, Shaba, Republic of Zaire, *In:* Friedrich, G.H., and Herzig, P.M., (Eds), Base Metal sulfide Deposits, Springer-Verlag, Berlin, Germany

Dewaele, S., Muchez, P., Vets, J., Fernandez-Alonzo, M., and Tack, L., 2006, Multiphase origin of the Cu-Co ore deposits in the western part of the Lufilian fold-and-thrust belt, Katanga (Democratic Republic of Congo), Journal of African Earth Sciences, v. 46, p. 455-469

Frimmel., H.E., Jonasson, I.R., and Mubita, P., 2004, An Eburnean base metal source for sediment-hosted zinc-lead deposits in Neoproterozoic units of Namibia: Lead isotopic and geochemical evidence, Mineralium Deposita, v. 39, p. 328-343

Haest, M., and Muchez, P., 2011, Stratiform and vein-type deposits in the Pan-African orogen in central and southern Africa: Evidence for multiphase mineralization, Geologica Belgica, v. 14, p. 23-44

Heijlen, W., Banks, D.A., Muchez, P. Stensgard, B.M., and Yardley, B.W.D., 2008, The nature of the mineralizing fluids of the Kipushi Zn-Cu deposit, Katanga, Democratic Republic of Congo: Quantitative fluid inclusion analysis using laser ablation ICP-MS and bulk crush-leach methods, Economic Geology, v. 103, p. 1459-1482

Hitzman, M.W., Broughton, D., Selley, D., Woodhead, J., Wood, D., and Bull, S., 2012, The Central African Copperbelt: Diverse stratigraphic, structural, and temporal settings in the

world's largest sedimentary copper district, Society of Economic Geologists, Special Publication 16, p. 487-514

Intiomale M, Oosterbosch R (1974) Géologie et Géochemie du gisement de Kipushi Zaire, *In:* Bartholomé, P., (Ed), Gisements stratiformes et provinces cupriféres, Centenaire Société Géologique Belgique, Liége, p 123-164

Jackson, M.P.A., Warin, O.N., Woad, G.M., and Hudec, M.R., 2003, Neoproterozoic allochthonous salt tectonics during the Lufilian orogeny in the Katangan Copperbelt, central Africa, Geological Society of America Bulletin, v. 115, p. 314-320

John, T., Schenk, V., Mezger, K., and Tembo, F., 2004, Timing and PT evolution of whiteschist metamorphism in the Lufilian Arc-Zambezi belt orogen (Zambia): Implications for the assembly of Gondwana, The Journal of Geology, v.112, p. 71-90

Kamona, A.F., Lévêque, J., Friedrich, G., and Haack, U., 1999, Lead isotopes of the carbonate-hosted Kabwe, Tsumeb, and Kipushi Pb-Zn-Cu sulfide deposits in relation to Pan African orogenesis in the Damaran-Lufilian fold belt of Central Africa, Mineralium Deposita, v. 34, p. 273-283

Kampunzu, A.B., and Cailteux, J., 1999, Tectonic evolution of the Lufilian Arc (Central Africa Copper Belt) during Neoproterozoic Pan African orogenesis, Gondwana Research, v. 2, p. 401-421

Kampunzu, A.B., Cailteux, J.L.H., Kamona, A.F., Intiomale, M.M., and Melcher, F., 2009, Sediment-hosted Zn-Pb-Cu deposits in the Central African Copperbelt, Ore Geology Reviews, v. 35, p. 263-297

Lhoest, J.J., 1995, The Kipushi mine, Mineralogical Record, v. 26, p. 163-192

Morelli, R.M., Creaser, R.A., Selby, D., Kontak, D.J., and Horne, R.J., 2005, Rhenium-Osmium Geochronology of Arsenopyrite in Meguma Group Gold Deposits, Meguma Terrane, Nova Scotia, Canada: Evidence for Multiple Gold-Mineralizing Events, Economic Geology, v. 100, p. 1229-1242

Muchez, P., Brems, D., Clara, E., De Cleyn, A., Lammens, L., Boyce, A., De Muynck, D., Mukumba, W., and Sikazwe, O., 2010, Evolution of Cu-Co mineralizing fluids at Nkana Mine, Central African Copperbelt, Zambia, Journal of African Earth Sciences, v. 58, n. 457-474

Muchez, P., André-Mayer, A.S., El Desouky, H.A., and Reisberg, L., 2015, Diagenetic origin of the stratiform Cu-Co deposit at Kamoto in the Central African Copperbelt, Mineralium Deposita, v. 50, p. 437-447

Porada, H., and Berhorst, V., 2000, Towards a new understanding of the Neoproterozoic-Early Palæzoic Lufilian and northern Zambezi Belts in Zambia and the Democratic Republic of the Congo, Journal of African Earth Sciences, v. 30, n. 3, p. 727-771

Rainaud, C., Master, S., Armstrong, R.A., and Robb, L.J., 2005, Geochronology and nature of the Palaeoproterozoic basement in the Central African Copperbelt (Zambia and the Democratic Republic of Congo), with regional implications, Journal of African Earth Sciences, v. 42, p. 1-31

Richards, J.P. Cumming, G.L., Krstic, D., Wagner, P.A., and Spooner, E.T.C., 1988a, Pb isotope constraints on the age of sulfide ore deposition and U-Pb age of late uraninite veining at the Musoshi stratiform copper deposit, Central African Copperbelt, Zaire, Economic Geology, v. 83, p. 724-741

Richards, J.P., Krogh, T.E., and Spooner, E.T.C., 1988b, Fluid inclusion characteristics and U-Pb rutile age of late hydrothermal alteration and veining at the Musoshi stratiform copper deposit, Central African Copper Belt, Zaire, Economic Geology, v. 83, p. 118-139

Rooney, A.D., Strauss, J.V., Brandon, A.D., and Macdonald, F.A., 2015, A Cryogenian chronology: Two long-lasting synchronous Neoproterozoic glaciations, v. 43, p. 459-462

Saintilan, N.J., Selby, D., Creaser, R.A., and Dewaele, S., 2018, Sulphide Re-Os geochronology links orogenesis, salt and Cu-Co ores in the Central African Copperbelt, Nature Scientific Reports, v. 8, p. 1-8

Schmandt, D., Broughton, D., Hitzman, M.W., Plink-Bjorklund, P. Edwards, D., and Humphrey, J., 2013, The Kamoa copper district, Democratic Republic of the Congo: Stratigraphy, diagenetic and hydrothermal alteration, mineralization, Economic Geology, v. 108, p. 1301-1324

Schneider, J., Melcher, F., and Brauns, M., 2007, Concordant ages for the giant Kipushi base metal deposit (DR Congo) from direct Rb-Sr and Re-Os dating of sulfides, Mineralium Deposita, v. 42, p. 791-797

Selley, D., and Cooke, D., 2001, Mineral zonation and sulfur isotope systematics of the Chibuluma West copper-cobalt deposit, Zambia, AMIRA P544 Progress Report, December, p. 133-169

Selley, D., Broughton, D., Scott, R., Hitzman, M., Bull, S., Large, R., McGoldrick, P., Croaker, M., and Pollington, N., 2005, A new look at the geology of the Zambian Copperbelt, Economic Geology 100th Anniversary Volume, v. 29, p. 485-522

Sillitoe, R.H., Perelló, J., and Garcia, A., 2010, Sulfide-bearing veinlets throughout the stratiform mineralization of the Central African Copperbelt: Temporal and genetic implications, Economic Geology, v. 105, p. 1361-1368

Sillitoe, R.H., Perelló, J, Creaser, R.A., Wilton, J., and Dawborn, T., 2015, Two ages of copper mineralization in the Mwombezhi Dome, Northwestern Zambia: Metallogenic implications for the Central African Copperbelt, Economic Geology, v. 110, p. 1917-1923

Sillitoe R.H., Perelló, J, Creaser, R.A., Wilton, J., Wilson, A.J., and Dawborn, T., 2017, Age of the Zambian Copperbelt, Mineralium Deposita, v. 52, p. 1245-1268

Sweeney, M.A., Binda, P.L., and Vaughn, D.J., 1991; Genesis of the ores of the Zambian Copperbelt, Ore Geology Reviews, v. 6, p. 51-76

Turner, E.C., Broughton, D.W., and Brooks, T., 2018, Neoproterozoic carbonate lithofacies and ore distribution at the Kipushi Cu-Zn deposit, Democratic Republic of Congo, and Gayna River Zn Camp, Northwest Territories, Canada, Economic Geology, v. 113, p. 779-788

Walraven, F., and Chabu, M., 1994; Pb-isotope constraints on base-metal mineralisation at Kipushi (Southeastern Zaïre,), Journal of African Earth Sciences, v. 18, p. 73-82

Whyte, R.J., and Green, M.E., 1971, Geology and palaeogeography of Chibuluma West orebody, Zambian Copperbelt, Economic Geology, v. 66, p. 400- 424

Winfield, O., 1961, Chibuluma, *In:* Mendelsohn, F., (Ed), The Geology of the Northern Rhodesian Copperbelt, Macdonald, London, UK

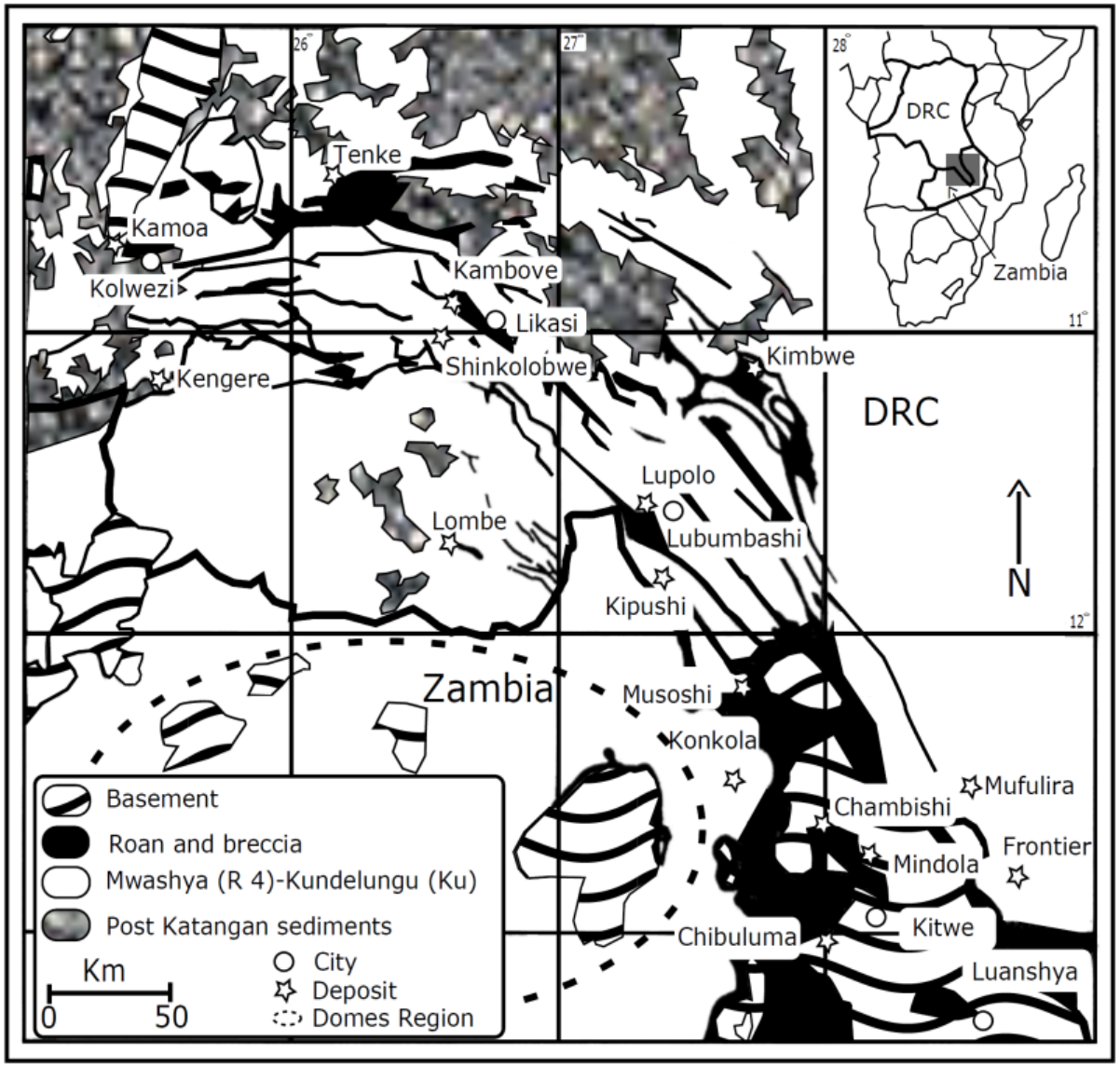

Figure 1.1: Simplified geological map of CAC in the DRC and Zambia (after Annels, et al., 1983; Richards et al., 1988a; Cailteux et al., 1994; Schmandt et al., 2013).

Stratigraphy of Katangan Supergroup, DRC			
Age (Ma)	Group	Sub-group	Formation
< 573	Kundelungu (Ku)	Biano (Ku 3)	
		Ngule (Ku 2)	Sampwe Kiubo Mongwe
		Gombela (Ku 1)	Lududi Kanianga Lusele Kyandamu
635	Nguba (Ng)	Bunkeya (Ng 2)	Monwezi Katete
		Muombe (Ng 1)	Kipushi **Kakontwe (Kipushi** [Ng 1.3.1-1.3.3]) Kaponda **Mwale (Kamoa** Ng 1.1.1)
727	Roan (R)	Mwashya (R 4)	Kanzadi Kafubu Kamoya
		Dipeta (R 3)	Kansuki-R 3.4 Mofya-R 3.3 R 3.2 R.G.S.-R 3.1
		Mines (R 2) **Chibuluma**	Kambove R 2.3 Dolomitic shales R 2.2 Kamoto R 2.1
		R.A.T. (R 1)	
	?		?
> 883	Nchanga Granite and basement		

Figure 1.2: Stratigraphy column of the Katangan Supergroup located in the DRC. Both the Kamoa and Kipushi deposts are located in the Muombe Formation of the Lower Nguba Group (after Winfield, 1961; Armstrong et al., 2005; Heijlen et al., 2008; Kampunzu et al., 2009; Schmandt et al., 2013; Rooney et al., 2015).

2) Sample Description and Geological Context

2.1 Introduction

Standard (30 µm thick) thin sections were made at the University of Alberta Thin Section Lab using drillcore material for both the Kamoa and Kipushi deposits. Petrographic images (Figure 2.1), and all subsequent petrographic observations (including measurements) were produced using a Nikon LV100POL microscope. Figure 2.1A-D are from the Kamoa deposit and are distinguished by greater sulphide diversity, iron oxide staining, and siliciclastic host rock. Figure 2.1E-H are from the Kipushi deposit and display considerable quantities of arsenopyrite, along with chalcopyrite serving as the most common copper ore.

2.2 Petrography of Kamoa and Kipushi

Figure 2.2 presents a summary paragenetic sequence for both Kamoa and Kipushi deposits, along with a volume % abundance for the sulphide phases present. These volume % were determined via point counting using JMicroVision 1.2.7. Images used for point counting are those which are best representative of the sulphide assemblage and contain most or all phases present in one image.

2.2.1 Temperature Constraint at Kipushi

Calcite twin width (w_n) is temperature sensitive, where w_n is proportional to temperature (Ferrill et al., 2004). Conversely, the twin intensity or twin density per area is inversely proportional to temperature. That is, observed twin intensities decrease as temperature increases. Additionally, the shear strain (γ) of calcite can be calculated following Groshong (1972);

$$\gamma = \frac{2}{w_c}\sum_{i=1}^{n}(w_t \tan\frac{\alpha}{2}). \qquad \textit{EQ. 2.1}$$

The width of the twinned carbonate crystal (w_c), width of an individual twin (w_t) and angle between the twinned crystal edge from a reference line (α) are all measurable values. For calcite, $\alpha = 38.28$ (Ferrill et al., 2004). It should be noted that this alpha value was used for both dolomite and calcite strain calculations. Twins were measured relative to an artificial transect oriented parallel to the long axis of the carbonate crystal (Figure 2.3) as in Groshong (1972). Twin width was measured using Nikon NIS-Elements Viewer software. Calcite was distinguished from dolomite, as calcite twins are parallel to the crystallographic c-axis of the crystal (Fairbairn and Hawkes, 1941). Table 2.1 provides measured twin widths, crystal widths, and calculated accompanying shear strain values. The observed twinning in both calcite and dolomite would require at least 200° C (Figure 2.4). While the dolomite may be from the Kakontwe Formation host rock, the temperature constraint pertains to the temperature of deformation. However, the temperature is too high for sediment-hosted diagenetic ore formation (Annels, 1989), allowing for the temperature of deformation to be a minimum temperature proxy of the ore fluid. The measured twins at Kipushi are Type II and Type III and have not been recrystallized (Ferrill et al., 2004). Furthermore, the twinned carbonates are not overprinted by sulphides. These textural observations indicate that the carbonates are either coeval with the sulphide mineralization (dolomite) or post-date the sulphide mineralization (calcite).

Furthermore, the shear strain differences between dolomite (γ= 0.08 and 0.27, mean = 0.15) and calcite ($\gamma = 0.04$) may have tectonic significance. The syn-orogenic dolomite (Re-Os and Pb-Pb Chapter 3 and Chapter 5) has a greater shear strain than the post-ore calcite (Oxygen, Chapter 6). The paragenetic relation between hydrothermal dolomite and hydrothermal calcite support this inference. At Kipushi, dolomite (host rock or hydrothermal) formed prior to hydrothermal calcite (Heijlen et al., 2008; Van Wilderode et al., 2013). The deformation of the

dolomite is associated with the Lufilian orogeny and a compressive stress regime. The shear strain calculations show that calcite experienced a stress lower than the dolomite. Since the shear strain value of dolomite exceeds that of calcite, the dolomite must have been deformed or crystallised prior to the calcite.

2.3 Sample Description and Paragenesis of Chibuluma West, Kamoa, and Kipushi

2.3.1 Generalized Paragenesis of CAC deposits

For stratiform Cu ore deposits, generally the first sulphides to crystallize is pyrite (either pre-ore or syn-ore), followed by chalcopyrite, then higher-grade copper ores (ex: bornite, chalcocite) follow (Brown, 1997). Carbonate is found in the gangue of both Kamoa (Schmandt et al., 2013) and Kipushi (Heijlen et al., 2008; Van Wilderode et al., 2013), although more prevalent in Kipushi (Figs 2.1H, 17G). The reported paragenetic sequences for Kamoa and Kipushi (Figure 2.2) are in general agreement with those published by Schmandt et al., 2013, and Heijlen et al. (2008);Van Wilderode et al. (2013) respectively.

2.3.2 Chibuluma West

Chibuluma West sample NS-137 was obtained from the the University of Tasmania. This sample (1336' from surface) is taken from drillhole NS 137 which is located western edge of the Chibuluma West deposit, and is hosted in a ~3 m thick pyrite-dominant package of the orebody quartzite of the Lower Roan Group, ~150 m above the basement (Selley and Cooke, 2001). At this depth, sulphide is disseminated in a massive sandstone host with corresponding Cu-Co grades of ~ 1%, and ~0.25% respectively (Selley and Cooke, 2001).

Whereas petrographic observations were not made for the Chibuluma West deposit, paragenetic relationships are found in Selley and Cooke (2001)-the results of this study are provided in Figure 2.2. These workers note that the orebody quartzite of the Chibuluma West

deposit experienced a general paragenesis from pyrite → carrolite → chalcopyrite → bornite. Ore sulphides tend to form rims on pyrite, while chalcopyrite and bornite may be found to be in textural equilibrium. Common gangue minerals include albite (whose abundance is inversely proportional to pyrite), biotite, calcite, and chlorite (Selley and Cooke, 2001). Biotite in particular forms as rims on sulphides and is taken as metamorphic in origin, and is either synchronous to ore formation or post-ore. Chlorite and biotite were found in the MI-light fraction (Chapter 3.2.1).

2.3.3 Kamoa

Kamoa sample DKMC-995 was obtained by Dr. Elizabeth Turner at Laurentian University. This sample (~312000 m E/8810000 m N, 35L) was taken from drillhole DD995, located 0.5 km east of the Kamoa Dome-straddling the 1-10 m% and 10-20 m% isograds, and 3 km SE of drillhole DD1445. DKMC-995 corresponds to a depth of 125.26 m below the surface.

The paragenesis for the Kamoa as depicted in Figure 2.2 is in agreement with that provided by Schmandt et al. (2013). The Grand Conglomerate is composed of pre-ore detrital lithic clasts in a fine-grained matrix. In hand sample, >1 cm^2 lithic clasts of carbonate are present. Additional lithic clasts include gneiss and schist (Schmandt et al., 2013). These lithic clasts are detrital and reflect scouring of underlying Katangan sediments or basement rock by the Sturtian glacier. Unoriented, sub-angular to sub-rounded albite and muscovite (Figure 2.1D) are interpreted as detrital grains. Sulphide mineralization begins with diagenetic framboidal pyrite, disseminated throughout the diamictite and predating ore mineralization. Reduced sulphur (needed for the framboidal pyrite) may have formed due to bacterial sulphate reduction (Brown, 1997). Furthermore, Brown (1997) notes that a reduced sulphur source is necessary for stratiform ore formation. The first ore-stage sulphide mineral to precipitate at Kamoa is cubic

pyrite, encasing lithic grains in the Grand Conglomerate. Therefore, Re-Os, and Pb-Pb data obtained from cubic pyrite will be a maximum timing for the age of ore mineralization, as the ore must be younger than or equal to that of the cubic pyrite. The most abundant ore minerals are sphalerite (~14 %), chalcocite (~4 %), and chalcopyrite (~4 %) (Figure 2.2), and post-date the cubic pyrite. Texturally, copper sulphides are found to both rim and replace cubic pyrite (Figures 2.1A, B) (Schmandt et al., 2013). Non-sulphide minerals associated with ore formation include ankerite, biotite, chlorite (Figure 4.4B), muscovite, and quartz (Figure 4.4B) (Schmandt et al., 2013). As mentioned in Chapter 1.3, a supergene enrichment is observed after the main ore formation event at Kamoa. Petrographic evidence of this supergene event is provided in Figure 2.1D, as limonite is found throughout much of the Grand Conglomerate-indicating an oxidizing event after ore formation.

2.3.4 Kipushi

Kipushi sample KPU/081 was obtained by Dr. Elizabeth Turner at Laurentian University. This sample is taken from a depth ranging from 557.3 to 573.85 m through the Big Zinc ore zone (34.9 % Zn) (Turner et al., 2018). On the surface, the Big Zinc is located approximately 100 m south of the Nord-riche, and 200 SE of the Série Récurrente (Kampunzu et al., 2009; Turner et al., 2018). A relative dearth of geological information exists for the unmined Big Zinc (Turner et al., 2018), and it is hoped that this study may, in particular, provide an increased understanding into this sub-region of the Kipushi deposit.

Prior to ore mineralization, sulphur was likely introduced to the Kakontwe Formation via a combination of both dissolved evaporite and BSR (Haest and Muchez, 2011). Arsenopyrite and pyrite are constrained to the initial and syn-ore formation stages. These sulfides were followed by bornite and chalcocite, while chalcopyrite and sphalerite precipitated throughout the

bulk of or mineralization (Figure 2.2). Kipushi contains both disseminated as well as vein-hosted (Figure 2.1F) ore (Turner et al., 2018). Arsenopyrite and pyrite either predate or are coeval with ore mineralization, so the Re-Os and Pb-Pb ages reflect timing maxima like the pyrite from Kamoa. The most abundant ore sulphides are sphalerite (~10 %), chalcopyrite (~7 %), and bornite (~4 %) (Figure 2.2), and can be observed in Figures 2.1E, G. Minor sulphides include briartite ($Cu_2(Zn,Fe)GeS_4$), germanite ($Cu_{26}Fe_4Ge_4S_{32}$), and renierite ($Zn_3(AsO_3)_2$) (Van Wilderode et al., 2013). Molybdenite, a relatively rare mineral (Kampunzu et al., 2009), is however found hosted in veins and formed synchronously with Co-rich chalcopyrite (Intiomale and Oosterbosch, 1974). Gangue minerals are predominately dolomite and quartz (Haest and Muchez, 2011). In addition, elongated phyllosilicates (sericite) formed throughout ore mineralization, and can be intergrown with sulphide minerals (Van Wilderode et al., 2013). The final mineral to crystallize at Kipushi is calcite. It should be noted that <0.5mm^2 disseminations of elemental copper are found in the Kipushi hand samples. Similarly, elemental copper is noted by Schmandt et al. (2013) at the Kamoa deposit and attribute its mineralization to supergene enrichment.

2.4 Conclusion

The paragenesis of the sediment-hosted Kamoa and Kipushi deposits are similar with zinc mineralization predating or coprecipitating with the copper mineralization-which increases in grade over time. A minimum fluid temperature of at least 200° C is required to produce the observed carbonate twin relationships. Shear strain calculations support the paragenetic relations, and the regional stress regimes as ore-stage, syn-orogenic dolomite experienced a greater stress (and resulting strain) than did the post-ore, retrograde? calcite (lower strain).

2.5 References

Annels, A.E., Vaughn, D.J., and Craig, J.R., 1983, Conditions of ore mineral formation in certain Zambian Copperbelt deposits with special reference to the role of cobalt, Mineralium Deposita, v. 18, p. 71-88

Brown, A.C., 1997, World-class sediment-hosted stratiform copper deposits: Characteristics, genetic concepts and metallotects, Australian Journal of Earth Sciences, v. 44, p. 317-328

Fairbairn, H.W., and Hawkes, H.E., JR, 1941, Dolomite orientation in deformed rocks, American Journal of Science, v. 239, p. 617-632

Ferrill, D.A., Morris, A.P., Evans, M.A., Burkhard, M., Groshong, R.H., JR, and Onasch, C.M., 2004, Calcite twin morphology: A low-temperature deformation geothermometer, Journal of Structural Geology, v. 26, p. 1521-1529

Groshong, R.H., JR, 1972, Strain calculated from twinning in calcite, Geological Society of America Bulletin, v. 83, p. 2025-2038

Haest, M., and Muchez, P., 2011, Stratiform and vein-type deposits in the Pan-African orogen in central and southern Africa: Evidence for multiphase mineralization, Geologica Belgica, v. 14, p. 23-44

Heijlen, W., Banks, D.A., Muchez, P. Stensgard, B.M., and Yardley, B.W.D., 2008, The nature of the mineralizing fluids of the Kipushi Zn-Cu deposit, Katanga, Democratic Republic of Congo: Quantitative fluid inclusion analysis using laser ablation ICP-MS and bulk crush-leach methods, Economic Geology, v. 103, p. 1459-1482

Intiomale M, Oosterbosch R (1974) Géologie et Géochemie du gisement de Kipushi Zaire, *In:* Bartholomé, P., (Ed), Gisements stratiformes et provinces cupriféres, Centenaire Société Géologique Belgique, Liége, p 123-164

Kampunzu, A.B., Cailteux, J.L.H., Kamona, A.F., Intiomale, M.M., and Melcher, F., 2009, Sediment-hosted Zn-Pb-Cu deposits in the Central African Copperbelt, Ore Geology Reviews, v. 35, p. 263-297

Selley, D., and Cooke, D., 2001, Mineral zonation and sulfur isotope systematics of the Chibuluma West copper-cobalt deposit, Zambia, AMIRA P544 Progress Report, December, p. 133-169

Schmandt, D., Broughton, D., Hitzman, M.W., Plink-Bjorklund, P. Edwards, D., and Humphrey, J., 2013, The Kamoa copper district, Democratic Republic of the Congo: Stratigraphy, diagenetic and hydrothermal alteration, mineralization, Economic Geology, v. 108, p. 1301-1324

Turner, E.C., Broughton, D.W., and Brooks, T., 2018, Neoproterozoic carbonate lithofacies and ore distribution at the Kipushi Cu-Zn deposit, Democratic Republic of Congo, and Gayna River Zn Camp, Northwest Territories, Canada, Economic Geology, v. 113, p. 779-788

Van Wilderode, J., Heijlen, W., De Muynck, D., Schneider, J., Vanhaecke, and Muchez, P., 2013, The Kipushi Cu-Zn deposit (DR Congo) and its host rocks: A petrographical, stable isotope (O, C) and radiogenic isotope (Sr, Nd) study, Journal of African Earth Sciences, v. 79, p. 143-156

Whyte, R.J., and Green, M.E., 1971, Geology and palaeogeography of Chibuluma West orebody, Zambian Copperbelt, Economic Geology, v. 66, p. 400- 424

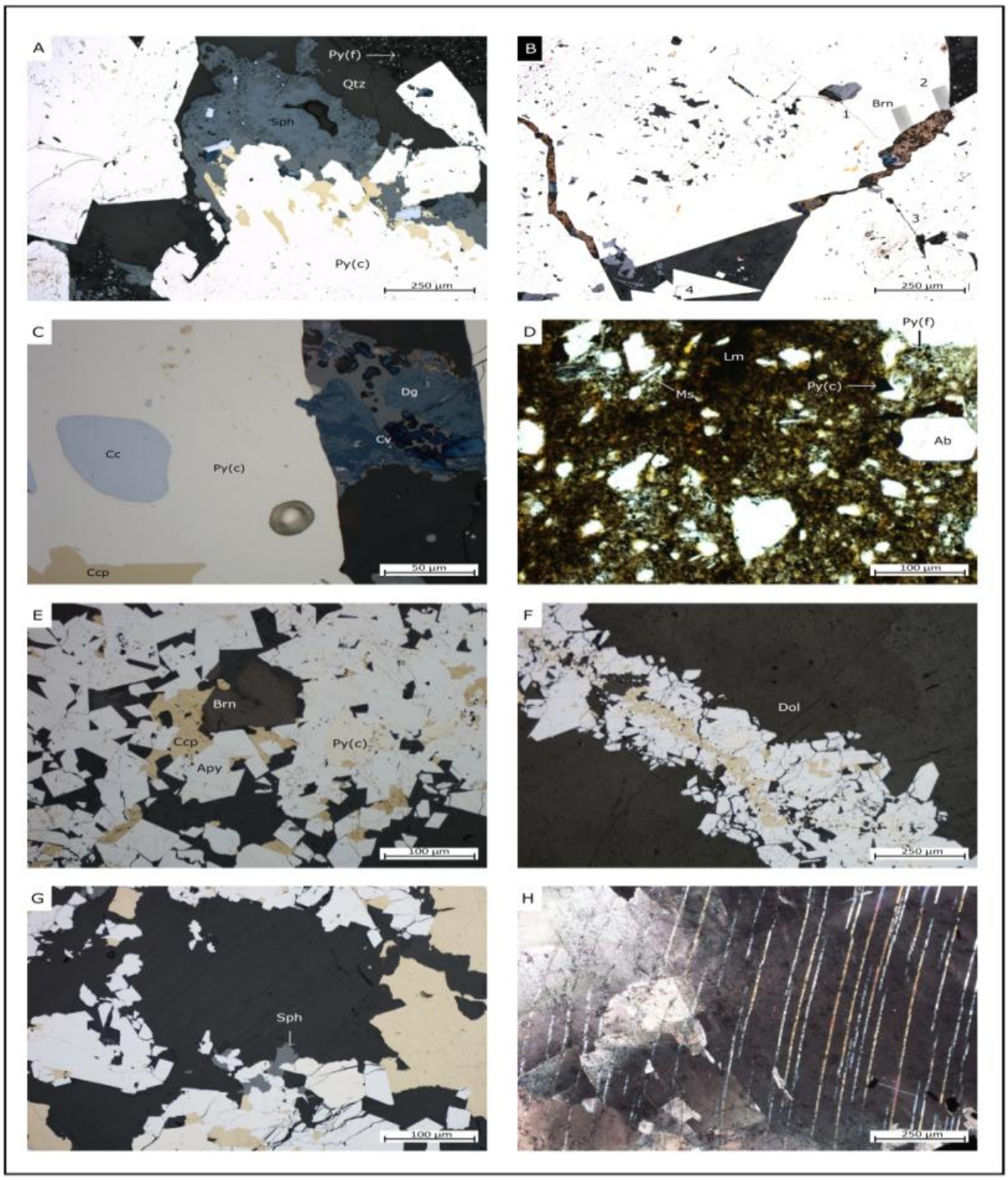
A
Py(f)
Qtz
Sph
Py(c)
250 µm
B
Brn
1
2
3
4
250 µm
C
Dg
Cv
Cc
Py(c)
Ccp
50 µm
D
Py(f)
Lm
Ms
Py(c)
Ab
100 µm
E
Brn
Ccp
Py(c)
Apy
100 µm
F
Dol
250 µm
G
Sph
100 µm
H
250 µm

Figure 2.1: Thin section photomicrographs of sulphide assemblages, host rock, and gangue minerals for the Kamoa (A-D), and Kipushi (E-H) deposits. Mineral abbreviations are as follows, albite (Ab), arsenopyrite (Apy), bornite (Brn), chalcocite (Cc), chalcopyrite (Ccp), chlorite (Chl) covellite (Cv), digenite (Dg), dolomite (Dol), limonite (Lm), muscovite (Ms), pyrite-framboidal (Py-f), pyrite-cubic (Py-c), quartz (Qtz), and sphalerite (Sph). **A)** Grand Conglomerate host rock with diagenetic framboids replaced by ore-stage pyrite and associated sulphide ores and quartz-RL, 50X. **B)** Cubic pyrite cross-cut by quartz + sulphide veinlet. Small fractures (1-4) intersect with but do not cross-cut the sulphide vein-RL, 50 X. **C)** Sulphide-beaing veinlet with covelliite, digenite, and minor bornite-RL, 500X. **D)** Iron-oxide (limonite) coating much of the groundmass in the Grand Conglomerate. Silicates may be of hydrothermal origin or carried by Sturtian glacier-PPL, 100X. **E)** Hydrothermal sulphides overprint the Kakontwe Dolomite-RL + PPL, 100X. **F)** Sulphide vein cross with minor chalcopyrite-RL, 50X**.** **G)** Sulphide assemblage, note fracturing at bottom right-RL, 100X. **H)** Metamorphic twinning of dolomite in the Kakontwe Formation-XPL, 50X

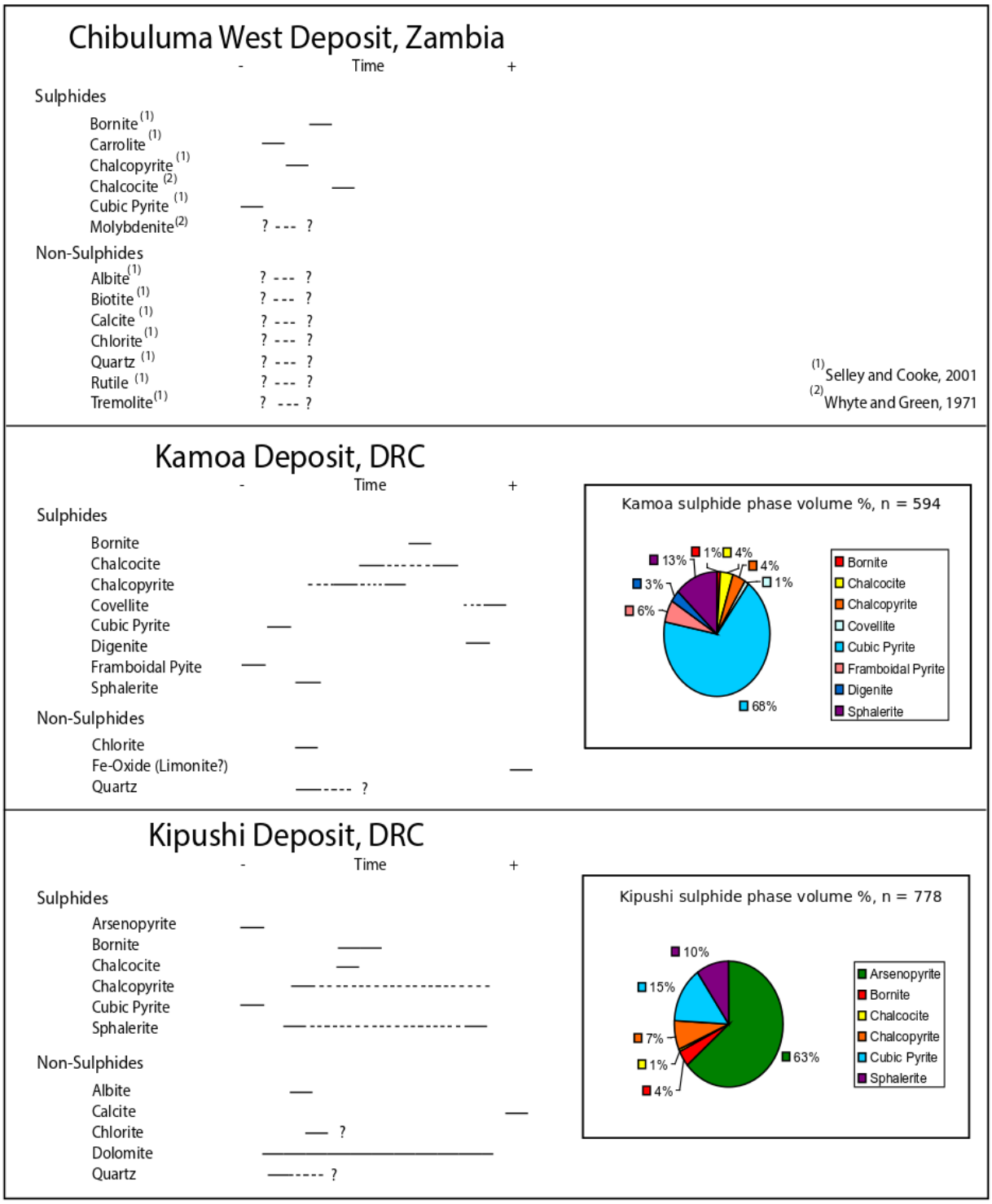

Figure 2.2: Parageneses of sulphide and accessory minerals for the Chibuluma West, Kamoa, and Kipushi deposits, and sulphide-phase volume % for both the Kamoa and Kipushi deposits. Data presented in Chibuluma West paragensis from Whyte and Green (1971); Selley and Cooke

(2001). Relative timings for the non-sulhpides, and molybdenite are not provided, however they are associated with ore mineralization.

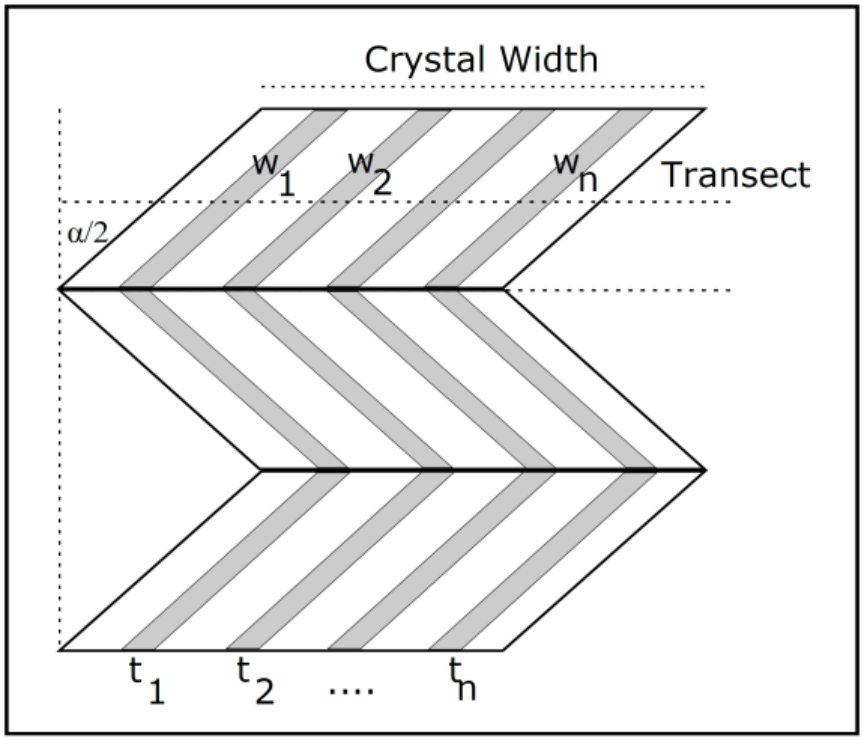

Figure 2.3: Cartoon of twinned carbonate (dolomite). Twins are denoted as t_n with cooresponding twin widths w_n and are measured along a transect datum. The angle (α) of the twinned grain edge to a vertical reference line (Groshong, 1972).

Sample	Twin #	Width of Crystal (µm)	Number of Twins Along Transect	Twin Width (µm)	Twin Width (mm)	Twin Intensity (#/mm)	Shear Strain (γ)
Dolomite 1	1	1679.18	15	27.70	0.02770	8.93	0.13
	2			22.63	0.02263		
	3			22.53	0.02253		
	4			19.76	0.01976		
	5			20.91	0.02091		
	6			20.10	0.02010		
	7			17.80	0.01780		
	8			21.78	0.02178		
	9			22.48	0.02248		
	10			20.46	0.02046		
	11			27.37	0.02737		
	12			29.06	0.02906		
	13			14.44	0.01444		
	14			14.31	0.01431		
	15			13.96	0.01396		
			Mean	**1 σ**	**Minimum**	**Maximum**	
		Width (µm)	21.02	4.53	13.96	29.06	
Calcite1	1	1965.60	11	8.13	0.00813	5.60	0.04
	2			6.44	0.00644		
	3			11.46	0.01146		
	4			11.06	0.01106		
	5			9.17	0.00917		
	6			10.12	0.01012		
	7			11.57	0.01157		
	8			11.01	0.01101		
	9			10.35	0.01035		
	10			12.42	0.01242		
	11			10.00	0.01000		
			Mean	**1 σ**	**Minimum**	**Maximum**	
		Width (µm)	10.16	1.63	6.44	12.42	
Dolomite 2	1	1202.42	22	6.43	0.00643	18.30	0.08

	2			5.69	0.00569		
	3			5.21	0.00521		
	4			5.21	0.00521		
	5			12.55	0.01255		
	6			8.57	0.00857		
	7			4.17	0.00417		
	8			4.17	0.00417		
	9			4.81	0.00481		
	10			7.79	0.00779		
	11			7.97	0.00797		
	12			5.65	0.00565		
	13			9.30	0.00930		
	14			5.00	0.00500		
	15			4.71	0.00471		
	16			8.72	0.00872		
	17			7.43	0.00743		
	18			4.57	0.00457		
	19			5.85	0.00585		
	20			6.33	0.00633		
	21			4.73	0.00473		
	22			6.37	0.00637		
			Mean	**1 σ**	**Minimum**	**Maximum**	
		Width (μm)	6.42	2.02	4.17	12.55	
Dolomite 3	1	2568.81	16	69.17	0.06917	6.228565	0.27
	2			25.64	0.02564		
	3			102.58	0.10258		
	4			62.28	0.06228		
	5			60.45	0.06045		
	6			65.94	0.06594		
	7			75.10	0.07510		
	8			75.10	0.07510		
	9			67.77	0.06777		
	10			67.77	0.06777		
	11			69.61	0.06961		
	12			61.05	0.06105		
	13			47.32	0.04732		
	14			36.63	0.03663		

	15			54.95	0.05495		
	16			62.60	0.06260		
			Mean	**1 σ**	**Minimum**	**Maximum**	
		Width (μm)	62.75	16.6	25.64	102.58	
Dolomite 4	1	1419.73	12	13.09	0.01309	8.452311	0.11
	2			16.07	0.01607		
	3			19.78	0.01978		
	4			13.09	0.01309		
	5			12.81	0.01281		
	6			22.80	0.0228		
	7			23.55	0.02355		
	8			23.61	0.02361		
	9			14.94	0.01494		
	10			16.29	0.01629		
	11			17.33	0.01733		
	12			28.05	0.02805		
			Mean	**1 σ**	**Minimum**	**Maximum**	
		Width (μm)	18.45	5.03	12.81	28.05	

Table 2.1: Measured twin widths, crystal widths, and calculated shear strain values for carbonates from Kipushi thin sections.

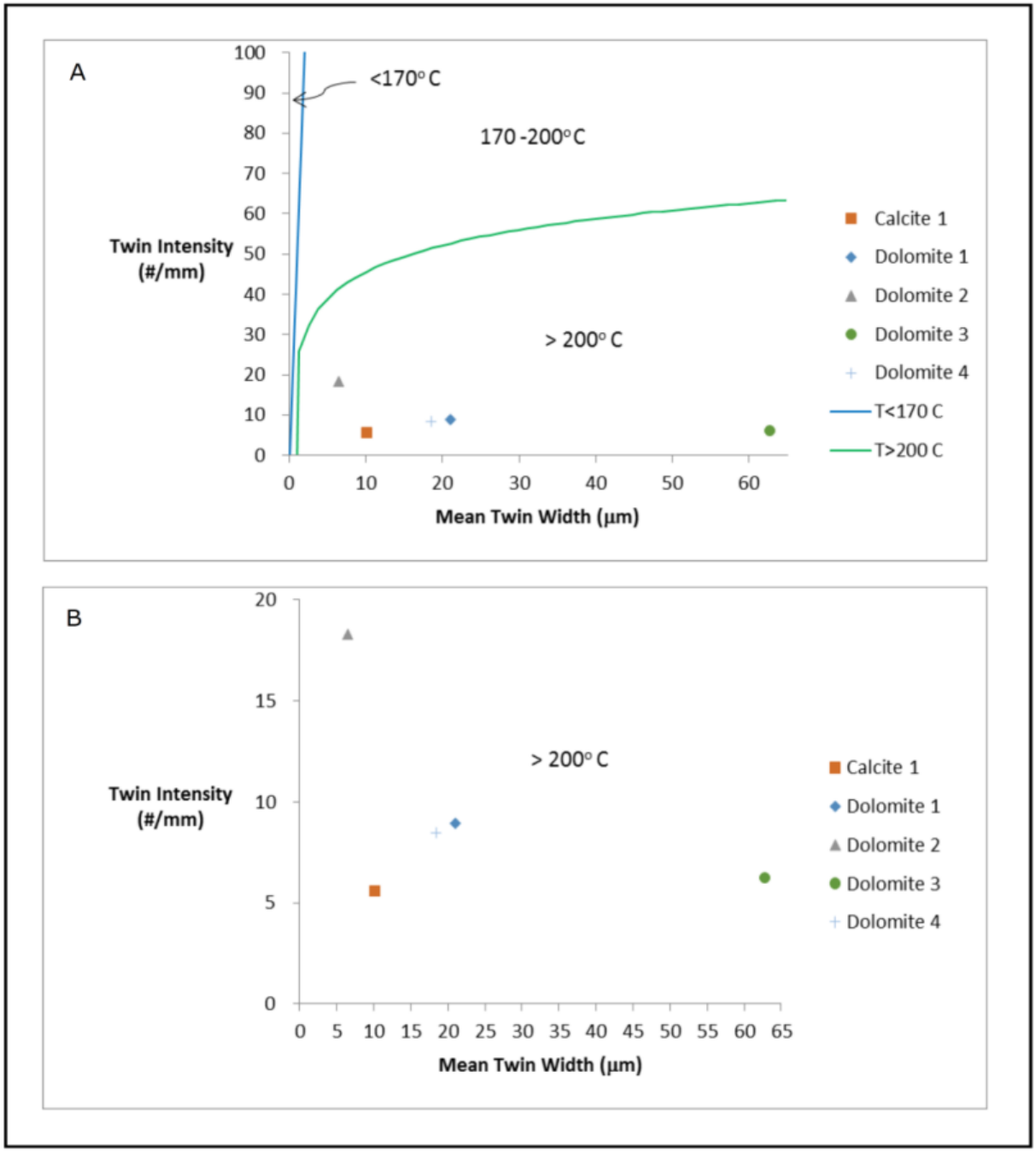

Figure 2.4: Measured carbonate twins and calculated twin intensities from the Kipushi deposit (after Ferrill et al., 2004). **A)** Temperature isopleths of less than 170° C and greater than 200° C are in blue and green respectively. **B)** Entire field shown cooresponds to twins realized at T above 200° C.

3) Re-Os Geochronology

3.1 Background

3.1.1 Introduction

As a relatively new geochronometer, the Re-Os system is particularly well suited for crustal materials given rhenium's moderate fractionation into the crust (Dickin, 1995). Rhenium and osmium readily sequester into iron and copper phases (Dickin, 1995; Richards and Noble, 1998), making the applicability of the Re-Os geochronometer to sulphide ore deposits obvious.

Suitable geochronometers include arsenopyrite, molybdenite, and pyrite (Stein et al., 1998; Morelli et al., 2005; Morelli et al., 2010; Van Acken et al., 2014; Sillitoe et al., 2017). Variable success has been obtained from other sulphides. Molybdenite in particular is an ideal Re-Os geochronometer because on formation contains effectively zero osmium (Creaser, 2015). By excluding common osmium, Re-Os age calculation is simplified. Since there is zero common osmium in molybdenite, isotopic evidence for molybdenite includes an $^{187}Re/^{188}Os > 5000$, $^{187}Os/^{188}Os > 50$, and very high % $^{187}Os^*$ (Stein et al., 2000; Morelli et al., 2010). Furthermore, Mo and Re are closely related, as both elements have similar atomic radii (0.70 and 0.72 Å) respectably, and a 4 + valence. Evidence for high concentrations of Re in molybdenite can be found in Voudouris et al. (2013), where Re was measured at 4.7 wt % (47000 ppm). Given a continental crustal background concentration of ~0.4 ppb Re (Sun et al., 2003), the ability of molybdenite to contain such high amounts of Re is remarkable.

Bornite has also shown to produce high precision (≤0.5 % Re-Os age uncertainty, and 0.2 % Re-Os model age difference) (Box et al., 2015), while chalcocite has not (> 10 % error, and 74 % difference) (Muchez et al., 2015). Recently Re-Os dating results from carrolite have yielded high precision (0.8 % error) ages – providing encouraging prospects for this mineral to directly

date ore formation (Saintilan et al., 2018). The relative purity of mineral separates is not trivial, as Re-Os concentrations vary between sulphides from ppt-level Re (Morelli et al., 2010) to ppm-level (Box et al., 2015; Sillitoe et al., 2017). This implies that the Re-Os age from an impure mineral separate may be meaningless due to signal mixing from numerous sulphide mineral phases (Morelli et al., 2010; Sillitoe et al., 2017).

3.1.2 Previous Re-Os Geochronology of the Chibuluma and Kipushi Deposits

Re-Os dating of deposits in the CAC is relatively recent compared to other isotopic systems. Similar to attempts at dating the CAC in general, Re-Os geochronological results have varied significantly, ranging from pre-Lufilian diagenetic, syn-orogenic, and post-orogenic timings for ore emplacement and are explained in detail in Chapter 1.1. A brief review of the preexisting Re-Os age constraints for the Chibuluma and Kipushi deposits is given below.

Sillitoe et al. (2017) dated unmetamorphosed disseminated molybdenite (molybdenite inclusions are encased by copper sulphide) from the Chibuluma South deposit. The Re-Os model ages of these molybdenite samples are extremely well constrained between 519.3 ± 2.4 Ma to 519.9 ± 2.1 Ma. Vein-hosted molybdenite from the same study yielded a single Re-Os model age of 500.7 ± 2.1 Ma. Ore mineralization therefore took place during the late stage of the Lufilian orogeny (Sillitoe et al., 2017).

Direct dating of Kipushi bornite and renierite returned a Re-Os isochron age of 450.5 ± 3.4 Ma (Schneider et al., 2007). The initial Os ratio was determined to be 0.741 ± 0.23. The ore yields a post-Lufilian timing, while the initial Os ratio suggests a broadly crustal source. These workers invoke the mechanism of mineralization to be the result of an extensional system occurring in the Katangan Basin after the Lufilian orogeny.

3.2 Methodology

3.2.1 Physical Separation

Both Kamoa and Kipushi samples were processed from drill core collected by Dr. Elizabeth Turner at Laurentian University. Chibuluma West samples were obtained from The University of Tasmania and were processed from pre-crushed ~0.5 cm^3 particles.

Whole rock, drill core samples were polished on a Buehler Polimet 1000 to remove any metallic saw particles and (all samples) were summarily crushed in a metal-free agate mortar and pestle. The crushed sample was sieved through the 74 to 210 µm (No. 200, and No. 70 U.S. Sieve Size) non-reusable, non-metallic mesh (Figure 3.1cL), and collected in glass vials (Kuo and Acharya, 2012). Grains in the 74 to 210 µm fraction were separated according to their relative density via methylene iodide (MI, ρ = 3.32 g/cm^3). MI liquid separation effectively isolates silicates and carbonates from sulphides (Figure 3.1dL). Sulphides with densities greater than the MI sank to the bottom of the separation funnel while carbonates and silicates remained in suspension or rose to the top of the MI. Both heavy and light fractions were collected into glass vials. The MI heavy fraction was further separated according to the magnetic susceptibility of the mineral(s) present, using a Frantz LB-1 electromagnet (Figure 3.1eL). A suite of subfractions were produced at varying side-slope angles (^{o}) and currents (A) and each was collected in a new glass vial. The least magnetic subfraction was split under iterative operating conditions unique to each sample. The purpose of this was to achieve an approximately equal volume of magnetic and non-magnetic sample. In general, only the least magnetic (most non-magnetic) samples were used for Re-Os analyses as these contain the highest % pyrite by volume. For additional information regarding magnetic separation, see Appendix 8.1.

Chibuluma West samples were processed identically to the procedure outlined in Figure 3.1aL but without wafering. Ore-stage pyrite, and gangue (carbonate dominant) were the two mineralogies extracted for Re-Os and Pb-Pb analysis. The pyrite will pre-date the Cu ore at Chibuluma West, meaning that the obtained geochronological ages are a maximum age of ore mineralization. The gangue is coeval with the ore mineralization. In the MI light fraction (gangue), a relatively pure (>80 %) fraction containing biotite and chlorite was obtained.

Kamoa samples denoted with suffix "WF" (ex: DKMC-995-145.26-WF4M) are from a single macroscopic ore-stage pyrite ($3cm^3$) cube. This pyrite cube was excised from the drill core with a rock saw (Figure 3.1aL). The cube was sectioned into six wafers using a rock saw (Figure 3.1bL). Kamoa samples denoted with suffix "Cube2" (DKMC-995-145.26-Cube2NM) were taken from a similarly sized pyrite cube also from the same core as WF samples. These samples were un-wafered, but were otherwise processed identically to other Kamoa samples. Cubic, ore-stage pyrite was the only sulphide extracted from the Kamoa bulk rock for Re-Os and Pb-Pb analysis. The pyrite will pre-date the ore at Kamoa, similarly to Chibuluma West.

Kipushi samples were processed similarly to un-wafered Kamoa samples (Figure 3.1aR-dR). The variation in the magnetic susceptibilities (K_m) of chalcopyrite (1.9E-5), arsenopyrite (K_m = 4.5E-6), and pyrite (K_m = 1.0E-6) allowed for extraction of each phase. As minerals often exhibit a range of K_m values, there were some magnetic fractions containing inseparable arsenopyrite and pyrite, and are denoted with "ApyPy". Arsenopyrite, pyrite, chalcopyrite, and carbonate minerals (dolomite and calcite) were separated from Kipushi core for Re-Os and Pb-Pb analysis. These sulphide phases will either predate or directly date ore formation (like at Chibuluma West and Kamoa), while carbonate will date or post-date ore formation.

Given that the host rock of the Kipushi deposit is dolomitic, some pyrite crystals will be attached to carbonate and the bulk density of the composite grain will not exceed that of the MI. This will result in the grain not sinking and not being collected for isotopic analysis. Carbonate dissolution experiments were performed and are explained with results in Appendix 8.2. Further complications arise when particles contain more than one mineral. The resulting magnetic susceptibility of that particle is a weighted average of the phases present. For example, a particle that is 50 % volume pyrite (least magnetic) and 50 % volume chalcopyrite (most magnetic) may occupy the arsenopyrite (intermediate magnetism) magnetic susceptibility domain, despite an absence of this mineral in the particle. Accurate mineralogical composition can be determined by either traditional petrography or by the use of an XRD (X-Ray Diffractometer).

3.2.2 Chemical Separation

Isotopic separation was performed in a Class 100 cleanroom. For ID-TIMS geochronology, all samples were accurately weighed to 0.01 mg (75 – 400 mg depending on Re concentration and mass of available sample) and spiked by standard addition. The spike is an accurately and precisely known mixture of ^{185}Re and ^{190}Os. For samples that are highly radiogenic (^{187}Os/^{188}Os >50) (Stein et al., 2000), a spike enriched in ^{185}Re, ^{188}Os, and ^{190}Os was used to accommodate the diminutive amount of common osmium in the natural sample (Creaser, 2015). Quantification of ^{188}Os is necessary for traditional isochron plots as both ^{187}Re and ^{187}Os are normalized to this stable isotope. Two samples (DKMC-995-145.26-WF6NM, and KPU-081/557.3a4Apy) were treated with 0.5 mL 30 % hydrogen peroxide (H_2O_2) following sample spiking. This additional technique is performed to ensure that all Os in both the sample and spike are equilibrated to the +8 oxidation state as osmium will exist in a variety of oxidation states when dissolved (Morgan et al., 1991; Paul et al., 2009).

The samples and spike were equilibrated in inverse aqua regia in a Carius tube, following procedure outlined by Shirey and Walker (1995); Pearson and Woodland (2000). Due to the low possible blank values that are obtainable from Carius tubes (Pearson and Woodland, 2000), these are the preferred vessel for sample digestion. Equilibration occurs at 220°C for 24 hours. According to Paul et al. (2009) "high temperature" (250°C) digestion is beneficial as it increases chemical kinetics, and aids in total osmium oxidation in both the sample and spike. After digestion, Os is separated from Re by the addition of 3.5 mL of chloroform ($CHCl_3$) to the aqua regia solution, where Os partitions into the chloroform-leaving Re still in aqua regia. The chloroform + osmium solution is treated with hydrobromic acid (HBr), where Os is sequestered and reduced (Os^{8+} to Os^{6+}) into bromine (Br_2) (Birck et al., 1997). Given the volatility of oxidized Os, it should not be exposed in an open-atmosphere environment (Makishima et al., 2001). Reduced Os is purified by microdistillation (Roy-Barman, 1993), using a chromium trioxide and sulphuric acid (CrO_3+H_2SO_4) solution, modified from Walker and Morgan (1989). More than one microdistillation may be necessary due to unknown matrix-effects. Re is initially purified by anion exchange chromatography using DOWEX AGI-X8 resin, and is washed with hydrochloric acid and nitric acid (Morgan et al., 1991). Rhenium is further purified using a single-bead extraction and stripping technique outlined by Selby and Creaser (2003). Procedural mean blank values (n = 6) are 2.21 pg (ppt), and 0.012 pg for Re and Os respectively. The $^{187}Os/^{188}Os$ of the blank is -0.676.

3.2.3 Mass Spectrometry

The purified Re samples were loaded onto degassed Ni filaments after Creaser et al. (2002) in either a barium nitrate and water $Ba(NO_3)_2$ + H_2O solution, or by dissolution in 15 N HNO_3. In the latter case, ~ 0.06 µl (2 applications) of $Ba(NO_3)_2$ activator was applied to the

loaded sample. This activator solution aids in the ionization of Re. Performance differences between both loading techniques were negligible. As such, dissolution and activation may be accomplished together with the $Ba(NO_3)_2$ + H_2O solution. Os samples were dissolved in 9N HBr and loaded onto degassed Pt wire filaments and subsequently treated with ~ 0.06 µl $Ba(OH)_2$ activator (Creaser et al., 2002).

All Re and Os isotopic measurements were produced using a Thermo Scientific Triton in the Canadian Centre for Isotopic Microanalysis (CCIM) at the University of Alberta. Due to the increased ionization efficiency and precision possible for both Re and Os as oxides, chiefly ReO_4^- and OsO_3^- (Creaser et al., 1991; Völkening et al., 1991) negative thermal ionization mass spectrometry (N-TIMS) was performed on all analyses. In addition, $O_{2(g)}$ (Oxygen gas) of known isotopic composition was leaked into the source chamber (P ~2.0^{-7} mbar) to aid in the formation of oxyanions (Birck et al., 1997). Measured Os oxides include $^{192}OsO_3$, $^{190}OsO_3$, $^{189}OsO_3$, $^{188}OsO_3$, $^{187}OsO_3$, and $^{186}OsO_3$ and are normalized to ^{188}Os. These isotopes were made in peak-hopping mode on an electron multiplier. The measured Re oxides include $^{187}ReO_4$, and $^{185}ReO_4$, and in general were made simultaneously using a Faraday cup, although for those samples with very low Re concentrations (~0.5 ppb), isotopic measurement was made using an electron multiplier. Instrument drift was monitored using two standards (for both Re and Os) that were run at the beginning of each analytical session. The isotopic ratios from these standards was compared to a running mean, n >800.

3.3 Results

3.3.1 Calculation of Re-Os Ages

Mono-spiked Re-Os isotopic data for Chibuluma West, Kamoa, and Kipushi samples are provided in Table 3.1, while double-spiked Re-Os isotopic data is provided in Table 3.2. Model ages are calculated using the general equation below, by assuming Os_i values

$$\frac{187}{188}Os_p = \frac{187}{188}Os_i + \frac{187}{187}\frac{Re}{Os}\left(e^{\lambda t} - 1\right). \qquad \textit{EQ. 3.1}$$

The present osmium ($^{187}Os/^{188}Os)_p$ is equal to the sum of the initial osmium ($^{187}Os/^{188}Os)_i$ and the rate of change ($e^{\lambda t}$ -1) of the radioactive parent ($^{187}Re/^{187}Os$). Note that radiogenic ^{187}Os is increased proportionally to time at the expense of radioactive ^{187}Re. When simplified and rearranged for time, Equation 3.1 becomes,

$$t = \frac{\ln\left(\frac{D_p - D_i}{P} + 1\right)}{\lambda}. \qquad \textit{EQ. 3.2}$$

If a suite of samples are coeval, they may be plotted on an isochron diagram. Isochron diagrams were made using ISOPLOT from the measured Re-Os sample data from all three deposits. All isochrons are Model 3 ages and employ the use of an overdispersion term to account for variation in initial osmium. Isochrons for the Chibuluma West, Kamoa, and Kipushi mono-spiked samples are provided in Figures 3.2, 3.3, and 3.4 respectively. For samples excluding initial osmium like molybdenite (Creaser, 2015), Equation 3.2 can be further simplified to;

$$t = \frac{\ln\left(\frac{D_p}{P} + 1\right)}{\lambda}. \qquad \textit{EQ. 3.3}$$

For molybdenite samples (or those samples with molybdenite inclusions) normalization to the stable isotope ^{188}Os is impossible. In this case, all osmium in the molybdenite is radiogenic, and thus a ^{187}Re (ppb) vs ^{187}Os (ppb) comparison may be made. A ^{187}Re vs ^{187}Os plot of Kipushi samples is provided in Figure3.4B-D. As stated previously, this (^{187}Re vs ^{187}Os) plot assumes

that the sole source of ^{187}Re and the resulting ^{187}Os is from molybdenite. These plots force the slope (age) through the origin, as there is zero initial osmium.

3.3.2 Chibuluma West

Chibuluma West samples contain a mean Re concentration of 9.9 ppb, and a mean Os concentration of 62.4 ppt. The pyrite samples contain overall lower Re/Os and Os/Os values than the MI-light (gangue) samples. Mean pyrite $^{187}Re/^{188}Os$ is ~10200, with $^{187}Os/^{188}Os$ of ~96, whereas the MI-light samples have mean $^{187}Re/^{188}Os$ of ~21000, and $^{187}Os/^{188}Os$ of 194. If an $Os_i = 0.5$ is used, pyrite model ages yield a weighted mean of 561 ± 4.0 Ma (n = 5), whereas the MI-light weighted mean age is 543 ± 7.9 Ma (n = 2). Due to the lack of linear spread in the gangue samples, a regression is not possible. However, the model ages ($Os_i = 0.5$) for these two samples are both 557 Ma. When the pyrite samples are regressed, a Model 1 isochron age of 537 ± 22 Ma with $Os_i = 4.4 \pm 3.5$ (MSWD = 1.6) is returned (Figure 3.2A). Similarly, when the pyrite samples and the gangue samples are combined, a robust regression isochron age of 536 +23/-14 Ma is obtained (Figure 3.2B). Robust regressions ignore the assigned error (similar to Model 2), and are preferable if the datasets contains outliers (Vugrinovich, 1981). Indeed, when the upper and lower bounds for this dataset are determined following Vugrinovich (1981), there are two samples (one from the pyrite fraction, and one from the gangue fraction) that fall outside this domain. Therefore, a robust regression is an appropriate choice for the Chibuluma dataset. The measured isotopic ratios for both pyrite and gangue samples exceed the threshold for Low-level Highly Radiogenic (LLHR) classification-discussed further in Chapter 3.4 (Stein et al., 2000).

3.3.3 Kamoa

The mean Re and Os concentrations of Kamoa pyrite are 2.1 ppb, and 19.4 ppt respectively. Additionally, the mean $^{187}Re/^{188}Os$ is 1135, with a mean $^{187}Os/^{188}Os$ of 7. A Model 3 isochron age of 282 ± 34 Ma is obtained for all Kamoa pyrite samples (Figure 3.3A). This isochron has an Os_i = 1.34 ± 0.79, with an MSWD = 781. The high scatter in this isochron is not likely the result of analytical error, but instead of complex pyrite origin, or open system behaviour. If an Os_i = 0.5 is used, all Kamoa samples yield a mean model age of 352 Ma. However, it appears that there are two populations of ages present in the dataset. The oldest of the two contains four pyrite samples with model ages ~458 Ma. These samples return a Model 3 isochron age of 460 ± 100 Ma, and is provided in Figure 3.3B. This isochron has an Os_i = 0.5 ± 1.0, and an MSWD = 12. There is significantly less scatter in this isochron, although the age uncertainty is still very high (>20 %).

3.3.4 Kipushi

There are two dominant sulphide phases analysed at Kipushi; pyrite and arsenopyrite. Mean Re concentrations in arsenopyrite are 12 ppb, with a mean Os concentration of 36 ppt. Pyrite contains noticeably less Re and Os, as the mean Re concentration is 6 ppb, with a mean Os concentration of 17 ppt. Chalcopyrite and bulk carbonate (mostly dolomite) both contain ~ 2 ppb Re. The mean $^{187}Re/^{188}Os$ for arsenopyrite, carbonate, and pyrite are 28400, 29400, 18800, respectively. The mean $^{187}Os/^{188}Os$ for the same minerals are 138, 97, and 95 respectively. In addition, arsenopyrite has 312 times more Re than Os, pyrite has 293 times more Re than Os, and carbonate has 450 times more Re than Os. Similar to the Kamoa Re-Os age results, an imprecise Late Paleozoic timing of ca. 300 Ma results from both the model ages and isochron regressions. However, unlike at Kamoa, the Kipushi Re-Os results are unimodal (~300 Ma ages only). Both

mono-spiked and double-spiked model ages, and their respective isochrons (327 ± 82 Ma, Os_i = -21 ± 43, MSWD = 7.7, and 291 ± 41 Ma, MSWD = 432 respectively) (Figure 3.4A-B, and Figure 3.4C) support a ~300 Ma mineralization for arsenopyrite and pyrite. A composite ^{187}Re vs ^{187}Os plot for both mono-spiked and double-spiked samples also returns an isochron age of 290 ± 25, MSWD = 258 Ma. Mono-spike Re-Os sulphide model ages from Kipushi are unimodal and produced a weighted mean of 288 ± 16 Ma, while the weighted mean for double-spiked Re-Os samples is 313 ± 15 Ma. ^{187}Re vs ^{187}Os plot return older ages due to the assumption that there is zero initial Os in the samples. Upper limit model age constraints can be made when substituting the current $^{187}Os/^{188}Os$ CHUR value of 0.125 (Allégre and Luck, 1980). This is the current, time-evolving Os composition of the mantle, and will yield older ages as a result of a steeper slope in $^{187}Re/^{188}Os$-$^{187}Os/^{188}Os$ space. When the current CHUR value is substituted for initial Os, no model age exceeds 305 Ma for any mono-spiked sample. The oldest sample model age for double-spiked samples is 348 Ma. Lower limit isochron age constraints can be determined by ignoring any negative initial Os value. For example, the mono-spiked samples in Figure 3.4A returned an initial Os ratio of -21 ± 43. The corresponding isochron age (327 ± 82 Ma) can be constrained, as the upper limit of 409 Ma is not reasonable, because the Os_i cannot be negative. Therefore, the true age for this isochron must be equal or less than 327 Ma.

3.4 Discussion

The likely cause for the LLHR observations in the Chibuluma West and Kipushi samples is the presence of molybdenite. The extent of the molybdenite is unknown, although it is possible that the iron sulphides themselves have zero Re, and are therefore irrelevant in the Re-Os results directly. Instead, micron-sized molybdenite inclusions bound within the iron

sulphides are likely the source of the Re-Os results. Molybdenite has been found at the nearby Chibuluma South deposit in close association with Cu mineralization (Sillitoe et al., 2017), and at the Kipushi deposit, where it is associated with Co mineralization (Intiomale and Oosterbosch, 1974). While Schneider et al. (2007) observe highly radiogenic reinerite, these workers do not attribute molybdenite as the source.

If molybdenite is the source of the LLHR sulphides and gangue samples, then determining the paragenetic and petrological context for this mineral is critical to making meaningful age constrains for the ore mineralization. Furthermore, this brings into question the importance of identifying which phase is in fact being dated. Unless prior EPMA or LA-ICP-MS imaging is performed, a "pyrite" Re-Os age may in fact be a molybdenite Re-Os age. This has significant implications for future Re-Os dating of sulphide minerals. For example, if molybdenite is known for a deposit, but it crystallized after the ore, then direct dating of the ore is likely to yield anomalously young ages. In this case, the measured Re and Os are from the molybdenite-not the ore itself. Careful sampling and/or preliminary elemental imaging should be conducted if molybdenite is suspected in the samples at any measureable concentration, and is presented in Chapter 4.

3.4.1 Mineralization at Chibuluma West

Since the gangue samples are paragenetically constrained to the ore, when these two mineralogies are combined, the composite isochron age of 536 +23/-14 Ma is obtained (Figure 3.2B). This age is well within the uncertainty of peak metamorphism ca 530 Ma for the Lufilian orogeny (John et al., 2004) and the pyrite isochron age 537 ± 22 Ma (Figure 3.2C). Considering that the gangue minerals must have been precipitated from the same fluid as the ore-stage pyrite, these two phases are therefore likely in isotopic equilibrium, as their respective isochrons are in

close agreement. The composite isochron age of 536 Ma proves that the ore at the Chibuluma West deposit formed during at or near peak metamorphic conditions during the Lufilian orogeny.

The measured isotopic ratios for both pyrite and gangue samples exceed the threshold for LLHR classification (Stein et al., 2000). Given how radiogenic the Chibuluma West samples are, it may be likely that both the pyrite and gangue contains molybdenite. Despite the density of molybdenite exceeding that of the MI, it is possible that molybdenite is found in the MI-light fraction as a constituent of a bulk grain with a total density less than the MI.

3.4.2 Mineralization at Kamoa

Given that the Kamoa deposit has experienced minimal (if any) metamorphism and contains only stratiform ore (Schmandt et al., 2013), Re-Os age results are critical to assessing when the stratiform ore mineralized. Unlike other CAC deposits which contain cross-cutting veins, Kamoa contains only a stratiform ore, eliminating the possibility of remobilized primary ore. While there is only a single style of ore mineralization at Kamoa, Re-Os ages suggest that there may have been two phases of sulphide mineralization. Including the accompanying error, the oldest of the two mineralization events occurred ~ 460 Ma, and may reflect a cooling phase of the Lufilian orogeny, as similar ages have been noted by Torrealday et al. (2000), and Schneider et al. (2007) for the Kansanshi and Kipushi deposits, respectively. The second, and younger of the two mineralization events occurred ca. 300 Ma is difficult to explain. One possible explanation is that the Katangan Basin experienced fluid mobilization due to a collision at the southern margin of the Gondwana continent in the Late Paleozoic (Daly et al., 1992). Evidence of this possibility is found in the adjacent Cuvette Centrale (Central Basin), located immediately to the north of Katangan sediments. Pre-existing faults within the Cuvette Centrale were reactivated during Permian-Triassic time. If faults located in the Cuvette Centrale were

reactivated, than it is very likely that fluid in the Katangan Basin was mobilized as the Katangan Basin is even closer (~500 Km) to the tectonic front. Furthermore, Schmandt et al. (2013) notes a post-ore supergene event at the Kamoa deposit up to a depth of 250 m. These ~300 Ma Re-Os ages may link the tectonic event to an established supergene mineralization long after primary ore mineralization during the Lufilian orogeny.

3.4.3 Mineralization at Kipushi

It is worth noting that these data alone do not provide any evidence of pre-existing diagenetic ore that was recrystallized during a later mineralization event. Given the unimodal nature of the sulphide ages and despite scatter in the isochron diagrams, the analyzed sulphides from Kipushi crystallized after the Lufilian orogeny. It is possible that the true ore formation for Kipushi is at 450 Ma (Schneider et al., 2007), and these ~300 Ma ages represent an influx of fluid that influenced Re-Os systematics, and are unrelated to the true ore timing. However, the upper bound (mean + 2σ) on the isochron in Figure 3.4A is only 409 Ma, and does not overlap with the expected ~450 Ma timing (Walraven and Chabu, 1994; Schneider et al., 2007). Moreover, the isochron with the highest precision (Figure 3.4B) is 356 ± 13 Ma is younger still.

Perhaps most striking is the similarity of these sulphide ages to the Re-Os age results from Kamoa. The sulphide isochron of the younger Kamoa pyrite is within error of the sulphide isochron from Kipushi. The LLHR nature of the analyzed arsenopyrite and pyrite mineral separates may indicate the presence of molybdenite. Textural relations and locating these molybdenite crystals may elucidate these anomalously young Late Paleozoic ages. If molybdenite is indeed present as inclusions within the arsenopyrite and pyrite samples, and not associated with fractures that cross cut sulphides, some amount of ore mineralization in the Late

Paleozoic cannot be excluded. Conversely, if molybdenite is located in cross cutting fractures, then the obtained Re-Os data is not dating the ore, but an unrelated post-ore event.

3.5 Conclusion

These observations suggest the following:

1. Apparent Re-Os ages recorded by arsenopyrite and pyrite at Kamoa and Kipushi record an event or events at ca. 300 Ma. This event(s) may or may not be associated with ore emplacement, and should be examined carefully (Chapter 4), especially considering the high amount of scatter and imprecision of the isochron ages. Nontheless, despite these unexpected ages, there is no evidence of an age compatible with a diagenetic origin for either deposit, even if a CHUR value is used for Os_i in the model age calculation.
2. A Lufilian timing for ore mineralization is supported by both model ages and isochron method for the Chibuluma West deposit. When the gangue (~540 Ma model ages) samples and sulphide (537 ± 22 Ma isochron age) samples are combined, the composite isochron age of 536 +23/-14 Ma proves isotopic homogeneity between these two phases during ore mineralization, providing excellent constraint for mineralization at Chibuluma West.
3. The LLHR nature for the Chibuluma and Kipushi samples are likely the result of molybdenite. If molybdenite is the source of Re and Os, than determining its distribution, textural relation and paragenetic position relative to the ore is critical to correctly interpreting Re-Os ages (Chapter 4).
4. Overlapping Re-Os model and isochron ages for both the Kamoa and Kipushi deposits may be significant and could provide evidence of a regional fluid in the Nguba Group ca. 300 Ma. The Chibuluma West deposit (Roan Group) appears unaffected.

3.6 References

Allégre, C.J., and Luck, J.M., 1980, Osmium isotopes as petrogenetic and geological tracers, Earth and Planetary Science Letters, v. 48, p. 148-154

Birck, J.L., Roy-Barman, M., and Capmas, F., 1997, Re-Os isotopic measurements at the femtomole level in natural samples, Geostandards Newsletter, v. 20, n.1, p. 19-27

Box, S.E., Syusyura, B., Seltmann, R., Creaser, R.A., Dolgopolova, A., and Zeintek, M.L., 2012, Dzhezkazgan and associated sandstone copper deposits of the Chu-Sarysu Basin, Central Kazakhstan, Economic Geology, Special Publication 16, p. 303-328

Creaser, R.A., Papanastassiou, D.A., and Wasserburg, G.J., 1991, Negative thermal ion mass spectrometry of osmium, rhenium, and iridium, Geochimica et Cosmochimica Acta, v. 55, p. 397-401

Creaser, R.A., Sannigrahi, P., Chacko, T., and Selby, D., 2002, Further evaluation of the Re-Os geochronometer in organic-rich sedimentary rocks: a test of hydrocarbon maturation effects in the Exshaw Formation, Western Canada Sedimentary Basin, Geochimica et Cosmochimica Acta, v. 66, i. 19, p. 3441-3452

Creaser, R.A., 2015, Crustal sulfide minerals (Re-Os), *In:* Rink, W.J., Thompson, J.W., (Eds); Heaman, L.M., Jull, A.J. Timothy, Paces, J.B. (Ass. Eds). Encyclopedia of Scientific Dating Methods, Springer, Dordrecht, Netherlands

Daly, M.C., Lawrence, S.R., Diemu-Tshiband, K., and Matouana, B., 1992, Tectonic evolution of the Cuvette Centrale, Zaire, Journal of the Geological Society, London, v. 149, p. 539-546

Dickin, A.P., 1995, Radiogenic Isotope Geology, Cambridge University Press, UK

El Desouky, H.A., Muchez, P., Boyce, A.J., Schneider, J., Cailteux, J.L.H., Dewaele, S., and Von Quadt, A., 2010, Genesis of sediment-hosted stratiform copper-cobalt mineralization at Luiswishi and Kamoto, Katanga Copperbelt (Democratic Republic of Congo), Mineralium Deposita, v. 45, p. 735-763

Intiomale M, Oosterbosch R (1974) Géologie et Géochemie du gisement de Kipushi Zaire, *In:* Bartholomé, P., (Ed), Gisements stratiformes et provinces cupriféres, Centenaire Société Géologique Belgique, Liége, p 123-164

John, T., Schenk, V., Mezger, K., and Tembo, F., 2004, Timing and PT evolution of whiteschist metamorphism in the Lufilian Arc-Zambezi belt orogen (Zambia): Implications for the assembly of Gondwana, The Journal of Geology, v.112, p. 71-90

Kuo, K. K., and Acharya, R., 2012, Appendix D: Particle Size–U.S. Sieve Size and Tyler Screen Mesh Equivalents, in Applications of Turbulent and Multiphase Combustion, John Wiley & Sons, Inc., Hoboken, NJ, USA

Levasseur, Birck, and Allégre, 1999, Osmium isotopic composition of corals: Evidences for multiple sources, Geochimica et Cosmochimica Acta, v. 63, p. 1335-1345

Ludwig, K.R., 2003, Isoplot/Ex version 3.76, A geochronological toolkit for Microsoft Excel, Berkeley Geochron Canter Special Publication, v. 4, p. 1-43

Makishima, A., Nakanishi, M., and Nakamura, E., 2001, A group separation method for Ruthenium, Palladium, Rhenium, Osmium, Iridium, and Platinum using their bromo complexes and an anion exchange resin, Analytical Chemistry, v. 73, p. 5240-5246

Morgan, J.W., Golightly, D.W., and A.F., Dorrzapf, 1991, Methods for the separation of rhenium, osmium and molybdenum applicable to isotope geochemistry, Talanta, v. 38, p. 259-265

Morelli, R.M., Creaser, R.A., Selby, D., Kontak, D.J., and Horne, R.J., 2005, Rhenium-osmium geochronology of arsenopyrite in Meguma Group gold deposits, Meguma Terrane, Nova Scotia, Canada: Evidence for multiple gold-mineralizing events, Economic Geology, v. 100, p. 1229-1242

Morelli, R.M., Bell, C.C., Creaser, R.A., and Simonetti, A., 2010, Constraints on the genesis of gold mineralization at the Homestake Gold Deposit, Black Hills, South Dakota from rhenium-osmium sulfide geochronology, Mineralium Deposita, v. 45, p. 461-480

Muchez, P., André-Mayer, A.S., El Desouky, H.A., and Reisberg, L., 2015, Diagenetic origin of the stratiform Cu-Co deposit at Kamoto in the Central African Copperbelt, Mineralium Deposita, v. 50, p. 437-447

Paul, M., Reisberg, L., and Vigier, N., 2009, A new method for analysis of osmium isotopes and concentrations in surface and subsurface water samples, Chemical Geology, v. 258, p. 136-144

Pearson, D.G., and Woodland, S.J., 2000, Solvent extraction/anion exchange separation and determination of PGEs (Os, Ir, Pt, Pd, Ru) and Re–Os isotopes in geological samples by isotope dilution ICP-MS, Chemical Geology, v. 165, i. 1-2, p. 87-107

Roy-Barman, M., 1993, Mesure du rapport $^{187}Os/^{186}Os$ dans les basaltes et péridotites: Contributionàla systematique $^{187}Re/^{186}Os$ dans le manteaux, Thesis, Univ. Paris 7

Richards, J.P., and Noble, S.R., 1998, Application of radiogenic isotope systems to the timing and origin of hydrothermal processes, *In:* Richards, J.P., and Larson, J.B., (Eds), Techniques in Hydrothermal Ore Deposits Geology, Reviews in Economic Geology, v. 10, Society of Economic Geologists, Littleton, USA

Saintilan, N.J., Selby, D., Creaser, R.A., and Dewaele, S., 2018, Sulphide Re-Os geochronology links orogenesis, salt and Cu-Co ores in the Central African Copperbelt, Nature Scientific Reports, v. 8, p. 1-8

Schneider, J., Melcher, F., and Brauns, M., 2007, Concordant ages for the giant Kipushi base metal deposit (DR Congo) from direct Rb-Sr and Re-Os dating of sulfides, Mineralium Deposita, v. 42, p. 791-797

Selby, D., and Creaser, R.A., 2003, Re–Os geochronology of organic rich sediments: an evaluation of organic matter analysis methods, Chemical Geology, v. 200, I, 3-4, p. 225-240

Shirey, S.B., and Walker, R.J., 1995, Carius tube digestions for low-blank rhenium–osmium chemistry analysis, Analytical Chemistry, v. 67, p. 2136-2141

Sillitoe, R.H., Perelló, J., Creaser, R.A., Wilton, J., Wilson, A.J., and Dawborn, T., 2017, Age of the Zambian Copperbelt, Mineralium Deposita, v. 52, p. 1245-1268

Stein, H.J., Sundblad, K., Markey, R.J., Morgan, J.W., and Motuza, G., 1998, Re-Os ages for Archaen molybdenite and pyrite, Kuittila-Kivisuo, Finland and Proterozoic molybdenite, Kabeliai, Lithuania: Testing the chronometer in a metamorphic and metasomatic setting, Mineralium Deposita, v. 33, p. 329-345

Stein, H.J., Morgan, J.W., and Scherstén, A., 2000, Re-Os Dating of Low-Level Highly Radiogenic (LLHR) sulfides: The Harnäs Gold Deposit, Southwest Sweden, Records Continental-Scale Tectonic Events, Economic Geology, v. 95, n. 8, p. 1657-1671

Sun, W., Bennett, V.C., Eggins, S.M., Kamenetsky, V.S., and Arculus, R.J., 2003, Enhanced mantle-to-crust rhenium transfer in undegassed arc magmas, Nature, v. 422, p. 294-297

Torrealday, H.I., Hitzman, M.W., Stein, H.J., Markley, R.J., Armstrong, R., and Broughton, D., Re-Os and U-Pb dating of the vein-hosted mineralization at the Kansanshi copper deposit, northern Zambia, Economic Geology, v. 95, p. 1165-1170

Van Acken, D., Su, W., Gao, J., and Creaser, R.A., 2014, Preservation of Re-Os isotope signatures in pyrite throughout low-T, high-P eclogite facies metamorphism, Terra Nova, v. 26, p. 402-407

Völkening, J., Walczyk, T., and Heumann, K.G., 1991, Osmium isotope ratio determinations by negative thermal ionization mass spectrometry, International Journal of Mass Spectrometry and Ion Processes, v. 105, p. 147-159

Voudouris, P., Melfos, V., Spry, P.G., Bindi, L., Moritz, R., Ortelli, M., and Kartal, T., 2013, Extremely Re-rich molybdenite from porphyry Cu-Mo-Au prospects in Northeastern Greece: Mode of occurrence, causes of enrichment, and implications for gold exploration, Minerals, v. 3, p. 165-191

Vugrinovich, R.G., 1981, A distribution-free alternative to least-squares regression and its application to Rb/Sr isochron calculations, Mathematical Geology, v. 13, p. 443-454

Walker, R.J., and Morgan, J.W., 1989, Rhenium-Osmium isotope systematics of carbonaceous chondrites, Science, v. 243, n. 4890, p. 519-522

Walraven, F., and Chabu, M., 1994; Pb-isotope constraints on base-metal mineralisation at Kipushi (Southeastern Zaïre,), Journal of African Earth Sciences, v. 18, p. 73-82

Whyte, R.J., and Green, M.E., 1971, Geology and palaeogeography of Chibuluma West orebody, Zambian Copperbelt, Economic Geology, v. 66, p. 400- 424

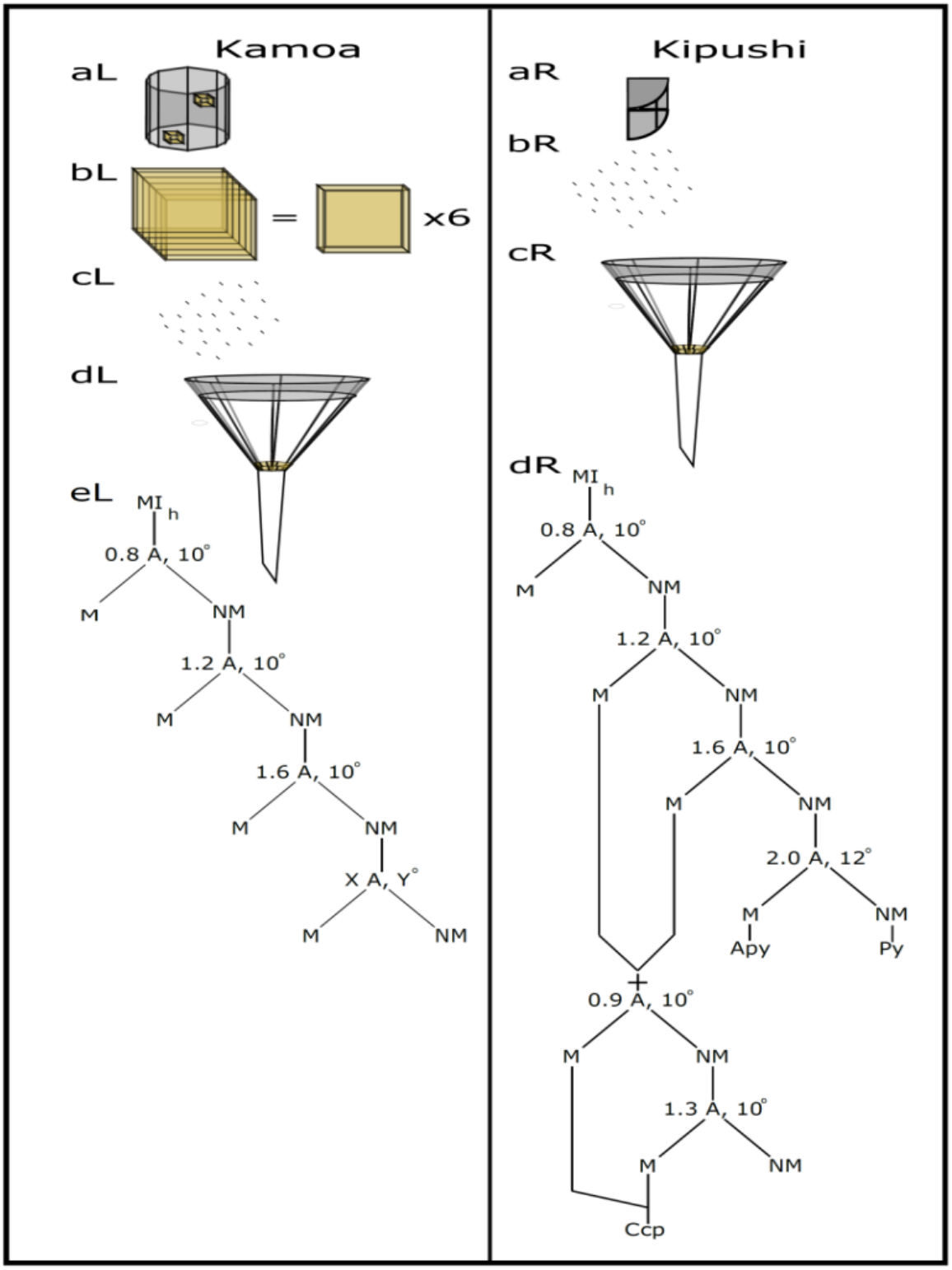

Figure 3.1: Physical separation of both Kamoa (**L**) and Kipushi (**R**) samples.

Sample Name	Isochron Sample Name (Mono/Double, Composite)	Deposit	Dominant Phase(s)
NS137-1336-HP1	1	Chibuluma West	Pyrite
NS137-1336-HP2	2	Chibuluma West	Pyrite
NS137-1336-HP3	3	Chibuluma West	Pyrite
NS137-1336-HP4	4	Chibuluma West	Pyrite
NS137-1336-HP5	5	Chibuluma West	Pyrite
NS137-1336-1-Gg-MIL	6	Chibuluma West	Gangue Minerals
NS137-1336-5-Gg-MIL	7	Chibuluma West	Gangue Minerals
DKMC995-145.26TS#2	1	Kamoa	Pyrite
DKMC995-145.26-WF1M	2	Kamoa	Pyrite
DKMC-995-145.26-WF2M	3	Kamoa	Pyrite
DKMC-995-145.26-WF5M	4	Kamoa	Pyrite
DKMC-995-145.26-WF1NM	5	Kamoa	Pyrite
DKMC-995-145.26-WF3NM	6	Kamoa	Pyrite
DKMC-995-145.26-WF6NM	7	Kamoa	Pyrite
DKMC-995-145.26-WF1M1.6	8	Kamoa	Pyrite
DKMC-995-145.26-WF2M1.2	9	Kamoa	Pyrite
DKMC-995-145.26-WF3M	10	Kamoa	Pyrite
DKMC-995-145.25-WF4M	11	Kamoa	Pyrite
DKMC-995-145.26-WF5M1.2	12	Kamoa	Pyrite
DKMC-995-145.26-Cube2NM	13	Kamoa	Pyrite
DKMC-995-145.26-Cube2M	14	Kamoa	Pyrite
DKMC-995-145.26-Cube2M1.2	15	Kamoa	Pyrite
DKMC-995-145.26-Cube2NM-RPT	16	Kamoa	Pyrite
DKMC-995-145.26-Cube2M-RPT	17	Kamoa	Pyrite
KPU-081/557.3a1Apy	1	Kipushi	Arsenopyrite
KPU-081/557.3a2Apy	2	Kipushi	Arsenopyrite
KPU-081-557.3a1ApyPy	3	Kipushi	Arsenopyrite + Pyrite
KPU-081/557.3a2ApyPy	4	Kipushi	Arsenopyrite + Pyrite
KPU-081/557.3a5ApyPy	5	Kipushi	Arsenopyrite + Pyrite
KPU-081/557.3a6ApyPy	6	Kipushi	Arsenopyrite + Pyrite
KPU-081/557.3a1Carb	7	Kipushi	Carbonate
KPU-081-557.3a1Py	8	Kipushi	Pyrite

Re ppb	± 2σ	Total Os ppt	± 2σ	$^{187}Re/^{188}Os$	± 2σ	$^{187}Os/^{188}Os$	± 2σ	rho
11.0	0.04	70.2	15.3	9749	1620	91.3	15.2	0.997

13.4	0.05	84.9	15.5	10461	1454	98.1	13.7	0.998
9.9	0.04	63.4	18.4	11651	2545	110.7	24.2	0.999
11.2	0.04	70.7	18.6	11935	2367	111.9	22.3	0.997
8.3	0.03	55.6	11.6	7234	1179	69.3	11.3	0.998
10.0	0.04	59.9	4.5	20771	1034	191.2	11.4	0.825
5.4	0.03	31.8	3.2	21716	1574	197.4	14.6	0.979
3.2	0.03	56.1	0.2	411	5	3.8	0.0	0.357
1.3	0.01	10.9	0.2	968	18	5.8	0.2	0.514
1.0	0.01	11.8	0.2	610	17	4.2	0.2	0.544
0.6	0.01	7.6	0.1	622	17	4.5	0.1	0.419
0.8	0.01	5.3	0.1	1655	43	9.8	0.2	0.843
1.2	0.02	22.3	0.7	364	17	3.2	0.3	0.511
0.6	0.01	5.9	0.1	956	20	7.8	0.1	0.643
2.3	0.01	18.9	0.1	956	7	4.9	0.0	0.528
2.3	0.01	19.8	0.1	932	7	5.1	0.0	0.474
0.8	0.01	17.5	0.1	248	4	1.6	0.0	0.309
2.4	0.01	17.3	0.1	1126	10	5.4	0.1	0.518
1.3	0.01	19.8	0.4	450	14	3.7	0.2	0.569
3.0	0.01	14.3	0.2	3067	36	15.4	0.2	0.715
2.7	0.01	16.9	0.2	1126	10	5.4	0.1	0.518
5.7	0.04	48.4	1.9	1095	37	7.2	0.5	0.467
3.0	0.01	14.1	0.4	3126	74	16.1	0.6	0.585
3.0	0.02	23.4	0.4	1592	24	9.8	0.2	0.553
10.9	0.06	34.6	6.5	24111	3017	114.0	17.9	0.797
11.7	0.05	37.8	3.6	32729	2312	161.4	11.5	0.989
11.1	0.05	29.0	3.1	21453	1649	81.2	7.2	0.867
13.3	0.07	44.6	5.2	31089	2583	158.3	14.0	0.939
10.7	0.05	34.5	5.4	40599	4605	201.5	23.2	0.985
9.8	0.05	30.0	5.3	38647	5021	180.7	23.6	0.992
1.9	0.01	4.1	0.6	29423	3047	96.5	10.4	0.960
5.0	0.04	17.1	6.3	18887	4451	94.8	30.4	0.734

^{187}Re ppb	**± 2σ**	**^{187}Os* ppb**	**± 2σ**	**% Re blank**	**%^{187}Os blk**	**%^{188}Os blk**	**Model Age Ma , Os_i =0.5**	**± 2σ**
6.920	0.027	0.064	0.0002	0.17	0.09	41	557	9
8.413	0.033	0.078	0.0002	0.13	0.07	35	557	8
6.244	0.025	0.059	0.0001	0.19	0.10	54	565	8
7.067	0.028	0.066	0.0001	0.16	0.09	49	558	10
5.236	0.021	0.050	0.0002	0.22	0.12	40	568	10
6.262	0.027	0.058	0.0000	0.11	-0.01	3	549	19

3.366	0.016	0.031	0.0000	0.17	-0.02	5	542	9
2.034	0.021	0.016	0.0001	0.55	-0.06	0.3	481	6
0.788	0.006	0.004	0.0001	0.36	-0.06	0.5	330	10
0.613	0.005	0.004	0.0002	0.46	-0.07	0.4	363	16
0.394	0.008	0.003	0.0001	0.98	-0.14	0.9	385	12
0.506	0.006	0.003	0.0000	0.68	-0.12	1.7	338	5
0.756	0.010	0.006	0.0005	0.73	-0.09	0.4	442	39
0.369	0.005	0.003	0.0000	0.76	-0.09	1.1	464	8
1.422	0.008	0.007	0.0000	0.23	-0.05	0.3	282	2
1.462	0.009	0.007	0.0000	0.23	-0.04	0.3	296	2
0.477	0.007	0.002	0.0000	0.78	-0.13	0.3	262	6
1.514	0.008	0.007	0.0001	0.20	-0.04	0.3	258	3
0.788	0.007	0.006	0.0003	0.47	-0.06	0.3	445	20
1.917	0.009	0.009	0.0004	0.15	-0.03	0.7	290	3
1.514	0.008	0.007	0.0001	0.20	-0.04	0.3	334	4
3.593	0.024	0.022	0.0014	0.08	-0.01	0.1	368	24
1.865	0.009	0.009	0.0003	0.16	-0.03	0.7	298	10
2.150	0.010	0.013	0.0003	0.13	-0.02	0.3	349	7
6.861	0.037	0.032	0.003	0.27	-0.05	8	282	27
7.332	0.034	0.036	0.0003	0.19	0.03	8	294	3
7.006	0.033	0.026	0.001	0.20	-0.04	5	225	10
8.359	0.041	0.042	0.001	0.23	0.03	9	304	9
6.702	0.034	0.033	0.001	0.25	0.03	12	297	6
6.161	0.034	0.029	0.0005	0.30	0.04	14	279	5
1.169	0.007	0.004	0.0001	0.31	0.07	11	196	6
3.152	0.023	0.016	0.003	0.43	-0.07	10	299	66

Table 3.1: N-TIMS Re-Os data for the Chibuluma West, Kamoa, and Kipushi deposits, along with calculated model ages for mono-spiked samples.

Sample Name	Isochron Sample Name (Mono/Double, Composite)	Deposit	Dominant Phase(s)
NS137-1336-1-M1.2	-	Chibuluma	Pyrite
NS137-1336-5-M1.2	-	Chibuluma	Pyrite
KPU-081/557.3a3Apy	1, 8	Kipushi	Arsenopyrite
KPU-081/557.3a4Apy	2, 9	Kipushi	Arsenopyrite
KPU-081/557.3a5Apy	3, 10	Kipushi	Arsenopyrite
KPU-081/557.3a3ApyPy	4, 11	Kipushi	Arsenopyrite + Pyrite
KPU-081/557.3a4ApyPy	5, 12	Kipushi	Arsenopyrite + Pyrite
KPU-081/557.3a2Py	6, 13	Kipushi	Pyrite
KPU-081/557.3a3Py	7, 14	Kipushi	Pyrite
KPU-081/557.3a4Py	8, 15	Kipushi	Pyrite
KPU-081/557.3a1Ccp	-	Kipushi	Chalcopyrite

Re ppm	± 2σ	^{187}Re ppb	± 2σ	^{187}Os ppb	± 2σ	Total common Os pg	Model Age Ma	± 2σ, Ma
0.013	4E-05	8.415	0.027	0.083	4E-05	1.632	588	2
0.009	3E-05	5.597	0.021	0.061	4E-05	1.156	647	3
0.012	5E-05	7.431	0.030	0.037	1E-04	0.177	298	2
0.013	6E-05	8.091	0.036	0.040	1E-04	0.166	296	2
0.014	6E-05	8.877	0.036	0.046	2E-04	0.154	313	2
0.016	6E-05	10.039	0.036	0.054	9E-05	0.285	321	2
0.012	6E-05	7.451	0.035	0.038	7E-05	0.120	302	2
0.007	4E-05	4.465	0.023	0.026	8E-05	0.117	348	2
0.007	4E-05	4.182	0.023	0.024	8E-05	0.124	344	2
0.006	3E-05	3.470	0.022	0.019	1E-04	0.116	320	3
0.002	3E-05	1.404	0.019	0.005	3E-05	0.041	230	4

Table 3.2: N-TIMS Re-Os data for Chbiuluma West and Kipushi deposit, along with calculated model ages for double-spiked samples.

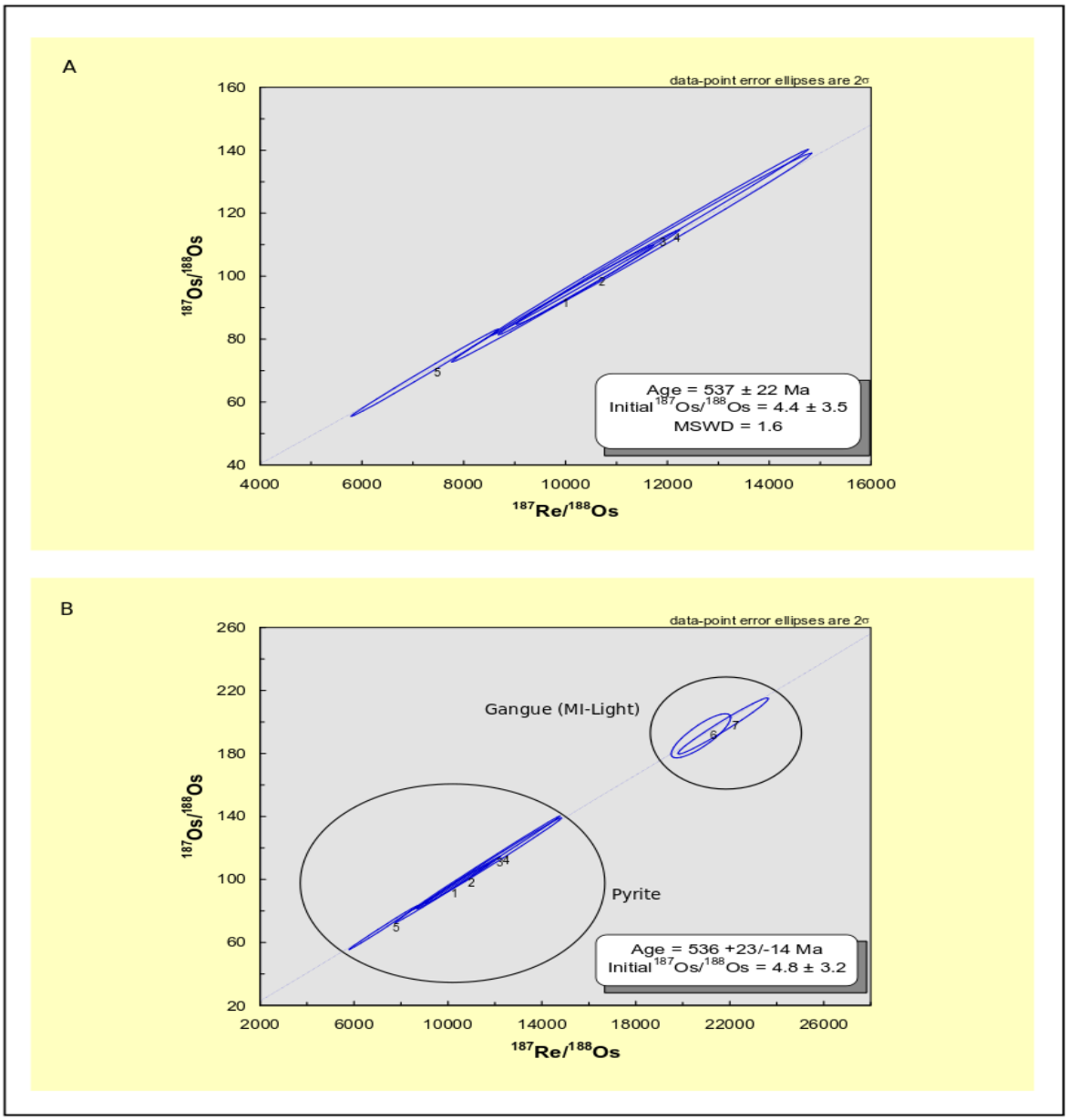

Figure 3.2: Re-Os isochrons (Ludwig, 2003) for gangue and sulphide mienrals from Chibuluma West. Each number adjacent to an error ellipses cooresponds to a sample designated in Table 3.1 **A)** Model 1 isochron of mono-spiked pyrite samples. **B)** Robust regression of combined mono-spiked gangue samples and mono-spiked pyrite samples (MSWD not made when robust regression is calculated).

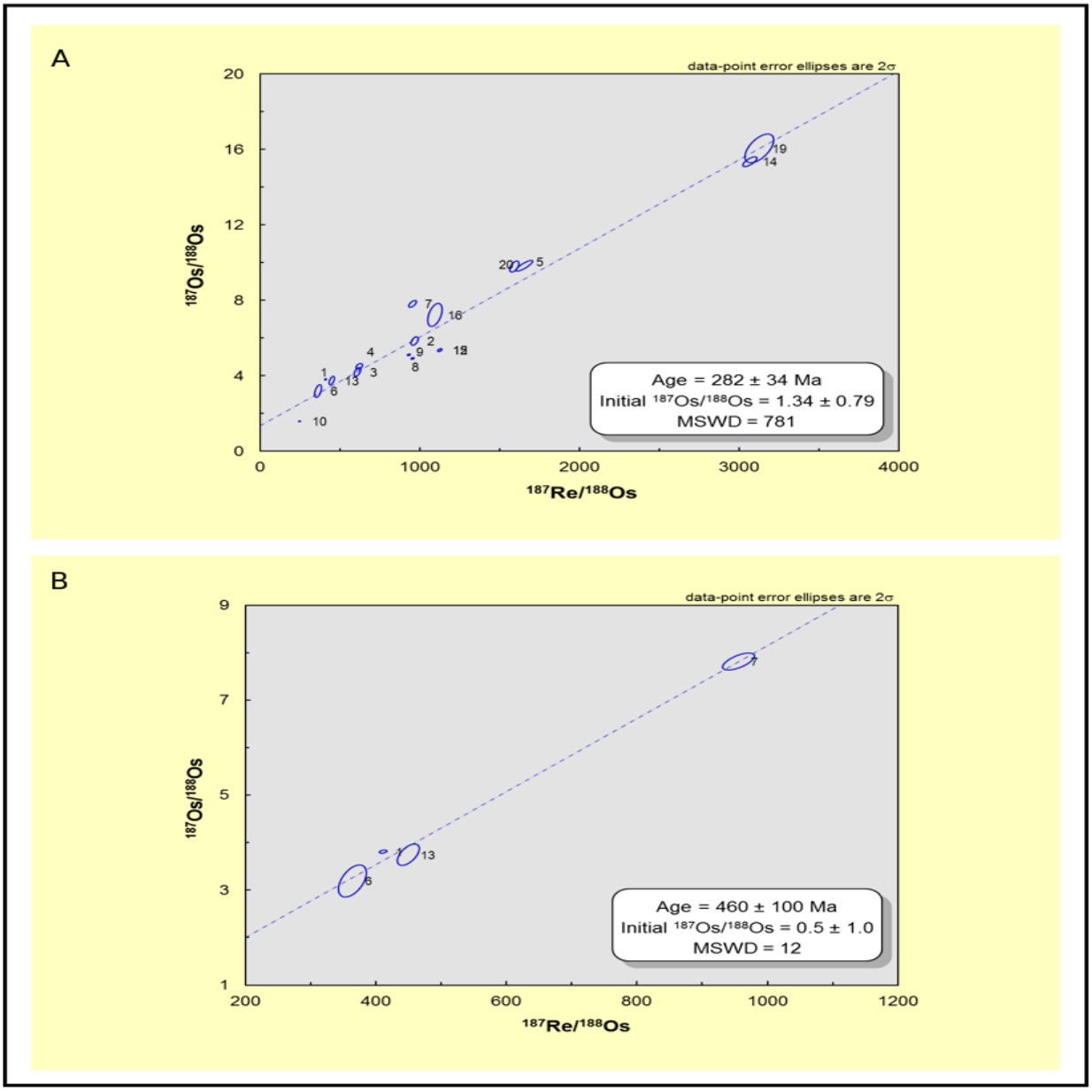

Figure 3.3: Model 3 Re-Os isochrons (Ludwig, 2003) for mono-spiked Kamoa pyrite samples. Each number adjacent to an error ellipses cooresponds to a sample designated in Table 3.1. **A)** Isochron plot for all analyzed Kamoa samples. **B)** Isochron plot for Kamoa samples whose minimum model ages are at least 442 Ma.

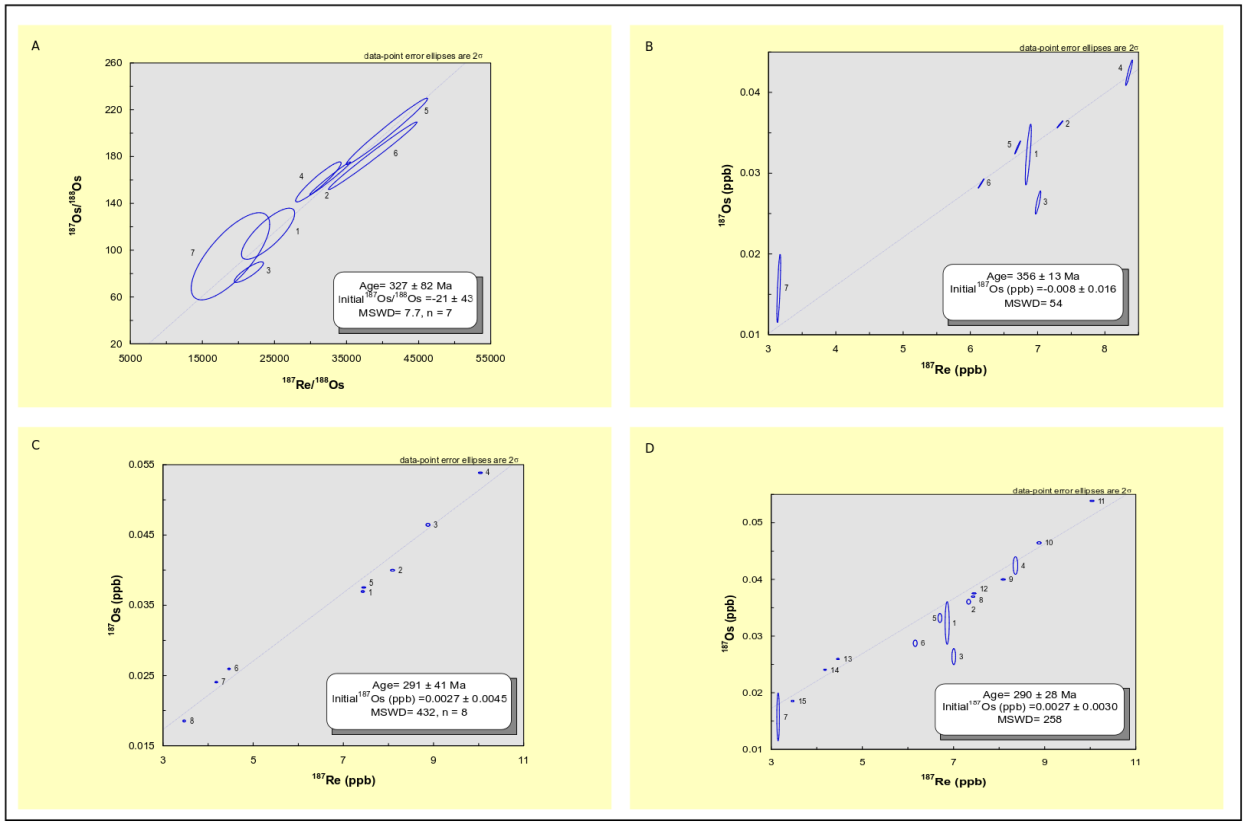

Figure 3.4: Re-Os isotope diagrams (Ludwig, 2003) for sulphide samples from Kipushi. Each number adjacent to an error ellipses cooresponds to a sample designated in Table 3.1. **A)** Model 3 isochron for mono-spiked samples. **B)** ^{187}Re vs ^{187}Os plot of mono-spiked samples. **C)** ^{187}Re vs ^{187}Os plot for double-spiked samples. **D)** Composite ^{187}Re vs ^{187}Os plot for both mono-spiked and double-spiked samples.

4) Molybdenum Distribution and Elemental Imaging

4.1 Background

4.1.1 Introduction and Purpose

A possible explanation for the LLHR nature of Os observed in the iron sulphide and carbonate minerals is due to micron-sized molybdenite inclusions. The occurrence of molybdenite is well established throughout the CAC, particularly in cross-cutting veins (Selley et al., 2005; Torrealday et al., 2000; Sillitoe et al., 2015; Sillitoe et al., 2017). The objective of elemental mapping was twofold, first to establish whether molybdenum, and therefore molybdenite was present in these minerals. The second objective was to characterize the distribution of molybdenum to undertstand it's possible origin in relation to the host sulphide phase. Ultimately, by understanding where the molybdenum is located (fractures, inclusions, grain perimeters), a more meaningful (and geologically plausible) interpretation of the Re-Os data is possible, and in particular the ~300 Ma ages obtained from both Kamoa and Kipushi samples.

These problems can be addressed with the use of electron probe microanalysis (EPMA) or laser ablation inductively coupled plasma mass spectrometry (LA-ICP-MS) techniques. Determining specifically where the Mo, and by inference the Re is located in the analyzed samples may help to understand the high scatter in the Re-Os isochrons and Late Paleozoic ages observed in the Kamoa and Kipushi samples. Furthermore, it may confirm the inferred existence of molybdenite in the Chibuluma West and Kipushi samples.

4.1.2 Choice of Sample Material

The advantage of using thin sections instead of mineral separate grains, is that thin sections provide textural relations which are not available in analysis of single grains. Additionally, due to the much lower LOD obtainable from a laser ablation system, detection of

Mo at trace element (< 100 ppm) concentrations is possible. This advantage is particularly beneficial for Kamoa samples, where molybdenum concentrations are unlikely to be high, given the Re-Os data. However, single grain analysis is beneficial in that it is a direct aliquot of the mineral separate that was used for Re-Os measurement. Identification of molybdenite in or attached to a grain is conclusive evidence that this mineral is affecting the Re-Os data.

4.2 Sampling and Analysis

4.2.1 EPMA

Aliquots of Chibuluma West, Kamoa, and Kipushi mineral separate vials were mounted in standard 2.54 cm diameter epoxy pucks and carbon coated. Single grains from Kamoa and Kipushi were handpicked at random, and grains from Chibuluma Westwere dumped onto the mount. Individual Kamoa and Kipushi grains were selected for X-Ray mapping if the Back Scattered Electron (BSE) images were heterogeneous (elemental variety). Additional considerations include grain fractures, zoning, and inclusions. Grains from Chibuluma West were too abundant for individual mapping, instead a bulk analysis of all grains (NS-137-1336-5-M1.2, n = 173, NS-137-1336-1-M1.2, n = 141) was performed. Analysis of more grains is a better representation of the entire mineral separate population; this however comes at the expense of time.

Qualitative elemental abundances of the chosen grains were determined for As, Co, Fe, Mo, and S were made using a Cameca SX-100 electron probe micro-analyser (EPMA) at the University of Alberta. The characteristic X-ray lines for each element are as follows; As $l\alpha_1$, Co $k\alpha_1$, Fe $k\alpha_1$, Mo $l\beta_1$, and S $k\alpha_1$. Mo $l\beta_1$ was used in lieu of Mo $l\alpha_1$ (2.29316 keV) due to an interference with S $k\alpha$ (2.30784 keV). The current of the fully focused incident beam was maintained at 100 nA. For Chibuluma West grains, the incident beam diameter was 2.0 μm,

while a smaller diameter ranging from 0.3 to 0.7 μm was used depending on grain size for Kamoa and Kipushi samples. The on-peak dwell time for each element was 10 ms.

4.2.2 LA-ICP-MS

Whole rock (30 μm thick) thin sections from the Kamoa and Kipushi deposits were used for major (As, Cu, Fe, and S), minor (Co), and trace (Mo and Re) in situ analysis via LA-ICP-MS. Regions of interest (ROI) or locations for elemental mapping were selected if it was either texturally or mineralogically complex. More specifically, a ROI was selected if it contained a diverse mineralogy, paragenetic diversity (host rock, gangue, sulphide), or fractures. In total, five ROIs were mapped from Kamoa and three ROIs were mapped from Kipushi. These maps are representative of the hand sample and are petrographically diverse.

Elemental mapping was performed using a New Wave Research UP-213 (213 nm) Nd: YAG LA system upstream from a Thermo Scientific ICAP-Q quadrupole QICPMS, located in the CCIM at the University of Alberta. The operating conditions for the LA system were sample dependent. The maps with the lowest Mo backgrounds were made when the ^{95}Mo dwell time was 85 % of the total sweep time (265/300 ms). Additional parameters yielding the best results include matching the spot size (30 μm) with the raster rate (30μm/s) at 67 % power (2.5 J/cm^2) with a laser pulse frequency between 10 to 20 Hz. Two external standards were used during throughout the analysis of each sample map. Sample data was normalized to the primary standard, USGS MASS-1, while a secondary standard, NIST SRM-612 was also used for comparison. Due to the lack of an internal standard, the reported concentrations are semi-quantitative. The frequency of sample raster to standard raster was maintained at a 11:1 ratio. For example, in a 1 mm^2 ROI with a 30 μm spot size, there would be 72 total laser rasters, 66

sample rasters, and 6 standard rasters. Each raster (if 1 mm in length) took 100 s to complete, and consisted of three components, 30 s background, 40 s measurement, and 30 s washout.

Elemental concentrations of samples were calculated by first determining the sensitivity of the Q-ICP-MS. The elemental sensitivity (S_E) of the Q-ICP-MS is expressed as a ratio of the known concentration of an element in a standard (Wilson et al., 2002) to the mean on-peak ($\overline{E_p}$) measured counts per second of the standard. For example, in the case of molybdenum,

$$S_{Mo} = \frac{Mo\ (ppm)}{\overline{Mo_p}\ (cps)}.$$

Then the concentration of an element in a sample may be calculated using Equation 4.1 below,

$$Sample\ (ppm) = S_E * Sample\ (cps). \qquad EQ.\ 4.1$$

It is worth noting that S_E may change on a temporal basis, and pertains only to an individual instrument. For best results, S_E should be determined regularly.

4.3) Results

4.3.1 EPMA Results

BSE and X-Ray results from Kamoa and Kipushi samples are provided in Figure 4.1. BSE and X-Ray results from Chibuluma West are provided in Figure 4.2 and Figure 4.3. The image dimensions have not been modified (resized), to preserve spatial fidelity. It should be noted that these results are strictly qualitative, and serve only to determine the distribution of molybdenite. Comparing the relative intensity between grains should be avoided, as the colour scaling is performed arbitrarily (Goldstein et al., 2003). For example, the same elemental concentration may be present in two discrete grains despite a visual colour difference. If “white” is observed in Grain X, corresponding to concentration A, Grain Y may also have concentration A although it is coloured “black”.

Molybdenite is observed in several of the Chibuluma West pyrite grains. These molybdenite crystals are found both along grain perimeters, and as inclusions within the pyrite. For those molybdenite crystals found along grain perimeters, textural and paragenetic relations cannot be made as the pyrite grains have been mechanically fractured for Re-Os analysis. Additionally, EPMA results show that the existence of non-sulphide phases present in the pyrite mineral separate, as well as significant zoning in Co throughout all grains.

Molybdenum is not detected by EMPA in the Kamoa sample grains (ex: Figure 4.1J). The absence of detectable molybdenum does not mean that there is not any molybdenum present, simply that it is below the LOD for the EPMA. A more sensitive method of analysis such as LA-ICP-MS can overcome this problem due to the much lower LOD (sub-ppm level), however this technique is destructive, and should be performed after initial analysis via microprobe. Kamoa samples are also not compositionally zoned in either As or Co.

A single ~1 μm^2 Mo-rich crystal is located on the grain perimeter in the Kipushi arsenopyrite mineral separate, which is likely to be molybdenite. Similar to those found at grain boundaries in Chibuluma West pyrite, petrological context is missing as the arsenopyrite grain was mechanically fractured. Nonetheless, future laser ablation analysis may assist in gaining an increased understanding of Kipushi molybdenite in relation to ore paragenesis, and the Re-Os results. Both As and Co are zoned in the Kipushi pyrite and arsenopyrite grains.

4.3.2 LA-ICP-MS Results

Raw data was stripped of the background and washout. The true sample signal was integrated from 30 s < t < 70 s using Iolite. A background subtraction correction was performed on all unknown samples using the sample signal from MASS-1 standard (Wilson et al., 2002). The background corrected LA maps are overlain on petrographic images of the same ROI

(Figures 4.1-4.2), allowing for petrological context. Changes in the background concentration are the result of changes to operating conditions to improve spatial resolution and reduce memory effects (smearing). This is due to slow signal washout, resulting in an apparent signal tail. The optimal parameters as explained in Section 4.2 reduced this affect. Additionally, it is possible that by increasing the carrier gas flow rate (> 0.5 L/m), the smearing effects can be further mitigated.

Laser ablation Mo maps are provided in Figure 4.4 and Figure 4.5 for Kamoa and Kipushi respectively. Laser ablation maps of Re and Yb are provided in Figure 4.6 and are compared to the Mo distribution of Area 3 in Figure 4.5.

Due to the decreased LOD of the LA-ICP-MS compared with EMPA, Mo can be successfully detected in the Kamoa thin section. Mo concentration throughout the Kamoa whole rock varies over three orders of magnitude (0.2 to 100 ppm), and even at the maximum concentration would still be too low for EPMA detection. Molybdenum is found in three distinct settings in the Kamoa whole rock sample. Molybdenum is found in the Grand Conglomerate host rock, as disseminated inclusions within ore-stage pyrite, and is strongly associated with veins and fractures that cross-cut the ore-stage pyrite.

Molybdenum is distributed similarly throughout the Kipushi whole rock. It is found as disseminated inclusions within ore-stage sulphide, and in close association with fractures. Molybdenum does not appear to be located in the Kipushi gangue (dolomite), although this may in fact be the host rock (dolomite). In either case, molybdenum does not appear to be found in carbonate.

4.4 Discussion

4.4.1 Chibuluma West Mo Distribution

Given that molybdenite is located both within pyrite as inclusions, and along grain perimeters, it may be assumed that the molybdenite either precipitated with or after the ore at Chibuluma West. That is, there is no evidence that molybdenite is found in non-sulphide phases (arenite host rock). This important observation allows the Re-Os ages to be bracketed as maximums for mineralization. The identified molybdenite can only have formed concurrently with the ore mineralization at Chibuluma West. Since pyrite was the first sulphide to precipitate during ore deposition (Chapter 2.3.2), the 537 Ma Re-Os timing dates the initial phase of ore emplacement. In other words, pyrite-hosted molybdenite precipitated prior to, but from the same fluid as the Cu-Co ore. Furthermore, the high precision of the Re-Os data suggests that a single fluid precipitated the ores of the Chibuluma West deposit. This observation in turn requires that all molybdenite (source of Re-Os data) to be coeval, making the molybdenite found along grain perimeters syn-ore. The identification of molybdenite confirms the LLHR nature obtained from the Re-Os data, and is the source of the Re-Os data itself.

4.4.2 Kamoa Mo Distribution

There is very little Mo in both the Kamoa pyrite, or sphalerite or chalcopyrite (Figure 4.1A). Moreover, there is almost no molybdenite found in the Kamoa samples, with the exception of one possible molybdenite crystal (nugget effect) located in the groundmass of Area 2 of Figure 4.4B.

The ore-stage (cubic) pyrite in Area 6 of Figure 4.4B displays an overall Mo concentration of 0.4 ppm. This low concentration is found throughout the entire cubic pyrite crystal (in the FOV). This implies that the Re is also located in the cubic pyrite. If this inference is correct, than the Re-Os age is in part derived from the ore-stage pyrite. Mo is also found at concentrations ~2.3 times greater (0.9 ppm) in fractures which cross-cut the ore-stage pyrite

(Figure 4.4C). Any Re (therefore Re-Os age results) associated with this Mo distribution will post-date pyrite formation. It is possible that the ~300 Ma Re-Os pyrite ages are derived from this type of Mo distribution.

Taken together, these two styles of Mo distribution indicate that the Re-Os analysis of Kamoa pyrite is a bulk composition. The relatively older Mo distributed throughout the cubic pyrite and the relatively younger Mo distributed in cross cutting fractures likely explains the high degree of scatter in the isochrons (MSWD = 781) as well as the range of model ages (481 to 258 Ma). The maximum and minimum model ages provide age estimates for the Mo deposition in both ore-stage pyrite, and in the fractures respectively. The older ~460 Ma Re-Os isochron may result from of a greater abundance of fracture-free pyrite, whereas the younger ~300 Ma Re-Os pyrite model ages conversely may be dominated by Mo found in post-ore fractures.

Considering the scatter in the ~300 Ma isochron, and the high age uncertainty in the ~460 Ma isochron are affected by variation in the Os_i, by identifying locations void of Mo (and thus Re), the phases containing common Os (non-radiogenic, ie ^{188}Os) may be constrained. For example, the hydrothermal chlorite, quartz, and sphalerite that rim the large cubic pyrite, do not contain Mo (Areas 2, 6 Figure 4.4B), nor does the quartz + biotite veinlet (Areas 1, 5 Figure 4.4A). Since these phases are void of molybdenum, then they are not likely to be radiogenic, and thus may be the source of the common Os.

4.4.3 Kipushi Mo Distribution

A single crystal of high-Mo – likely molybdenite was identified in the Kipushi arsenopyrite mineral separate (Figure 4.1B). Despite this, its location on the edge of a pyrite grain makes interpretation of the geochronological results difficult. The molybdenite may be located on a cleavage plane or in a fracture. If so, then the young (~300 Ma) Re-Os ages are

dating this post-ore event. Therefore, it is imperative to characterize its petrological relation to the host grain, and thus the ore. Regardless, the identification of molybdenite corroborates the LLHR findings.

Upon closer inspection via LA-ICP-MS, molybdenum appears to be strongly associated with fractures and small veins which cross cut ore-stage sulphide (Figure 4.5). Molybdenum does not appear to be in association with gangue mineralization (Figure 4.5A), or as inclusions in copper sulphide (Figure 4.5C). These textural observations corroborate the Re-Os results, as the ca 300 Ma ages are the result of a post-ore fluid bearing Mo, and by inference Re. This Mo then precipitated along these cross-cutting fractures, possibly as fine molybdenite crystals

4.4.4 Zoning of Major and Minor Elements

The pyrite mineral separate from Chibuluma West (Figure 4.2D and Figure 4.3D) displays noticeable Co zoning, implying that the ore-stage pyrite did not experience post-ore metamorphism. If the primary ore mineralization were later disturbed, these delicate zoning textures would have been erased. This critical observation corroborates the Re-Os data, and supports a Lufilian timing of ore mineralization for the Chibuluma West deposit, rather than a pre-Lufilian or diagenetic origin of this pyrite.

The pyrite grains from Kamoa are not zoned in As or Co (Figure 4.1K and Figure 4.1L). This suggests that the precipitating fluid did not evolve with time given that the deposit is effectively unmetamorphosed (with respect to these two elements), and that mineralization took place under similar conditions, possibly in a single event (ref). Sulphides from Kipushi are zoned in As, and Co (Figure 4.1C and Figure 4.1G). This zoning is observed in both pyrite and arsenopyrite mineral separates. Similar to the observations made for Co, As zoning is complex

and indicates that these sulphides (and ores) have not been rehomogenized since the zoning is retained.

4.4.5 Elemental Correlations

Mo is an excellent tracer for Re, and is used as a proxy for the source of Re and hence the source of radiogenic Os in a sample. As an example, Figure 4.6 visualizes this elemental correlation in the Kipushi thin section KPU-081/557.3. Mo (Figure 4.6A) and Re (Figure 4.6B) are clearly correlated. It is worth mentioning that Mo in the top frame of Figure 4.6A is not macroscopic crystals of molybdenite, but instead elevated (above background) concentrations of Mo. Instead, molybdenite is located in the bottom frame of Figure 4.6A. Nonetheless, these two elements are clearly spatially related and concentrate most heavily alongside other sulphides and not the gangue minerals or host rock. Indeed Re and Mo possess a pairwise probability of 31.17 % (for further discussion see Appendix 8.5). Furthermore, Co may serve as a useful tracer for both Mo and Re. If only a background correction is applied the P for Co:Mo and Co:Re is 33.59 % and 27.42 % respectively. Pairwise comparisons for Co:Mo, Re:Co, Re:Mo are provided in Table 4.1.

4.5 Conclusion

Molybdenite was found in the Chibuluma West ore-stage pyrite. Both molybdenite and molybdenum are found in the arsenopyrite mineral separate, and throughout arsenopyrite and pyrite in Kipushi samples. Molybdenite is likel y present in the Grand Conglomerate host rock and as inclusions within pyrite (nugget effect) at the Kamoa deposit. Molybdenum is found in close association with cross-cutting, post-ore fractures and as inclusions within ore-stage sulphide at both Kamoa and Kipushi deposits. Co is zoned in the Chibuluma West pyrite mineral separate. While both As and Co are zoned in the Kipushi arsenopyrite and pyrite

mineral separates. Zoning at both of these deposits indicates that these sulphides have retained the primary As and or Co ore zoning, and are not overprinted post-ore formation. Kamoa pyrite is not zoned, although considering that only stratiform ore is found at this deposit, a single mineralization is still evident. The proposal that the Re-Os data from Chibuluma West relates to molybdenite is corroborated by the Mo mapping results.

The Late Paleozoic Re-Os ages for the Kamoa and Kipushi deposits are likely derived from the Mo-rich areas found in crosscutting fractures. The ca 460 Ma Re-Os age for pyrite from Kamoa may be real, considering that molybdenum is also found as distributed within ore-stage pyrite, and not along grain boundaries or fractures. However, the molybdenum located within the crosscutting fractures may have formed as a result from fluid migration due to the collisional event at the southern margin of Gondwana in the Late Paleozoic (Daly et al., 1992). The crosscutting fractures in turn, may be the source of the ~300 Ma Re-Os model ages and isochrons. Nonetheless, further evidence is needed to evaluate this particular age. Co has shown to be a very good indicator for Re and Mo, and may serve as a useful tracer for these elements for future laser ablation mapping, and characterization of Re distribution in a sample.

4.6 References

Daly, M.C., Lawrence, S.R., Diemu-Tshiband, K., and Matouana, B., 1992, Tectonic evolution of the Cuvette Centrale, Zaire, Journal of the Geological Society, London, v. 149, p. 539-546

Goldstein, J.I., Newbury, D.E., Joy, D.C., Lyman, C.E., Echlin, P., Lifshin, E., Sawyer, L., and Michael, J.R., 2003, Scanning Electron Microscopy and X-Ray Microanalysis, Kluwer Academic/Plenum Publishers, New York, USA, p. 673

Potts, P.J., 1992, A Handbook of Silicate Rock Analysis, Blackie, Glasgow, UK, p. 622

Selley, D., Broughton, D., Scott, R., Hitzman, M., Bull, S., Large, R., McGoldrick, P., Croaker, M., and Pollington, N., 2005, A new look at the geology of the Zambian Copperbelt, Economic Geology 100th Anniversary Volume, v. 29, p. 485-522

Sillitoe, R.H., Perelló, J., Creaser, R.A., Wilton, J., and Dawborn, T., 2015, Two ages of copper mineralization in the Mwombezhi Dome, northwestern Zambia: Metallogenic implications for the Central African Copperbelt, Economic Geology, v. 110, p. 1917-1923

Sillitoe, R.H., Perelló, J., Creaser, R.A., Wilton, J., Wilson, A.J., and Dawborn, T., 2017, Age of the Zambian Copperbelt, Mineralium Deposita, v. 52, p. 1245-1268

Torrealday, H.I., Hitzman, M.W., Stein, H.J., Markley, R.J., Armstrong, R., and Broughton, D., Re-Os and U-Pb dating of the vein-hosted mineralization at the Kansanshi copper deposit, northern Zambia, Economic Geology, v. 95, p. 1165-1170

Wilson, S.A., Ridley, W.I., and Koenig, A.E., 2002, Development of sulfide calibration standards for the laser ablation inductively-coupled plasma mass spectrometry technique, Journal of Analytical Atomic Spectrometry, v. 17, p. 406-409

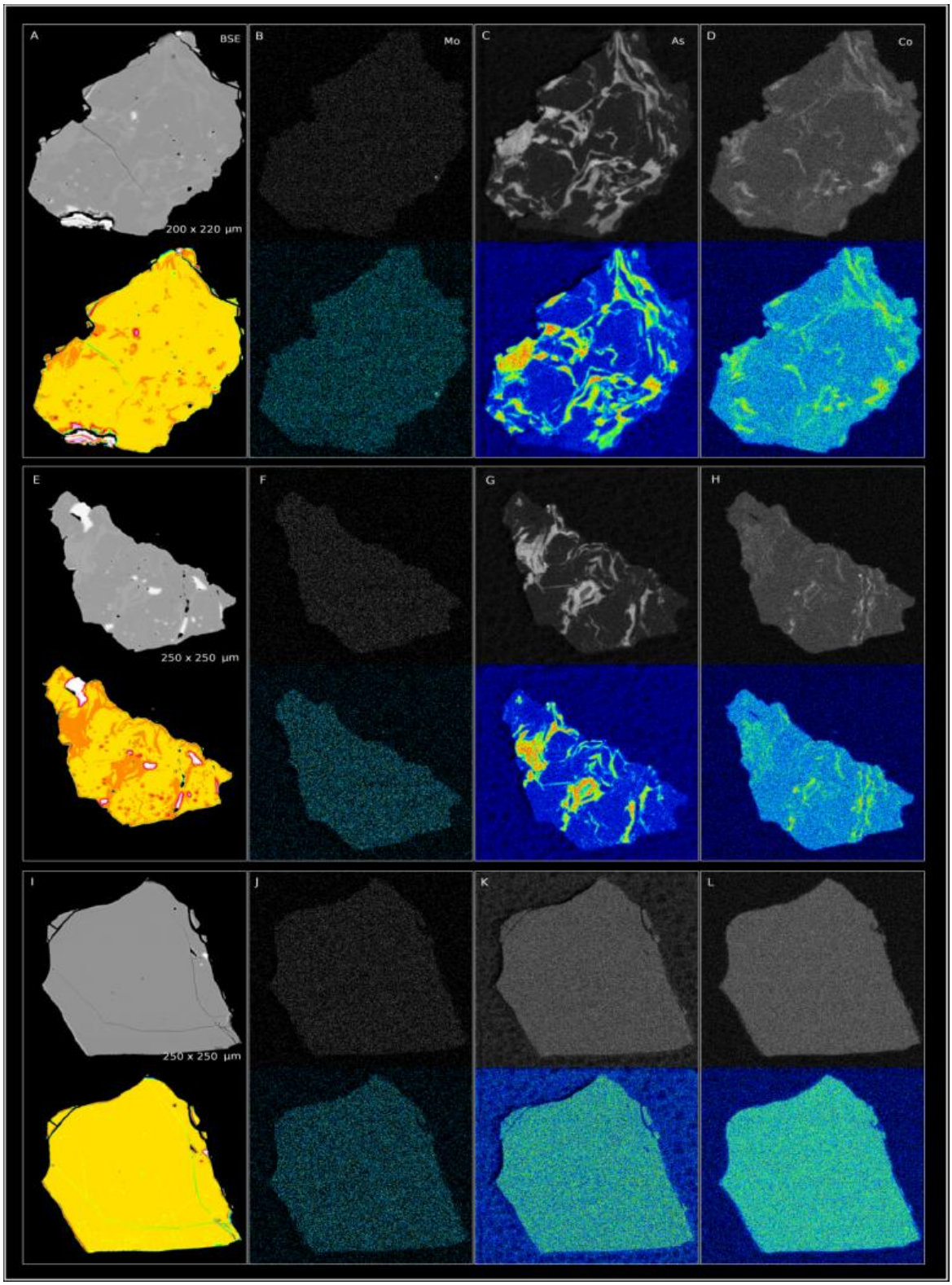
A
BSE
200 x 220 µm
B
Mo
C
As
D
Co
E
250 x 250 µm
F
G
H
I
250 x 250 µm
J
K
L

Figure 4.1: EPMA images of Kamoa and Kipushi single grains. Panels A-D are of a single grain from Kipushi sample, a1Apy. Panels E-H are of a single grain from Kipushi, sample a1Py. Panels I-L are a of a single grain from Kamoa, sample WF6NM. **A,E,I)** BSE and color enhanced images. **B,F,J)** Mo X-Ray and color enhanced images. **C,G,K)** As X-Ray and color enhanced images. **D,H,L)** Co X-Ray and color enhanced images.

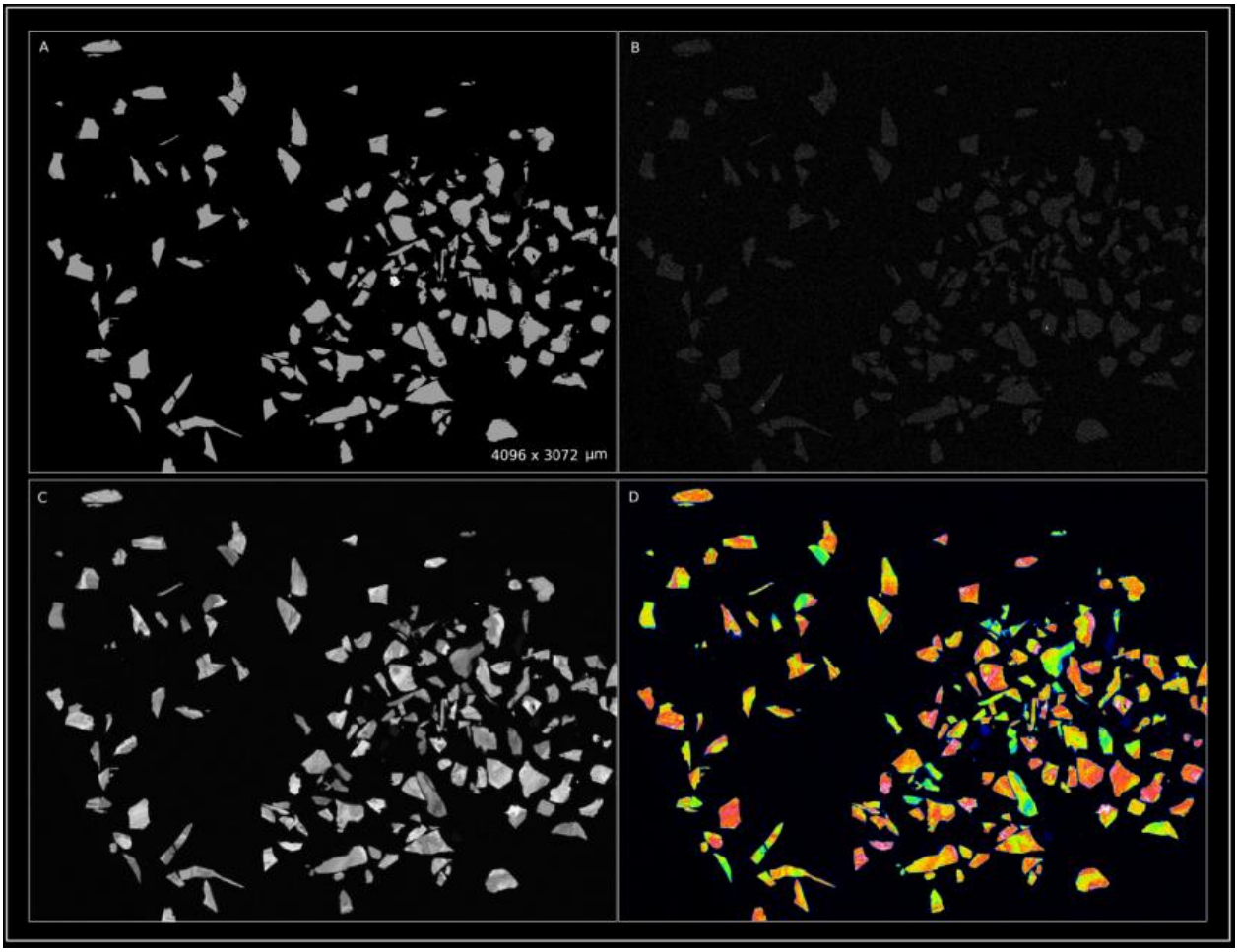

Figure 4.2: EPMA images of Chibuluma West sample NS-137-1336-5-M1.2. **A)** BSE image. **B)** Mo X-Ray image. **C)** Co X-Ray image. **D)** Co X-Ray color enhanced image.

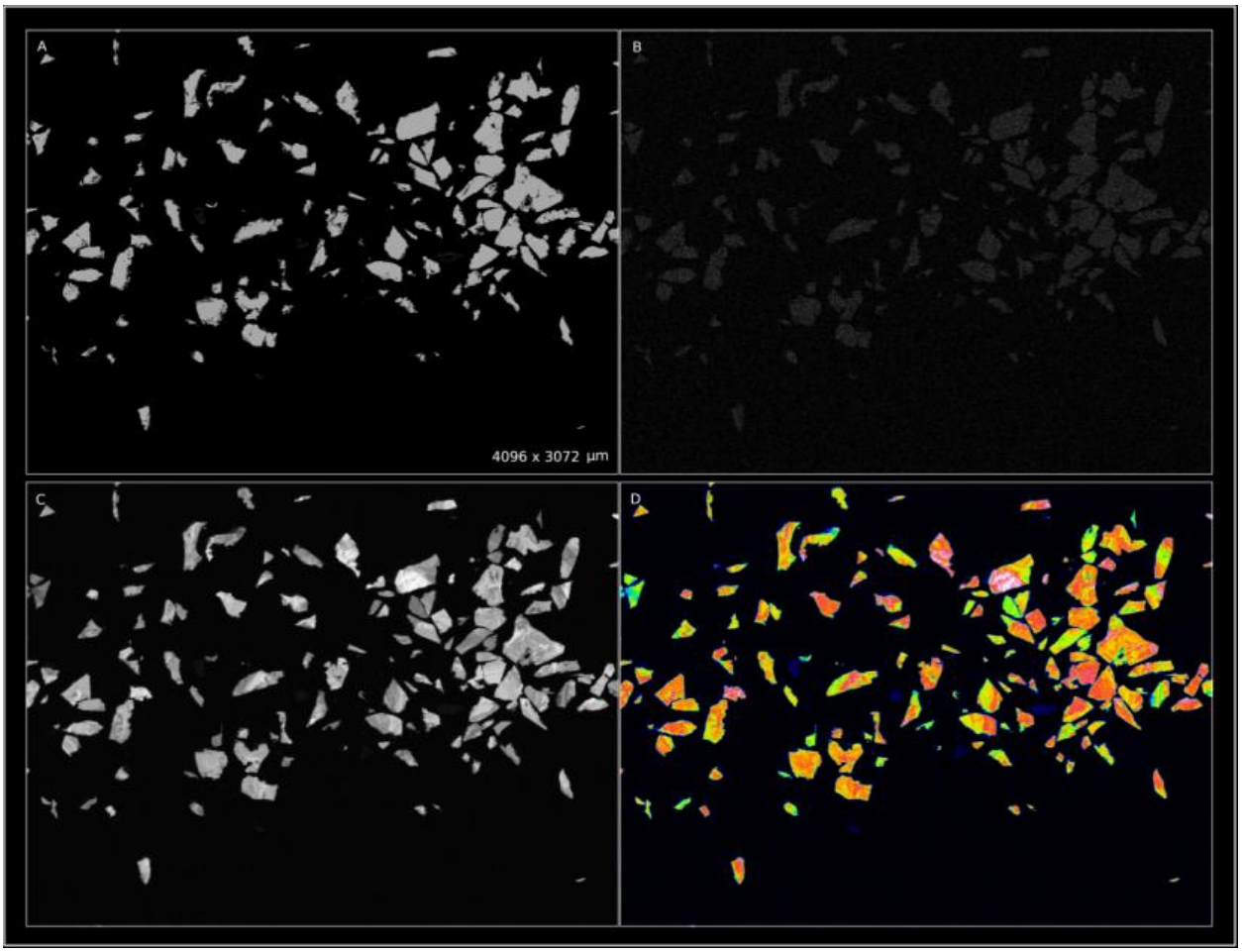

Figure 4.3: EPMA images of Chibuluma West sample NS-137-1336-1-M1.2. **A)** BSE image. **B)** Mo X-Ray image. **C)** Co X-Ray image. **D)** Co X-Ray color enhanced image.

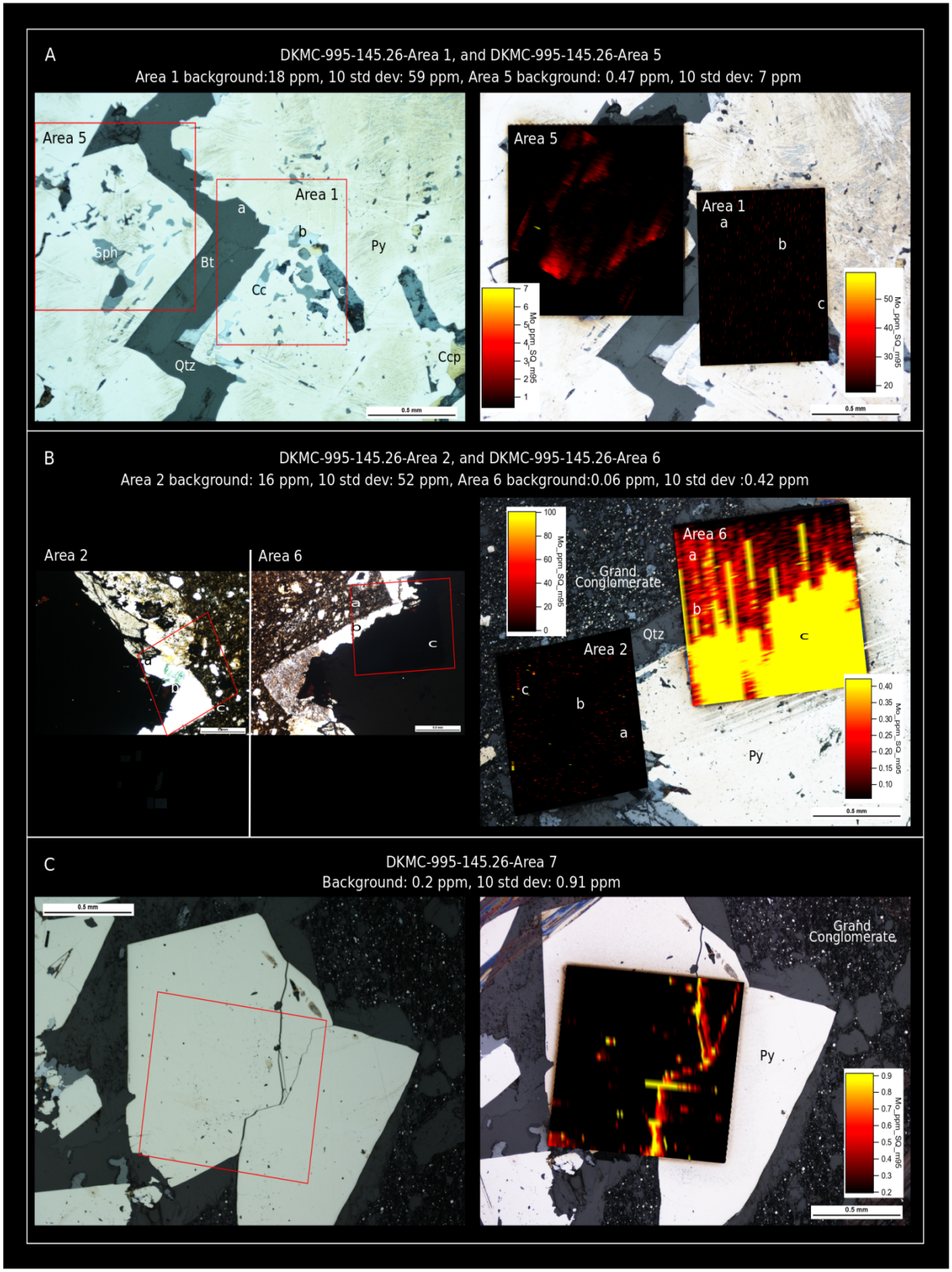
A
DKMC-995-145.26-Area 1, and DKMC-995-145.26-Area 5
Area 1 background:18 ppm, 10 std dev: 59 ppm, Area 5 background: 0.47 ppm, 10 std dev: 7 ppm
Area 5
Area 1
a
b
c
Sph
Bt
Cc
Py
Qtz
Ccp
Mo_ppm_SQ_m95
0.5 mm
B
DKMC-995-145.26-Area 2, and DKMC-995-145.26-Area 6
Area 2 background: 16 ppm, 10 std dev: 52 ppm, Area 6 background:0.06 ppm, 10 std dev :0.42 ppm
Area 2
Area 6
Grand Conglomerate
Qtz
Py
C
DKMC-995-145.26-Area 7
Background: 0.2 ppm, 10 std dev: 0.91 ppm

Figure 4.4: LA Mo mapping of Kamoa thin sections. Images on the left panel are taken under RL, and the ROI is outlined by the box. The cooresponding Mo map is on the right panel. Lowercase letters on both panels serve as reference points. The mimimum values on the color bar located on the right panel are the mean background concentrations for Mo for the given ROI. Therefore non-black pixels are locations where Mo is above background. The maximum value on the color bar is 10 σ above mean background (Potts, 1992). Abbreviations are as follows: biotite (Bt), chalcocite (Cc), chalcopyrite (Ccp), pyrite (Py), sphalerite (Sph), and quartz (Qtz).

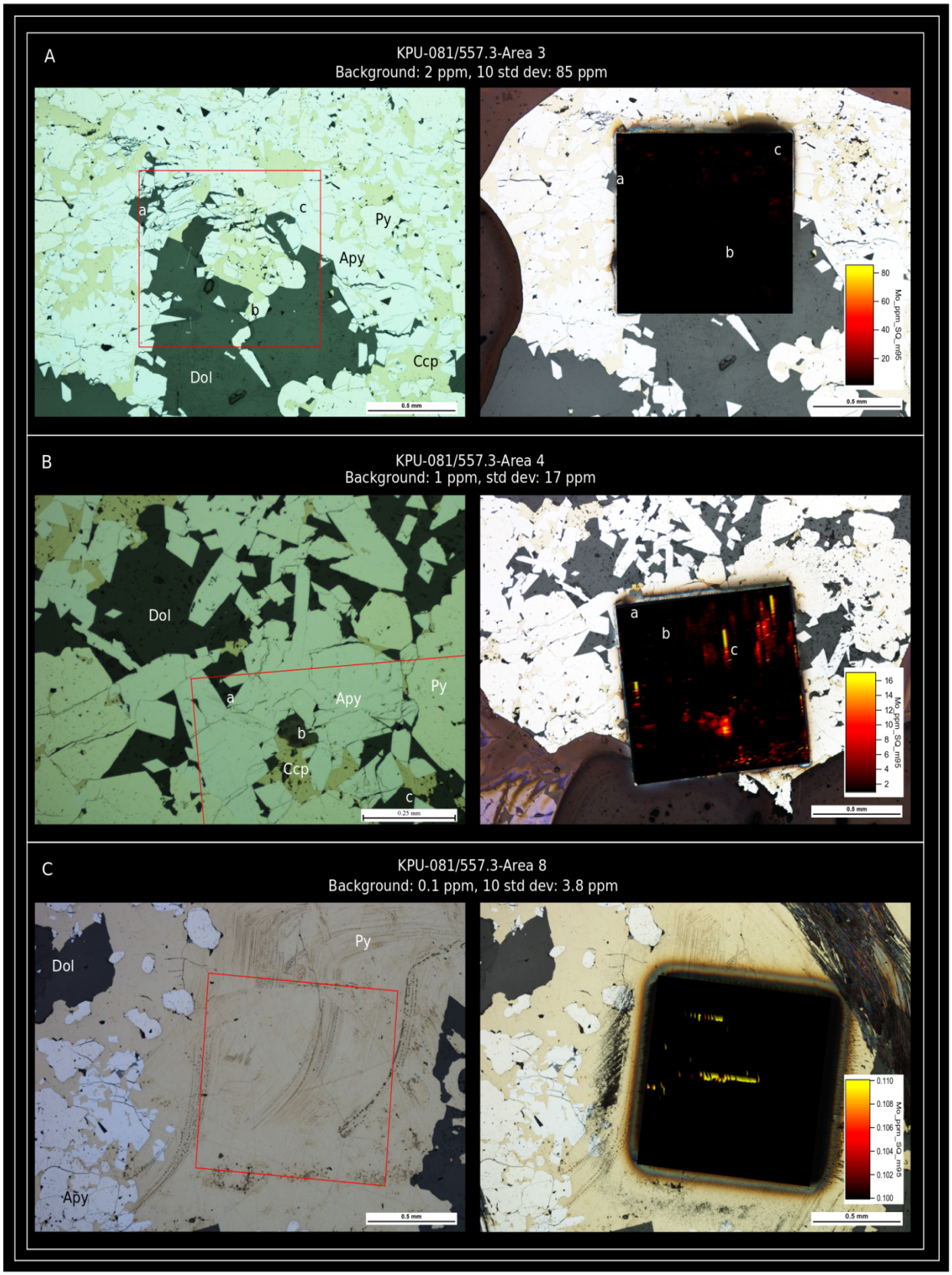
A
KPU-081/557.3-Area 3
Background: 2 ppm, 10 std dev: 85 ppm
a
b
c
Py
Apy
Ccp
Dol
0.5 mm
Mo_ppm_SQ_m95
80
60
40
20
B
KPU-081/557.3-Area 4
Background: 1 ppm, std dev: 17 ppm
Dol
Apy
Py
Ccp
0.25 mm
16
14
12
10
8
6
4
2
C
KPU-081/557.3-Area 8
Background: 0.1 ppm, 10 std dev: 3.8 ppm
Dol
Py
Apy
0.110
0.108
0.106
0.104
0.102
0.100

Figure 4.5: LA Mo mapping of Kipushi thin sections. Images on the left panel are taken under RL, and the ROI is outlined by the box. The cooresponding Mo map is on the right panel. Lowercase letters on both panels serve as reference points. The mimimum values on the color bar located on the right panel are the mean background concentrations for Mo for the given ROI. Therefore non-black pixels are locations where Mo is above background. The maximum value on the color bar is 10 σ above mean background (Potts, 1992). Abbreviations are as follows: arsenopyrite (Apy), chalcopyrite (Ccp), dolomite (Dol), pyrite (Py), sphalerite (Sph), and quartz (Qtz).

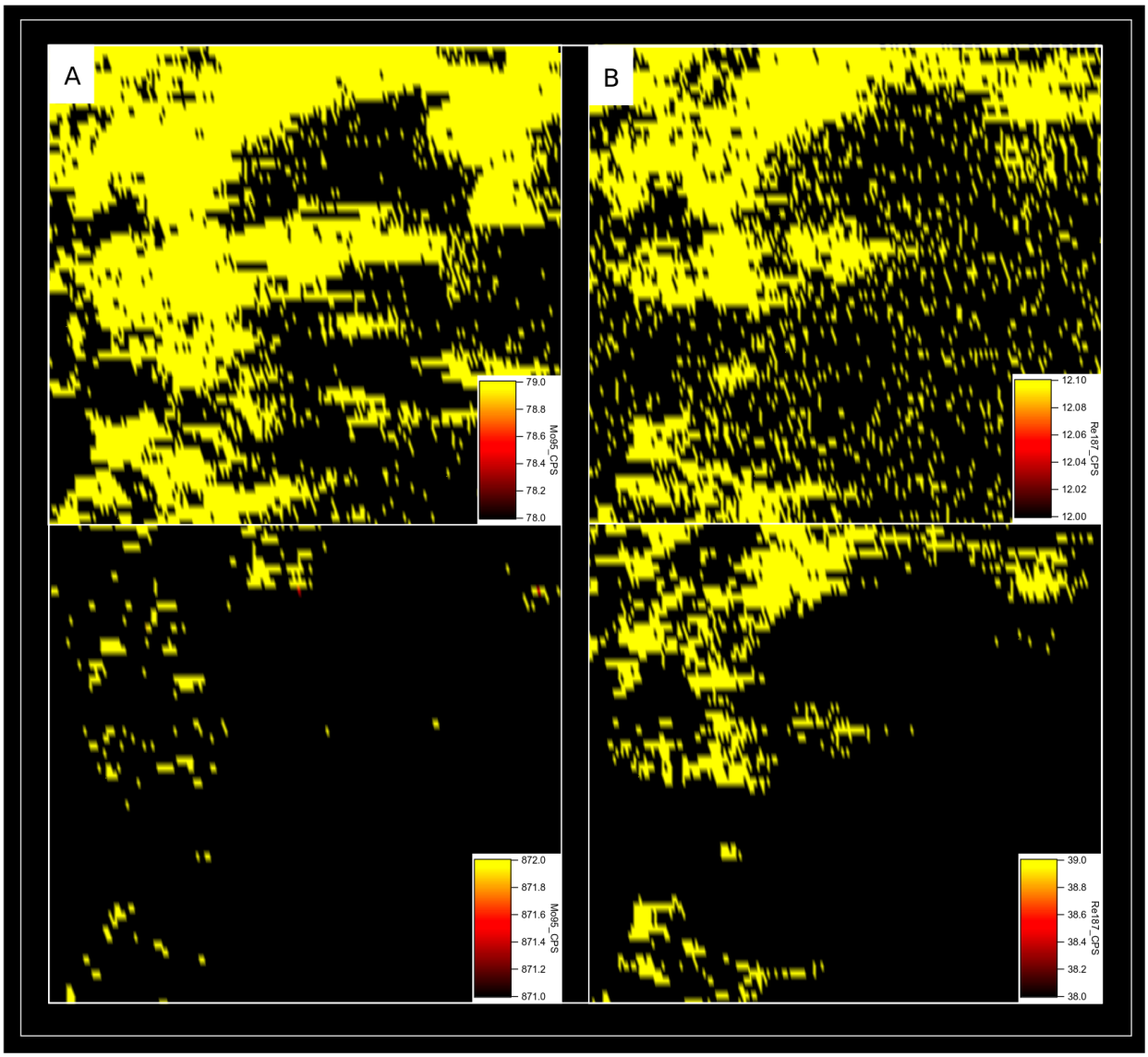

Figure 4.6: LA map of Kipushi thin section KPU-081/557.3 (Area 3 of Figure 4.5) comparing the coorelation between Mo, and Re, FOV is 1 mm^2 **A) Top frame:** The minimum value on the color bar is the mean Mo baseline. **Bottom frame:** The minimum value on the color bar is the summation of the mean Mo baseline and 2σ above the mean baseline. **B) Top frame:** The minimum value on the color bar is the mean Re baseline. **Bottom frame:** The minimum value on the color bar is the summation of the mean Re baseline and 2σ above the mean baseline.

Std deviations + background	% Re:Mo	% Co:Re	% Mo:Co
0	31.17	27.42	33.59
1	19.07	27.84	14.06
2	8.64	23.78	5.30
5	1.14	9.62	0.46
10	0.10	0.00	0.00

Table 4.1: Correlation between trace elements measured via laser ablation in Kipushi thin section KPU-081/557.3. The calculated probability in which both elements coexist in the same cell (Appendix 8.3) as a function of the confidence in measurement.

5) Pb-Pb Geochronology

5.1 Background

5.1.1 Introduction

The benefit of including Pb isotope geochemistry is twofold. Firstly, age data determined through Pb-Pb geochronology serves as a point of comparison to the Re-Os age data (Poty, 1989). Secondly, since the CAC contains significant quantities of Pb (Kampunzu et al., 2009), the Pb ore itself is directly dated. Model lead ages differ from traditional radiogenic isotope ages in that the calculated age is the time in which the sample was removed from a homogenous, bulk reservoir-instead of continuous ingrowth of a daughter isotope. Common lead is extracted from the bulk reservoir at time t and the interval between t_0 and t is the integrated total of produced radiogenic Pb (Figure 5.1). After t, the isotopic composition of the sample is preserved and no more radiogenic Pb is produced. Minerals (ex: pyrite) that do not incorporate U or Th into their crystal structure are the best common lead geochronometers (Köppel and Grünenfelder, 1979). Therefore, unlike Re-Os geochronology, accurate common lead ages depend on the exclusion of parent isotopes and the assumption of comparison to an accurate model evolution.

5.1.2 Calculating Model Lead and Pb-Pb Isochron Ages

There are two different methodological approaches to calculating Pb model ages, although both approaches rely on using the measured $^{206}Pb/^{204}Pb$ sample values. Pb model ages may be calculated using Equation 5.1 or 5.2 as put forth by Stacey and Kramers (1975), and Cumming and Richards (1975), respectively. Stacey and Kramers (1975) Two-Stage model ages rely on a shift in the $^{238}U/^{204}Pb$ (μ) of the bulk Earth from a primordial value of 7.19, to 9.74 at 3.7 Ga. Cumming and Richards (1975) Model III ages differ in that μ-where αVp is equivalent

to μ-increases at some rate (ε). Two-Stage common lead were calculated using Equation 5.1 below from Stacey and Kramers (1975), where

$$x = x_0 + \mu t(e^{\lambda t_0} - e^{\lambda t_1}). \qquad \textit{EQ. 5.1}$$

Due to differences in notation between Stacey and Kramers (1975) and Cumming and Richards (1975), Table 5.2 provides equivalent variables and coefficients for ease of use and brevity. Model III common lead ages were calculated using Equation 5.2 below from Cumming and Richards (1975), where

$$X = a_0 + \alpha V_p \left[e^{\lambda t_0}\left(1 - \varepsilon(t_0 - \tfrac{1}{\lambda}\right) - e^{\lambda t}\left(1 - \varepsilon(t - \tfrac{1}{\lambda}\right)\right]. \qquad \textit{EQ. 5.2}$$

It is clear that Equations 5.1 and 5.2 do not yield the same model lead age. Due to the calculated age discrepancy between both models, evaluation of which model best represents the sample is impossible. However, for model lead ages (not radiogenic leads), Albarede and Juteau (1984) reconciled this problem by standardizing model ages calculated from either Stacey and Kramers (1975) (Equation 5.1) or Cumming and Richards (1975) (Equation 5.2)-allowing both model ages to be plotted together against an accepted Geochron reference line. The Geochron reference line is a regression through a series of accepted common lead ratios. This reference line is extrapolated to the Canyon Diablo Troilite (CDT)-assumed to best represent the primordial bulk Earth. Samples containing an influx of non-common lead indicates open-system behaviour (Albarede and Juteau, 1984), and will yield incorrect common lead ages. As such, samples containing radiogenic lead are referred to as anomalous leads and are frequently encountered in ore systems (Faure and Mensing, 2005). However, given how highly radiogenic these samples, it is probable that some U-rich phase is present. Therefore, the isochron method may be applied to these samples using the $^{207}Pb/^{204}Pb$ and $^{206}Pb/^{204}Pb$ values. Pb-Pb isochrons for the

Chibuluma West samples are provided in Figure 5.3. Isochron ages are referred to as 7/6* ages and are calculated iteratively using Equation 5.3 below,

$$\frac{207}{206}Pb^{*} = \frac{1}{137.88} * \frac{e^{\lambda_{235}t}-1}{e^{\lambda_{238}t}-1}. \qquad EQ.\ 5.3$$

Due to the abundance of radiogenic lead, this approach is similar to a U-Pb age, in that these samples contain high U/Pb and are not good samples for model age Pb analysis. One benefit of this approach lies in the removal of estimating or assuming a μ ($U^{238}/^{204}Pb$) value (Richards et al., 1988b).

5.1.3 Evaluation of Previous Pb-Isotope Geochronology of CAC

A regional, CAC-wide overview of Pb isotope age constraints is provided in Chapter 1.1.3, although the published Pb data and age interpretations are examined herein. Previous workers often do not publish Pb-Pb ages (ex: Walraven and Chabu, 1994; Kamona et al., 1999; Schneider et al., 2007). The ensuing ages in this section and in Chapter 5.1.4 are Cumming and Richards (1975) Model III ages, unless otherwise noted., the method chosen to calculate a model Pb age is sensitive to assumptions made about a set of samples. In particular, the assumed $^{238}U/^{204}Pb$ (μ) value may affect the calculated model age. The viability of a chosen μ value is critiqued in detail in Chapter 5.4.3.

The 680 ± 13 Ma Pb model age for Kabwe as reported by Kamona et al. (1999) is suspicious because when the reported sample $^{206}Pb/^{204}Pb$ isotopes are used, Stacey and Kramers (1975) Two-Stage model Pb ages (using μ = 9.74 at 3.7 Ga), range from 467 to 444 Ma. In addition, these authors propose a μ of 10.31 to substitute for 9.74 at 3.7 Ga, which still does not return 680 Ma ages. Furthermore, there are no 3.7 Ga basement rocks underlying the Katangan Supergroup. 680 Ma Pb model ages are possible for a Three-Stage evolution, if the third stage

began at 2.0 Ga, and if the corresponding μ = 27, although none of these parameters are mentioned by Kamona et al. (1999). Finally, Cumming and Richards Model III Pb ages of the same Kabwe data set of Kamona et al. (1999) return Model Pb ages ranging from 477 to 498 Ma. This is corroborated by the Albarede and Juteau (1984) age estimates in Figure 5.2-where a post-Lufilian timing is obtained, not a pre-Lufilian timing as suggested by Kamona et al. (1999).

The 645 ± 15 Ma Pb-Pb isochron age from chalcopyrite dominant samples from Musoshi as reported by Richards et al. (1988a) are interpreted as age minima for stratiform mineralization. These workers also measured Pb isotopes in feldspars from the same deposit, which, upon plotting in Figure 5.2 display a wide range of ages. These feldspars return approximate ages ranging from ~440 to ~710 Ma. The upper end of these feldspars is significantly older than the 645 Ma ore sulphide age, whereas the majority of the feldspars plot near 575 Ma or younger. In summary, these feldspars were interpreted by Richards et al. (1988a) to be isotopically mixed with the 645 Ma stratiform ore Pb, and Pb from a younger 514 Ma remobilization event. However, this explanation does not account for the ~440 Ma feldspars, which are younger than the proposed 514 Ma endmember necessary for mixing, and the ~710 Ma feldspar is older than the 645 Ma stratiform Pb ore age. Instead, the 645 Ma stratiform ore timing may include exotic Pb, sourced from preexisting phases in the Ore Shale host rock. This exotic Pb is likely the cause for the ~710 Ma feldspar, and the actual timing of ore mineralization at Musoshi is likely more similar to the ~575 Ma age as per the majority of the feldspars which precipitated alongside the stratiform ore.

5.1.4 Kipushi Deposit

Kipushi sphalerite data from Walraven and Chabu (1994) yields model Pb ages of 487 and 496 Ma, while a suite of galena samples yielded Pb model ages ranging from 481 to 355 Ma.

Later work from Kipushi conducted by Kamona et al. (1999), yield galena Pb-model ages ranging from 476 to 424 Ma. These ages are in agreement with these authors' published Pb age of 456 Ma, μ of 9.84. Pb model ages from the published bornite, renierite, and sphalerite samples of Schneider et al. (2007) range from 437 to 489 Ma, with a mean age of 470 Ma (n = 9), and a μ of 9.82. The sphalerite samples from Schneider et al. (2007) received a leaching procedure prior to digestion. This implies that the measured Pb ratios are in isotopic homogeneity with the ore fluid (no post-ore rim).

Together, these Pb ages reflect a post-Lufilian timing, although the ~355 Ma model ages from the Walraven and Chabu (1994) data in particular are much younger than the expected ~450 Ma ore emplacement suggested by Schneider et al. (2007) and Walraven and Chabu (1994). If these ages are real, it may indicate a previously unexamined mineralization event.

5.2 Methodology

5.2.1 Chemical Separation

Between 5 to 25 mg aliquots from the mineral separate vial (as explained in Chapter 3.2) used for Re-Os analysis was used for common lead isotopic analysis. Once weighed, the unspiked samples were treated with a leaching procedure similar to that of Schneider et al. (2007), wherein dilute (0.2 N) HCl was added to the solid sample for 2 hours. This leaching procedure was used to remove the outer surface of the sulphide grains, and therefore any non-primary Pb signal. The leachate solution was isolated from the undissolved sulphide and was dried. The remaining undissolved sulphide was digested in aqua regia for 24 hours at 80°C, and subsequently dried. Dried samples were equilibrated in 0.5N HBr (Manton, 1988) and filtered at 0.45 μm to remove insoluble particles (silicates). This solution was loaded into chromatography columns containing Dowex AGI-8X resin. Procedural total Pb mean blank values (n = 4) are

0.84 ng (ppb). This value is well below the 2 ng threshold for acceptable blanks, given samples with ~1 μg Pb (Dickin, 1995).

5.2.2 Mass Spectrometry

All Pb measurements were made using a Nu Instruments Nu Plasma inductively coupled plasma multicollector mass spectrometer (ICP-MC-MS) in the CCIM at the University of Alberta. Four lead isotopes were measured (^{204}Pb, ^{206}Pb, ^{207}Pb, and ^{208}Pb) with normalization to ^{204}Pb. The accepted TIMS Pb values for the external standard NBS 981 served as a reference ratio. The measured absolute difference of the measured isotopic value from the accepted value is 1.19%, 0.17%, 0.34 %, and 0.03 % for ^{208}Pb/^{204}Pb, ^{207}Pb/^{204}Pb, ^{206}Pb/^{204}Pb, and ^{207}Pb/^{206}Pb respectably. NBS 981 was measured least twice for each analytical session. Instrumental mass bias was corrected by Tl doping with a solution of known ^{205}Tl/^{203}Tl. Thallium is used as it is of similar mass to the Pb isotopes of interest, and mass bias effect (and Pb/Pb correction) for both are be modelled using a power law relationship (Begley and Sharp, 1997).

5.3 Results

Pb isotope data is presented in Table 5.1 for the Chibuluma West, Kamoa, and Kipushi deposits. The data has been corrected for mass bias (see Tl doping in 5.2.2) and normalized to NBS 981; all errors are to 2 σ. Common lead model ages are not calculable for the Chibuluma West samples due to highly radiogenic Pb isotope compositions, although 7/6* ages are calculated using Equation 5.3. Measured Pb isotope data, and the calculated Pb model ages following Stacey and Kramers (1975) and Cumming and Richards (1975) are provided in Table 5.1. Model Pb ages for both Kamoa and Kipushi samples are independently compared to the Albarede and Juteau (1984) Geochron reference line in Figure 5.2, allowing for a third age to be

determined. Published Pb isotopes from other CAC deposits are also included in Figure 5.2 for comparision.

5.3.1 Kamoa

For model ages calculated using Equation 5.1, a range from 490 Ma to 475 Ma is returned for the digested pyrite, while leached pyrite returned a range from 486 Ma to 475 Ma. Similarly, for model ages calculated using Equation 5.2, a range from 519 Ma to 505 Ma is returned for the digested pyrite, while leached pyrite returned a range from 517 Ma to 507 Ma.

The Kamoa digested pyrite samples plot slightly above the Two-Stage growth line of Stacey and Kramers (1975) (Figure 5.4A). In the Albarede and Juteau (1984) model, only $^{206}Pb/^{204}Pb$ are used, and sample ages are determined when compared to accepted, conformable ores of known age The Kamoa pyrite samples support both the Stacey and Kramers (1975), and the Cumming and Richards (1975) model ages, as these pyrites return Albarede and Juteau (1984) ages of ~500 Ma (Figure 5.2).

5.3.2 Kipushi

Unlike Kamoa, Pb isotopes from Kipushi are noticeably varied and are leach/residue dependent. The mean residue sample (arsenopyrite, chalcopyrite, gangue, and pyrite) model ages are at least 89 Myr (from Equation 5.2) older than the leachate mean of the same samples. All leachate sample model ages are between 360 Ma and 317 Ma, broadly similar to the range in Re-Os ages observed in Chapter 3. Mean residue arsenopyrite, chalcopyrite, gangue, and pyrite model lead ages calculated using Equation 5.2 are 387 Ma, 389 Ma, 488 Ma, and 478 Ma respectively.

These samples yield Albarede and Juteau (1984) ages (Figure 5.2) that are in agreement with both Stacey and Kramers (1975) and Cumming and Richards (1975) Pb model ages. For

example, in Figure 5.2, the Pb ages range from ~470 to ~325 Ma which is very similar to the range of calculated Pb model ages, as the upper end age 488 Ma (Equation 5.2) and the lower end age of 317 Ma (Equation 5.1).

5.3.3 Chibuluma West

Despite the inability to calculate common lead ages, the isochron method was applied to a suite of mineral separates. The isochrons and the corresponding 7/6* age results as determined from Equation 5.3 are provided in Figure 5.3. Similar to the leach vs residue samples from Kipushi, the Chibuluma West leach/residue Pb ratios vary significantly, and given the complexity of the Chibuluma West samples, the isochrons in Figure 5.3 are arranged as follows:

- Figure 5.3A: MI-Heavy + Pyrite mineral separates. These samples are combined as they both are sulphide-rich. The MI-Heavy samples have not been magnetically separated, and would contain magnetic phases, that the more pure pyrite mineral separate would not. Any grain with a bulk density greater than of 3.32 g/cm^3 (Chapter 3.2.1) may be included in this fraction. The Pb-Pb isochron age of these four samples is 568 ± 250 Ma, MSWD = 33. This very high age uncertainty may reflect the relative impurity of the MI-Heavy, as dense detrital grains such as in the host rock would be present in this mineral separate, and would have no association with ore mineralization. In particular, zircon is found in the host rocks at Chibuluma West by Selley and Cooke (2001). Ages associated with detrital phases would predate ore formation and skew the data-resulting in high age uncertainties.
- Figure 5.3B: Pyrite mineral separate. This two-point regression provides a better age constaint to the ore mineralization at Chbuluma West than the regression in Figure 5.3A, as only ore-stage pyrite is included. The age of this regression is 552 ± 58 Ma. An

MSWD is not calculable for two-point regressions as the formula to calculate the MSWD contains (n-2) in the denominatior (Kullerud, 1991).

- Figure 5.3C: MI-Light mineral separate + pyrite and MI-Heavy leachate: These samples were combined as they would represent phases precipitated from the ore fluid, or from a post-ore event. In other words, they are gangue samples, and the six point isochron yields a Pb-Pb age of 667 ± 26 Ma, MSWD = 78. These samples produce a noticeably older age than the previous two regressions. The samples in this isochron likely are a mixing of ore-stage gangue with detrital phases (ex: feldspars, see Chapter 5.1.2) that predate the ore mineralization.

The considerable amount of radiogenic Pb in the Chibuluma West samples can be visualized as in Figure 5.4B. The Chibuluma West digested pyrite and MI-light samples plot far off the Stacey and Kramers (1975) Two-Stage reference line. Since these samples plot ahead of the 0 Ma reference point, any model age would return future ages. In addition, due to the radiogenic Pb, none of the Chibuluma West samples plot close to the Albarede and Juteau (1984) reference line.

5.4 Discussion

5.4.1 Age Constraints for Kamoa

Lead isotopes and the calculated common lead ages for the Kamoa deposit are unimodal and well constrained. The model ages clearly support a Lufilian to post-Lufilian timing from 519 to 475 Ma. In either case, the Pb model ages are not compatible with a diagenetic age, and are independently confirmed by the Albarede and Juteau (1984) plot in Figure 5.2. The lack of variance in these model ages indicates that a single fluid was responsible for ore mineralization, also suggested by Schmandt et al. (2013). Furthermore, there is no difference between either the

residue (digested) pyrite Pb model ages, or the leachate pyrite Pb model ages. Therefore, it appears the Pb isotopes have not been affected by the same process(es) that yield a wide range in Re-Os model ages from 481 to 258 Ma.

The regression line of all Kamoa pyrites (Figure 5.4A), intersects the Stacey and Kramers (1975) reference line at 731 Ma. While the coorelation coefficient of this regression is poor ($r^2 \approx 0.46$), the Kamoa pyrites nonetheless contain radiogenic lead not associated with the primary ore deposition ca 500 Ma. Depending on which pyrite samples are chosen for regression, the time ranges to a minimum of 646 Ma, an age obtained for the two pyrite samples with the greatest spread in Re/Os and Os/Os space. In either case, radiogenic Pb (enriched in ^{207}Pb) was removed from a U-rich source between ~731 to ~646 Ma. The intersection occurring at ~731 Ma is reasonable because the contact between the Grand Conglomerate and the underlying Mwashya Formation has been directly dated at 727 ± 4.9 Ma (Rooney et al., 2015), making it within error of the start of the deposition of the Grand Conglomerate. The Grand Conglomerate is well established as a glacial till, deposited by the Sturtian glaciation event in the Neoproterozoic (~730-660 Ma) Rooney et al., (2015). The lower age constraint of ~646 Ma is similar in time to the end of the Sturtian glaciation. The Sturtian ice sheet must have scoured the U-rich reservoir (gneiss and schist basement) and accumulated lithic fragments in the glacial till. Batumike et al. (2007) and Schmandt et al (2013) have observed both gneiss and schist lithic clasts in the diamictite of the Grand Conglomerate. Preenrichment of the Grand Conglomerate offers a solution to the radiogenic lead component in the Kamoa pyrites. The source of the radiogenic lead is likely from the 2.0 Ga basement. Sillitoe et al. (2015) report a copper preenrichment event ca 1100 Ma for the Nyungu deposit in Zambia, and attribute a 2.0 to 1.9 Ga basement source. Unfortunately, the radiogenic Pb component from Kamoa cannot be explained by an

increase in μ (discussed in Chapter 5.4.4), or by a three-stage Pb evolution using either 2.0 Ga or 1.1 Ga as t_0. It is probable, that radiogenic Pb from exotic/detrital minerals in the CAC is the cause for apparent diagenetic Pb model (Kabwe: Kamona et al., 1999) and Pb-Pb isochron ages (Musoshi: Richards et al., 1988a).

5.4.2 Age Constraints for Kipushi

The model Pb ages for the Kipushi samples support two events. The initial event occurred ~410 Ma (mean Two-Stage Stacey and Kramers (1975) model Pb ages are 390 Ma, while mean Model III Cumming and Richards (1975) model Pb ages are 428 Ma). Individual sample model Pb ages are similar to the ~450 Ma Re-Os and Rb-Sr isochron ages of (Schneider et al., 2007), and to the 456 Ma Pb ages of Kamona et al. (1999). This timing is likely related to a syenite intrusion also occurring ca 450 Ma (Cosi, et al., 1992; Walraven and Chabu, 1994; Kamona et al., 1999; John et al., 2004; Schneider et al., 2007). It appears that this post-Lufilian timing is not unique to the Kipushi deposit, as Figure 5.2 clearly shows $^{206}Pb/^{204}Pb$ ratios from Kabwe, Lombe, Musoshi, and Tsumeb yield overlapping ages with Kipushi-all post-dating the Lufilian Orogeny.

The second event at Kipushi is supported by Pb model ages ranging from 294 to 338 Ma taken from the leachate samples. This second event is strikingly similar in age to the Re-Os isochron ages for both Kamoa (282 Ma) and Kipushi (290 Ma and 327 Ma). This revelation indicates a regional event during the Late Paleozoic, and may be linked to the collision event discussed in Chapter 3.4 (Daly et al., 1992).

5.4.3 Age constaints for Chibuluma West

A significant contribution of radiogenic lead is found in all of the Chibuluma West samples. The 667 ± 26 Ma isochron age obtained from the gangue samples is likely the result of

radiogenic Pb from silicate or carbonate phases that incorporated Pb into their crystallographic matrix prior during sedimentation of the Chibuluma West host rocks or prior to deposition of the host rock. The MI-Heavy + pyrite isochron age of 568 ± 250 Ma is likely caused by an impure mineral separate, as the MI-Heavy fraction was not magnetically separated. The MI-Heavy fraction contains radiogenic lead as well-a mixing of Pb from detrital grains. Examples of dense, U-rich minerals found in the Chibuluma West host rock includes (recrystallized) rutile, and zircon (Selley and Cooke, 2001). Finally, the ore-stage pyrite itself contains radiogenic Pb. The source of this Pb may be from inclusions of U-rich phases such as rutile or uraninite-both have been found to be coeval with vein-hosted ore mineralization at Musoshi (Richards et al., 1988a; Richards et al., 1988b).

In summary, detrital grains present in the Chibuluma West host rock contribute to the excess radiogenic Pb in both the MI-Heavy, and gangue (MI-Light + leachate) samples. Unless this radiogenic Pb is accounted for, a diagenetic/pre-Lufilian timing is obtained. This revelation may also explain the pre-Lufilian ~645 Ma Pb-Pb isochron for the Musoshi deposit (Richards et al., 1988a).

5.4.4 Mu and Pb Origin

The μ value is a useful indicator of Pb provenance. This is because of the fractionation of U (and thus radiogenic Pb) into the crust (similar to Re) with respect to the mantle. Pb isotopes take on signatures which reflect the reservoir from which they were derived. This concept, developed by Zartman and Doe (1981) is referred to as plumbotectonics and can assist in determining the source of Pb. Figure 5.6 displays a series of Pb isotopes from deposits throughout the CAC as well as Pb isotope data from the Kamoa and Kipushi deposits from this study. The plumbotectonics reservoirs are included and their evolution of time is included.

Under a Two-Stage model, the average μ of the homogenous Pb reservoir increased to 9.74 at 3.7 Ga (Stacey and Kramers, 1975). The μ values for samples from this study are presented in Table 5.1 and were calculated using Equation 5.4 after Faure and Mensing (2005),

$$\mu = \frac{x - x_0}{e^{\lambda t_0} - e^{\lambda t}}. \qquad \textit{EQ. 5.4}$$

Notation used is that of Stacey and Kramers (1975) Table 5.2. It should be noted that the time used was from the Cumming and Richards (1975) Model III age. Determination of μ using Stacey and Kramers (1975) model ages would be inappropriate, as those ages rely on assuming a μ value-an assumption not made by Cumming and Richards (1975) (as μ is constantly increasing over time). This effect is visualized in Figure 5.5, where an increase in μ produces a profound increase in the Stacey and Kramers (1975) growth lines. The Pb isotopes of nearly all deposits provided in Figure 5.5 support an elevated μ (greater than 9.74).

Given the unimodal nature of the model Pb ages for Kamoa pyrite, the μ values are similarly homogenous. A mean value of 9.81 is calculated for both pyrite and leachate samples. When the Kamoa pyrite and leachate are plotted in Figure 5.5, the μ is close to 10.50. However, this elevated value is the result of excess radiogenic ^{207}Pb. While the Kamoa pyrites appear to plot near the 750 Ma isopleth in Figure 5.5, this age cannot be accepted as it is in direct discord with the calculated μ, and the Pb-model ages. Furthermore, this time is impossible as it exceeds the known age of the base of the Grand Conglomerate host rock (Rooney et al., 2015). Instead, while these Pb ratios cannot be reconciled with either an elevated μ, or by a Three-Stage Stacey and Kramers (1975) evolution (as mentioned in Chapter 5.4.1), they are clearly of a crustal origin (Figure 5.6). If an isopleth is held constant at ~500 Ma as suggested by the model ages, the resulting Kamoa samples plot between the orogene and upper crust reservoirs. Perhaps the lithic clasts in the Grand Conglomerate are indeed the source of the radiogenic Pb in the Kamoa

pyrites, and the cause of the apparent 750 Ma age in Figure 5.5, and the location above the crustal endmember in Figure 5.6.

A mean value of 9.82 is returned for the Kipushi digested samples, while a slightly higher mean value of 9.84 is returned for the leachate samples. The calculated μ values from both digested and leachate Kipushi samples are within error of the galena (μ = 9.79 ± 0.12) and the bulk sulphide (bornite, chalcopyrite, galena, and sphalerite, μ = 9.88 ± 0.05) (Walraven and Chabu, 1994). These authors suggest a crustal source, but do not exclude possible magmatic influence. Conversely, Kamona et al. (1999) assign a significant mantle contribution to Kipushi sulphide (μ = 9.84). The published Pb isotopic data agrees well with the results from this study, as the samples plot in close proximity (Figure 5.5). The leachate samples from this study do indeed corroborate a younger timing, and a slightly elevated μ. There is no evidence for a mantle source based on the Plumbotectonics model for the Kipushi deposit (Figure 5.6).

The plumbotectonics plot in Figure 5.6 indicates that several deposits (Tsumeb, Kabwe, Musoshi, Kinsenda, and Kolwezi) contain excess ^{207}Pb-indicative of radiogenic Pb. If the same technique applied to the Kamoa samples is applied to these deposits' samples, an orogenic or upper crustal lead source is suggested.

5.5 Conclusion

The Chibuluma West pyrite isochron age of 552 ± 58 Ma is within error of the Re-Os pyrite isochron age, and is of Lufilian timing. Significant radiogenic Pb is found throughout the Chibuluma West samples, but most particularly in the MI-light and leachate samples. This radiogenic Pb is derived from silicates or carbonates predating the actual ore mineralization in the Lufilian, or from impure mineral separates, while the radiogenic Pb in the pyrite is possibly from rutile or uraninite inclusions. Radiogenic Pb must be considered or pre-Lufilian, diagenetic

ages may result. This revelation likely explains the apparent diagenetic ages obtained from other workers (ex: Kabwe, Musoshi).

The Kamoa model Pb ages are unimodal, and also support a Lufilian timing (~512 Ma) for ore formation. The Grand Conglomerate likely experienced a preenrichment event during the Sturtian glacation-although precise time constraints are difficult to determine. This preenrichment event may further help explain previous diagenetic interpretations as well as the radiogenic Pb input from basement sources. Hydrothermal mineralization at Kamoa must have occurred in a single pulse of fluid as there is no difference between digested pyrite and leached pyrite Pb ages. The Pb in the stratiform ore was derived from the crust.

Kipushi model Pb ages indicate two pulses of fluid. The original mineralization event occurred after the Lufilian orogeny, ~428 Ma. Most striking is the similarity between the Kipushi leachate model Pb ages and the Re-Os isochron ages for both Kamoa and Kipushi. The overlapping of these two geochronometers supports the existence of a Late Paleozoic fluid containing both Mo (and Re) and Pb. These revelations indicate a large-scale Mo and Pb-rich fluid precipitating molybdenite in fractures, and Pb adsorbed to sulphide rims after the Lufilian orogeny ended. It is unlikely that this fluid reached deeper sediments in the Katangan Basin (Lower Roan), given the high Re-Os precision obtained from Chibuluma West. Instead, this Mo-rich fluid traversed throughout the Nguba Group and interacted with reactivated faults, precipitating Mo in crosscutting fractures of the Kamoa and Kipushi ore-stage sulphides.

5.6 References

Albarede, F., and Juteau, M., 1984, Unscrambling the lead model ages, Geochimica et Cosmochimica Acta, v. 48, p. 207-212

Batumike, M.J., Cailteux, J.L.H., Kampunzu, A.B., 2007, Lithostratigraphy, basin development, base metal deposits, and regional correlations of the Neoproterozoic Nguba and

Kundelungu rock successions, central African Copperbelt, Gondwana Research, v. 11, p. 432-447

Begley, I.S., and Sharp, B.L., 1997, Characterization and correction of instrumental bias in inductively coupled plasma quadrupole mass spectrometry for accurate measurement of lead isotope ratios, Journal of Analytical Atomic Spectrometry, v. 12, p. 395-402

Cumming, G.L., and Richards, J.R., 1975, Ore lead isotope ratios in a continuously changing Earth, Earth and Planetary Science Letters, v. 28, p. 155-171

Daly, M.C., Lawrence, S.R., Diemu-Tshiband, K., and Matouana, B., 1992, Tectonic evolution of the Cuvette Centrale, Zaire, Journal of the Geological Society, London, v. 149, p. 539-546

Dickin, A.P., 1995, Radiogenic Isotope Geology, Cambridge University Press, Cambridge, UK

Faure, G., and Mensing, T.M., 2005, Isotopes: Principles and Applications, Wiley, Hoboken, USA

Frimmel, H.E., Jonasson, I.R., and Mubita, P., 2004, An Eburnean base metal source for sediment-hosted zinc-lead deposits in Neoproterozoic units of Namibia: Lead isotopic and geochemical evidence, Mineralium Deposita, v. 39, p. 328-343

Jaffey, A.H., Flynn, K.F., Glendenin, L.E., Bentley, W.C., and Essling, A.N., 1971, Precision measurement of half-lives and specific activities of ^{235}U and ^{238}U, Physical Review C, v. 4, p. 1889-1906

Kamona, A.F., Lévêque, J., Friedrich, G., and Haack, U., 1999, Lead isotopes of the carbonate-hosted Kabwe, Tsumeb, and Kipushi Pb-Zn-Cu sulfide deposits in relation to Pan African orogenesis in the Damaran-Lufilian fold belt of Central Africa, Mineralium Deposita, v. 34, p. 273-283

Kampunzu, A.B., and Cailteux, J., 1999, Tectonic evolution of the Lufilian Arc (Central Africa Copper Belt) during Neoproterozoic Pan African orogenesis, Gondwana Research, v. 2, p. 401-421

Köppel, V., and Grünenfelder, M., 1979, Isotope geochemistry of lead, *In:* Jäger, E., and Hunziker, J.C. (Eds), Lectures in Isotope Geology, Springer, Berlin, Germany

Kullerud, L., 1991, On the calculation of isochrons, Chemical Geology, v. 87, p. 115-124

LeRoux, L.J., and Glendenin, L.E., 1963, Half-life of thorium-232, Proc. Natl. Conf. on Nuclear Energy, Pretoria, p. 83-94

Ludwig, K.R., 2003, Isoplot/Ex version 3.76, A geochronological toolkit for Microsoft Excel, Berkeley Geochron Canter Special Publication, v. 4, p. 1-43

Manton, W.I., 1988, Separation of Pb from young zircons by single-bead ion exchange, Chemical Geology, v. 73, p. 147-152

Porada, H., and Berhorst, V., 2000, Towards a new understanding of the Neoproterozoic-Early Palæzoic Lufilian and northern Zambezi Belts in Zambia and the Democratic Republic of the Congo, Journal of African Earth Sciences, v. 30, n. 3, p. 727-771

Poty B., 1989, Geological conditions governing the use of dating methods, *In:* Roth, E., Poty, B., and Menager, M.T. (Eds), Nuclear Methods of Dating, Kluwer Academic Publishers, Dordrecht, Netherlands

Richards, J.P., Cumming, G.L., Krstic, D., Wagner, P.A., and Spooner, E.T.C., 1988a, Pb isotope constraints on the age of sulfide ore deposition and U-Pb age of late uraninite veining at the Musoshi stratiform copper deposit, Central African Copper Belt, Zaire, Economic Geology, v. 83, p. 724-741

Richards, J.P., Krogh, T.E., and Spooner, E.T.C., 1988b, Fluid inclusion characteristics and U-PB rutile age of late hydrothermal alteration and veining at the Musoshi stratiform copper deposit, Central African Copper Belt, Zaire, Economic Geology, v. 83, p. 118-139

Richards, J.P., and Noble, S.R., 1998, Application of radiogenic isotope systems to the timing and origin of hydrothermal processes, *In:* Richards, J.P., and Larson, J.B., (Eds), Techniques in Hydrothermal Ore Deposits Geology, Reviews in Economic Geology, v. 10, Society of Economic Geologists, Littleton, USA

Rooney, A.D., Strauss, J.V., Brandon, A.D., and Macdonald, F.A., 2015, A Cryogenian chronology: Two long-lasting synchronous Neoproterozoic glaciations, v. 43, p. 459-462

Schneider, J., Melcher, F., and Brauns, M., 2007, Concordant ages for the giant Kipushi base metal deposit (DR Congo) from direct Rb-Sr and Re-Os dating of sulfides, Mineralium Deposita, v. 42, p. 791-797

Selley, D., and Cooke, D., 2001, Mineral zonation and sulfur isotope systematics of the Chibuluma West copper-cobalt deposit, Zambia, AMIRA P544 Progress Report, December, p. 133-169

Stacey, J.C., and Kramers, J.D., 1975, Approximation of terrestrial lead isotope evolution by a two-stage model, Earth and Planetary Science Letters, v. 26, p. 207-221

Tatsumoto, M., Knight, R.J., Allégre, C.J., 1973, Time differences in the formation of meteorites as determined from the ratio of lead-207 to lead-206, Science, v. 180, p. 1279-1283

Walraven, F., and Chabu, M., 1994, Pb-isotope constraints on base-metal mineralisation at Kipushi (Southeastern Zaïre), Journal of African Earth Sciences, v. 18, p. 73-82

Zartman, R.E., and Doe, B.R., 1981, Plumbotectonics, the model, Tectonophysics, v. 75, p. 135-162

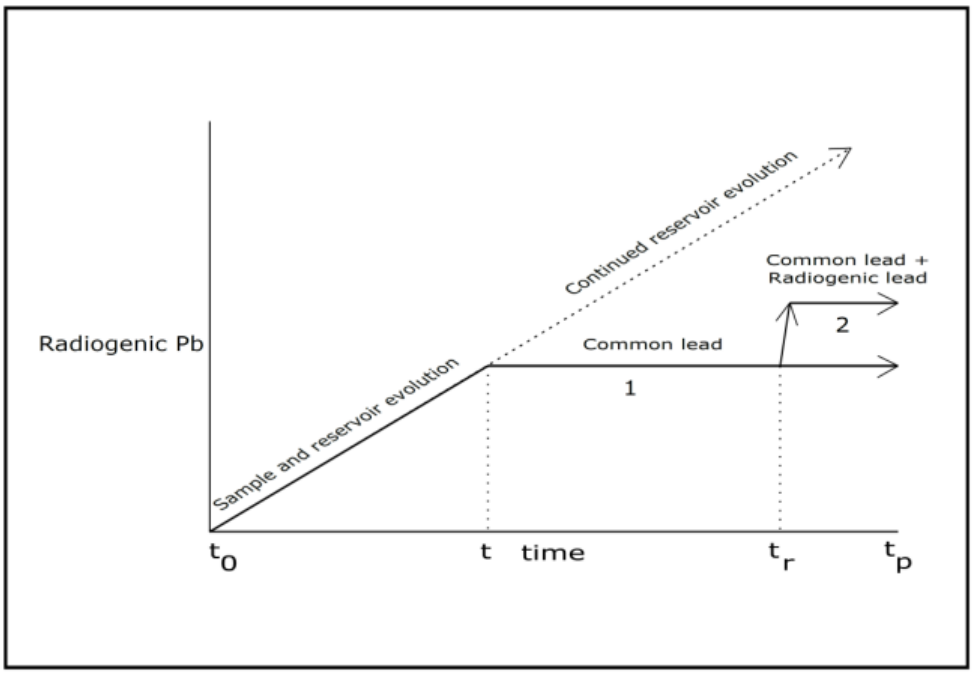

Figure 5.1: Common lead evolution curve from the primordial Earth at t_0 to the present t_p. Radiogenic lead is produced from a uranium source and is resulting Pb-Pb isotopic compostion of both the reservoir and rock are recorded. At some time t, the measured sample is extracted from this bulk reservoir and the Pb-Pb isotpic composition of the sample is retained forever (assuming no isotopic reequilibration or mixing). The true age of the sample is representated by the Pb-Pb ratio at t. A common lead age is the integrated total of radiogenic lead produced prior to reservoir extraction from t_0 to t (Path 1). If an influx of radiogenic Pb at t_r occurs (Path 2), the Pb-Pb ratio, and the geochronological age will be apparent, and not true.

Full Name	Sample Name	Deposit	Dominant Phase
DKMC-995-145.26-TS2	TS2	Kamoa	Pyrite
DKMC-995-145.26-Cube2M	Cube2M	Kamoa	Pyrite
DKMC-995-145.26-Cube2NM	Cube2NM	Kamoa	Pyrite
DKMC-995-145.26-WF1M	WF1M	Kamoa	Pyrite
DKMC-995-145.26-WF2M	WF2M	Kamoa	Pyrite
DKMC-995-145.26-WF3M	WF3M	Kamoa	Pyrite
DKMC-995-145.26-WF4M	WF4M	Kamoa	Pyrite
DKMC-995-145.26-WF5NM	WF5NM	Kamoa	Pyrite
DKMC-995-145.26-WF6NM	WF6NM	Kamoa	Pyrite
DKMC-995-145.26-Cube2M-L	Cube2M-L	Kamoa	Pyrite-Leach
DKMC-995-145.26-Cube2NM-L	Cube2NM-L	Kamoa	Pyrite-Leach
DKMC-995-145.26-TS2-L	TS2-L	Kamoa	Pyrite-Leach
DKMC-995-145.26-WF1M-L	WF1M-L	Kamoa	Pyrite-Leach
DKMC-995-145.26-WF2M-L	WF2M-L	Kamoa	Pyrite-Leach
DKMC-995-145.26-WF3M-L	WF3M-L	Kamoa	Pyrite-Leach
DKMC-995-145.26-WF4M-L	WF4M-L	Kamoa	Pyrite-Leach
DKMC-995-145.26-WF5NM-L	WF5NM-L	Kamoa	Pyrite-Leach
DKMC-995-145.26-WF6NM-L	WF6NM-L	Kamoa	Pyrite-Leach
KPU-081/557.3a1Apy	a1Apy	Kipushi	Arsenopyrite
KPU-081/557.3a2Apy	a2Apy	Kipushi	Arsenopyrite
KPU-081/557.3a1Ccp	a1Ccp	Kipushi	Chalcopyrite
KPU-081/557.3a2Ccp	a2Ccp	Kipushi	Chalcopyrite
KPU-081/557.3a1Gg	a1Gg	Kipushi	Dolomite
KPU-081/557.3a1Py	a1Py	Kipushi	Pyrite
KPU-081/557.3a2Py	a2Py	Kipushi	Pyrite
KPU-081/557.3a1Apy-L	a1APy-L	Kipushi	Arsenopyrite-Leach
KPU-081/557.3a2Apy-L	a2Apy-L	Kipushi	Arsenopyrite-Leach
KPU-081/557.3a1Ccp-L	a1Ccp-L	Kipushi	Chalcopyrite-Leach
KPU-081/557.3a2Ccp-L	a2Ccp-L	Kipushi	Chalcopyrite-Leach
KPU-081/557.3a1Py-L	a1Py-L	Kipushi	Pyrite-Leach
KPU-081/557.3a2Py-L	a2Py-L	Kipushi	Pyrite-Leach
NS137-1336-1-M1.2	1-M1.2	Chibuluma West	Pyrite
NS137-1336-5-M1.2	5-M1.2	Chibuluma West	Pyrite
NS137-1336-2-MI-Heavy	2-MI-H	Chibuluma West	MI Heavy

NS137-1336-3-MI-Heavy	3-MI-H	Chibuluma West	MI Heavy
NS137-1336-4-MI-Light	4-MI-L	Chibuluma West	MI Light
NS137-1336-5-MI-Light	5-MI-L	Chibuluma West	MI Light
NS137-1336-5-M1.2-L	5-M1.2-L	Chibuluma West	Pyrite-Leach
NS137-1336-1-M1.2-L	1-M1.2-L	Chibuluma West	Pyrite-Leach
NS137-1336-3-MI-Heavy-L	3-MIH-L	Chibuluma West	MI Heavy-Leach
NS137-1336-2-MI-Heavy-L	2-MIH-L	Chibuluma West	MI Heavy-Leach

$^{208}Pb/^{204}Pb$	2 SE	$^{207}Pb/^{204}Pb$	2 SE	$^{206}Pb/^{204}Pb$	2 SE	$^{207}Pb/^{206}Pb$	2 SE
38.179	0.00516	15.714	0.00157	17.934	0.00199	0.876	0.00003
38.212	0.00614	15.722	0.00254	17.945	0.00282	0.876	0.00004
38.204	0.00448	15.719	0.00169	17.940	0.00158	0.876	0.00003
38.214	0.00938	15.721	0.00368	17.946	0.00292	0.876	0.00004
38.236	0.01010	15.731	0.00421	17.959	0.00236	0.876	0.00006
38.215	0.00650	15.721	0.00248	17.948	0.00216	0.876	0.00004
38.208	0.00726	15.720	0.00244	17.946	0.00173	0.876	0.00004
38.202	0.00763	15.721	0.00301	17.950	0.00304	0.876	0.00003
38.195	0.00528	15.715	0.00175	17.953	0.00127	0.875	0.00005
38.207	**0.00688**	**15.720**	**0.00260**	**17.947**	**0.00221**	**0.876**	**0.00004**
38.205	0.00980	15.720	0.00348	17.945	0.00332	0.876	0.00006
38.210	0.00544	15.721	0.00224	17.943	0.00167	0.876	0.00008
38.186	0.00327	15.717	0.00123	17.938	0.00113	0.876	0.00003
38.207	0.00530	15.719	0.00190	17.956	0.00175	0.875	0.00003
38.173	0.00568	15.711	0.00217	17.941	0.00202	0.876	0.00005
38.217	0.00380	15.723	0.00136	17.951	0.00112	0.876	0.00004
38.208	0.00658	15.721	0.00226	17.949	0.00186	0.876	0.00004
38.197	0.00374	15.718	0.00140	17.951	0.00156	0.876	0.00003
38.200	0.00536	15.722	0.00192	17.948	0.00109	0.876	0.00004
38.200	**0.00544**	**15.719**	**0.00200**	**17.947**	**0.00172**	**0.876**	**0.00004**
37.741	0.00542	15.637	0.00202	18.119	0.00192	0.863	0.00004
37.746	0.00446	15.644	0.00181	18.212	0.00178	0.859	0.00002
37.712	0.00540	15.638	0.00182	18.170	0.00210	0.861	0.00004
37.707	0.00462	15.637	0.00166	18.156	0.00153	0.861	0.00003
37.738	0.00630	15.628	0.00238	17.990	0.00232	0.869	0.00005
37.755	0.00810	15.634	0.00276	18.002	0.00266	0.868	0.00005
37.748	0.00406	15.633	0.00155	18.012	0.00149	0.868	0.00003
37.735	**0.00548**	**15.636**	**0.00200**	**18.094**	**0.00197**	**0.864**	**0.00004**
37.754	0.00470	15.656	0.00173	18.272	0.00141	0.857	0.00004
37.713	0.01112	15.647	0.00422	18.287	0.00446	0.856	0.00008

37.740	0.00998	15.643	0.00362	18.244	0.00414	0.857	0.00003
37.724	0.00840	15.644	0.00320	18.237	0.00320	0.858	0.00003
37.727	0.00650	15.648	0.00290	18.213	0.00252	0.859	0.00003
37.771	0.01520	15.667	0.00638	18.248	0.00624	0.859	0.00008
37.738	**0.00932**	**15.651**	**0.00368**	**18.250**	**0.00366**	**0.858**	**0.00005**
53.473	0.06300	18.710	0.02180	68.382	0.08000	0.274	0.00005
52.648	0.06680	17.653	0.02260	50.345	0.06400	0.351	0.00008
47.479	0.01532	18.223	0.00552	58.998	0.01466	0.309	0.00002
57.336	0.03440	19.563	0.01134	82.361	0.04820	0.237	0.00003
41.457	0.01272	16.147	0.00466	25.911	0.00782	0.623	0.00004
43.495	0.02320	16.285	0.00836	28.541	0.01562	0.571	0.00008
51.618	0.02040	17.557	0.00682	48.950	0.01882	0.359	0.00002
61.279	0.01902	24.648	0.00754	163.486	0.04860	0.151	0.00001
61.547	0.02620	19.817	0.00848	86.495	0.03640	0.229	0.00002
51.567	0.00654	18.470	0.00248	63.670	0.00818	0.290	0.00001

$^{206}Pb/^{204}Pb$ C&R Model III Age (Ma)	**$^{206}Pb/^{204}Pb$ S&K 2-Stage Model Age (Ma)**	**μ (238U/204Pb)**
519	490	9.81
514	484	9.81
516	487	9.81
512	483	9.81
505	475	9.81
511	481	9.81
513	483	9.81
511	481	9.81
509	478	9.81
512	**482**	**9.81**
514	484	9.81
515	485	9.81
517	487	9.81
507	477	9.81
516	486	9.81
510	480	9.81
511	475	9.81
509	480	9.81
512	482	9.81
512	**482**	**9.81**
414	375	9.83
360	317	9.84
385	343	9.83

393	353	9.83
488	455	9.81
481	448	9.82
475	442	9.82
428	**390**	**9.82**
326	280	9.84
317	270	9.84
342	297	9.84
346	302	9.84
360	317	9.84
340	295	9.84
338	**294**	**9.84**
-	-	83.44
-	-	57.14
-	-	69.76
-	-	103.82
-	-	21.52
-	-	25.35
-	-	55.11
-	-	222.10
-	-	109.85
-	-	76.57

Table 5.1: Pb isotope results for all CAC deposits obtained from ICP-MC-MS. Bolded values are deposit means. Stacey and Kramers (1975) Two-Stage Model ages are calculated using (Equation 5.1), Cumming and Richards (1975) Model III ages are caluclated using Equation 5.2, and μ values are calculated after Faure and Mensing (2005).

	Equivalent Variable/Coefficent, Value		
Variable/Coefficent	**Stacey and Kramers (1975)**	**Cumming and Richards (1975)**	**Reference**
$(^{206}Pb/^{204}Pb)_i$	x_0, 11.152	a_0, 9.307	Tatsumoto et al., 1973
$(^{206}Pb/^{204}Pb)s$	x, sample	X, sample	-
ε	-	5.00E-11	-
λ	λ_{238}, 0.155125E-9 yr^{-1}	λ_{238}, 0.155125E-9 yr^{-1}	Jaffey et al., 1971
μ	μ, 9.74	αV_p, 10.75	-
t_0	3.700E+09 yr	4.509E+09 yr	-
t	age of sample	age of sample	-

Table 5.2: Compilation of values and coefficents used in Equations 5.1 and 5.2. Values pertaining to the Stacey and Kramers (1975) column correspond to the Two-Stage common Pb model (beginning at 3.7 Ga).

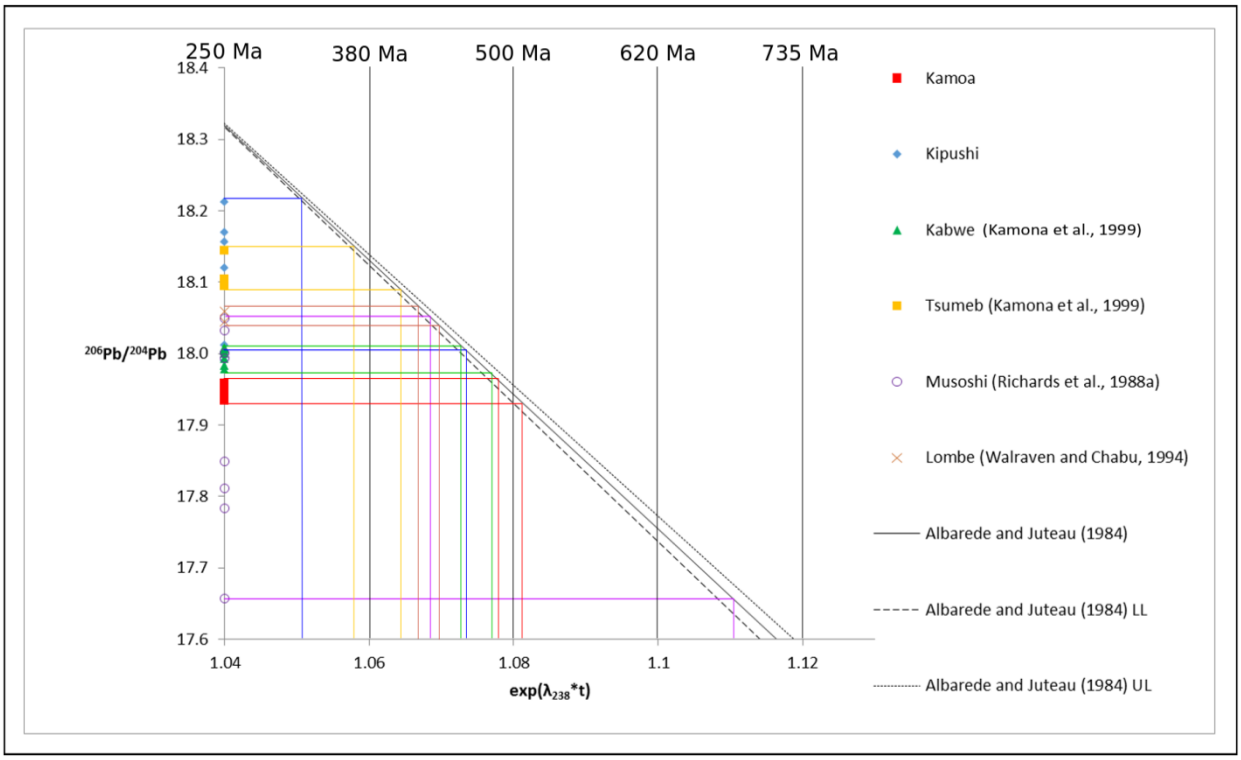

Figure 5.2: Albarede and Juteau (1984) Geochron reference line for $^{206}Pb/^{204}Pb$ as a function of accepted common lead ages ($e^{\lambda 238*t}$). Errors to the Geochron reference line of ± 2% are included per Albarede and Juteau (1984)-LL is lower limit, UL is upper limit. Common lead ratios and ages from the Kamoa and Kipushi deposits (this study) are compared to published data from other CAC deposits. Mineral phases are as follows; Kamoa: pyrite, Kipushi: arsenopyrite, chalcopyrite, and pyrite, Kabwe: galena , Tsumeb: galena, Musoshi: feldspars, Lombe: sulphides.

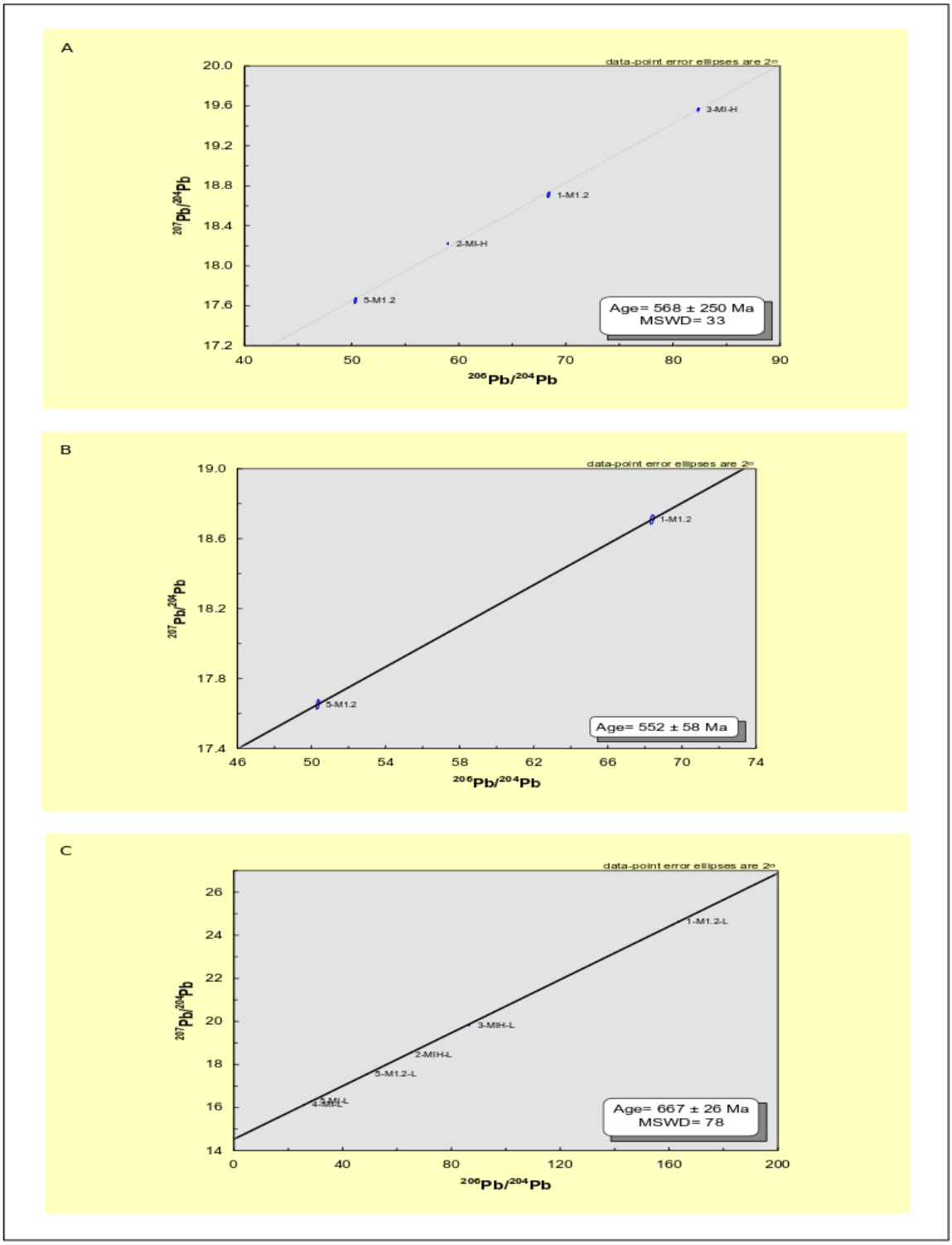
A
data-point error ellipses are 2σ
3-MI-H
1-M1.2
2-MI-H
5-M1.2
Age= 568 ± 250 Ma
MSWD= 33
207Pb/204Pb
206Pb/204Pb
B
data-point error ellipses are 2σ
1-M1.2
5-M1.2
Age= 552 ± 58 Ma
207Pb/204Pb
206Pb/204Pb
C
data-point error ellipses are 2σ
1-M1.2-L
3-MIH-L
2-MIH-L
5-M1.2-L
Age= 667 ± 26 Ma
MSWD= 78
207Pb/204Pb
206Pb/204Pb

Figure 5.3: Pb-Pb isochron (Ludwig, 2003) for samples from the Chibuluma West deposit. Simplified sample names are provided in Table 5.1. **A)** Model 2 isochron of samples from the MI-Heavy mineral separate (includes pyrite). **B)** Two-point pyrite mineral separate regression. **C)** Model 2 isochron of samples from the MI-Light mineral separate, and leachate of both pyrite and MI-Heavy mineral separates.

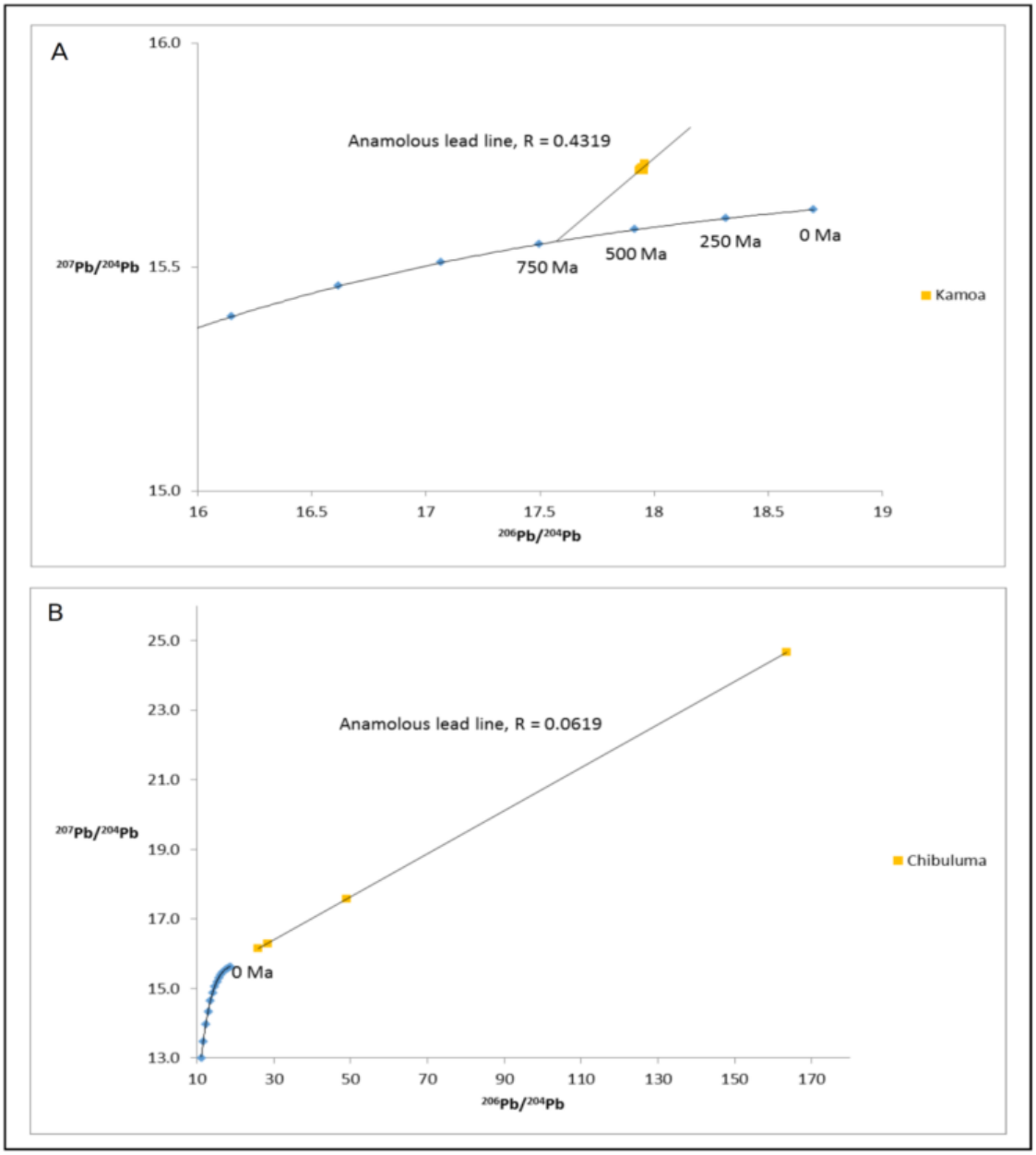

Figure 5.4: $^{206}Pb/^{204}Pb$-$^{207}Pb/^{204}Pb$ crossplot for identifying radiogenic lead. **A)** Kamoa digested pyrite samples are regressed and intersect the Stacey and Kramers (1975) reference line at 731 Ma. **B)** Chibuluma West pyrite and MI-light leachate samples. These samples do not intersect the reference line.

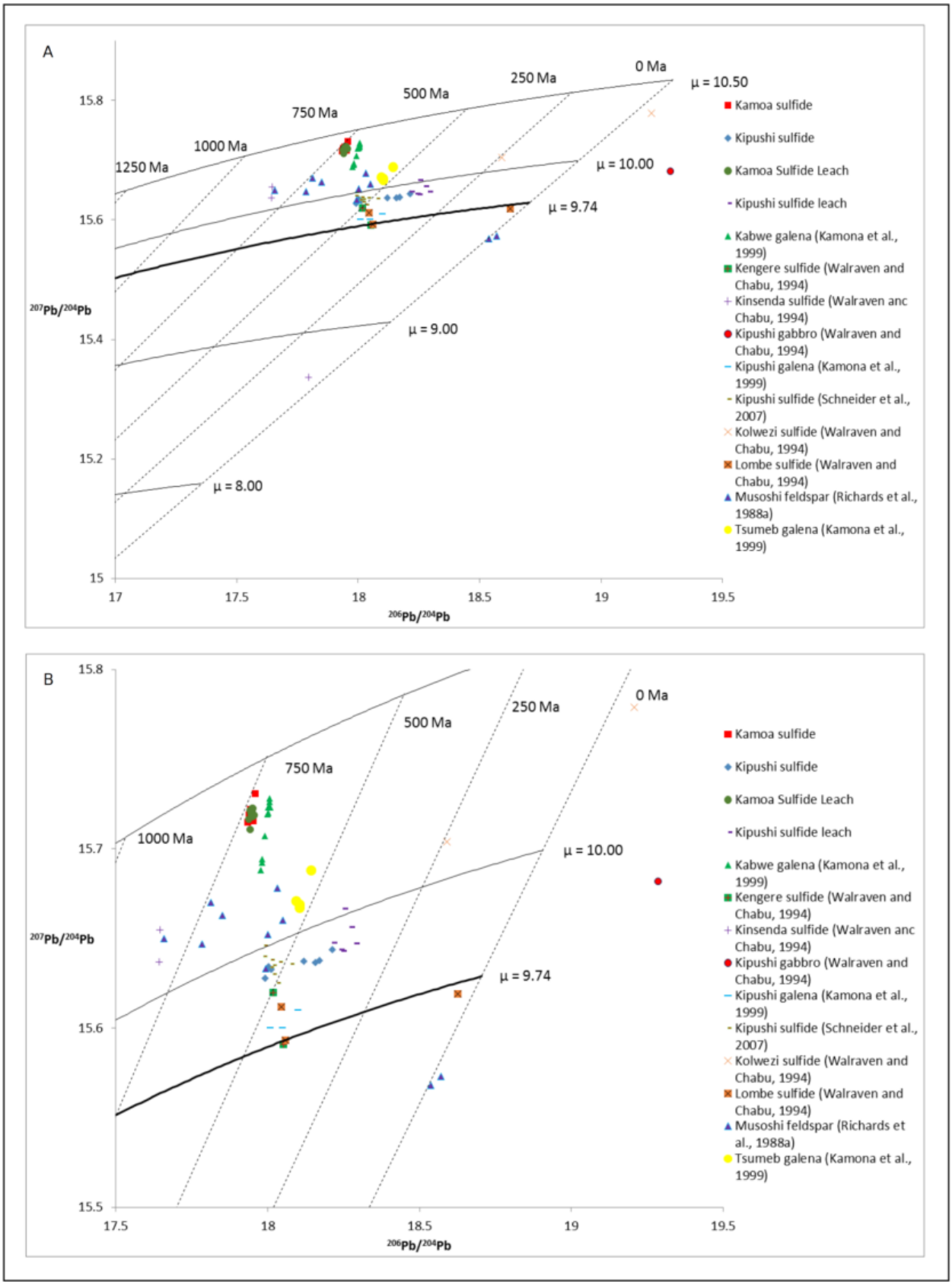
A
0 Ma
250 Ma
500 Ma
750 Ma
1000 Ma
1250 Ma
μ = 10.50
μ = 10.00
μ = 9.74
μ = 9.00
μ = 8.00
15.8
15.6
15.4
15.2
15
17
17.5
18
18.5
19
19.5
207Pb/204Pb
206Pb/204Pb
Kamoa sulfide
Kipushi sulfide
Kamoa Sulfide Leach
Kipushi sulfide leach
Kabwe galena (Kamona et al., 1999)
Kengere sulfide (Walraven and Chabu, 1994)
Kinsenda sulfide (Walraven anc Chabu, 1994)
Kipushi gabbro (Walraven and Chabu, 1994)
Kipushi galena (Kamona et al., 1999)
Kipushi sulfide (Schneider et al., 2007)
Kolwezi sulfide (Walraven and Chabu, 1994)
Lombe sulfide (Walraven and Chabu, 1994)
Musoshi feldspar (Richards et al., 1988a)
Tsumeb galena (Kamona et al., 1999)
B
0 Ma
250 Ma
500 Ma
750 Ma
1000 Ma
μ = 10.00
μ = 9.74
15.8
15.7
15.6
15.5
17.5
18
18.5
19
19.5
207Pb/204Pb
206Pb/204Pb
Kamoa sulfide
Kipushi sulfide
Kamoa Sulfide Leach
Kipushi sulfide leach
Kabwe galena (Kamona et al., 1999)
Kengere sulfide (Walraven and Chabu, 1994)
Kinsenda sulfide (Walraven anc Chabu, 1994)
Kipushi gabbro (Walraven and Chabu, 1994)
Kipushi galena (Kamona et al., 1999)
Kipushi sulfide (Schneider et al., 2007)
Kolwezi sulfide (Walraven and Chabu, 1994)
Lombe sulfide (Walraven and Chabu, 1994)
Musoshi feldspar (Richards et al., 1988a)
Tsumeb galena (Kamona et al., 1999)

Figure 5.5: Two-Stage Stacey and Kramers (1975) growth lines for different μ, compared to the reference line (μ = 9.74 in bold). **A)** Total field to show location for all deposits. **B)** Zoomed-in to show detail in ROI containing a high density of deposits.

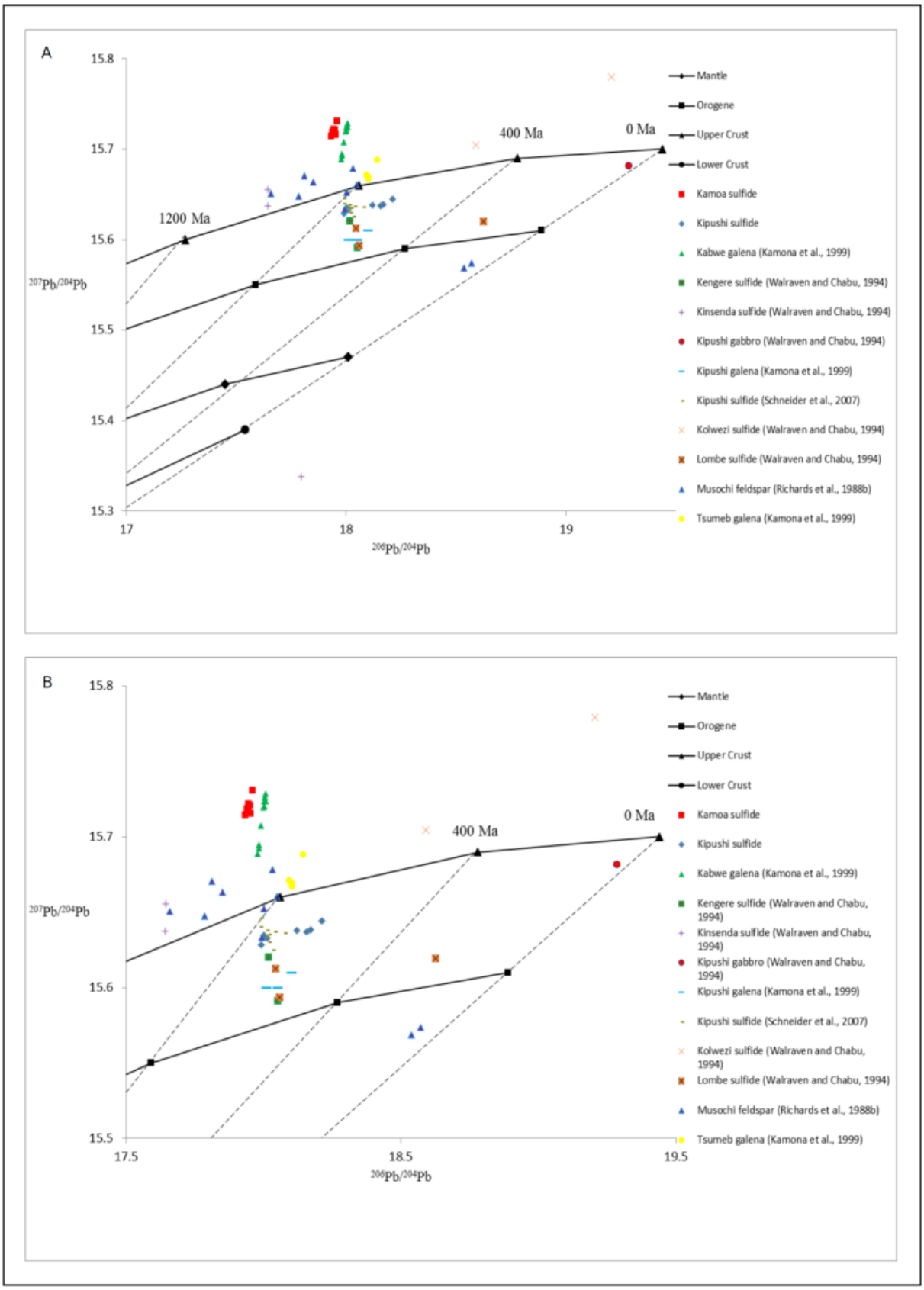
A
15.8
15.7
15.6
15.5
15.4
15.3
17
18
19
$^{207}Pb/^{204}Pb$
$^{206}Pb/^{204}Pb$
1200 Ma
400 Ma
0 Ma
Mantle
Orogene
Upper Crust
Lower Crust
Kamoa sulfide
Kipushi sulfide
Kabwe galena (Kamona et al., 1999)
Kengere sulfide (Walraven and Chabu, 1994)
Kinsenda sulfide (Walraven and Chabu, 1994)
Kipushi gabbro (Walraven and Chabu, 1994)
Kipushi galena (Kamona et al., 1999)
Kipushi sulfide (Schneider et al., 2007)
Kolwezi sulfide (Walraven and Chabu, 1994)
Lombe sulfide (Walraven and Chabu, 1994)
Musochi feldspar (Richards et al., 1988b)
Tsumeb galena (Kamona et al., 1999)
B
15.8
15.7
15.6
15.5
17.5
18.5
19.5
$^{207}Pb/^{204}Pb$
$^{206}Pb/^{204}Pb$
400 Ma
0 Ma
Mantle
Orogene
Upper Crust
Lower Crust
Kamoa sulfide
Kipushi sulfide
Kabwe galena (Kamona et al., 1999)
Kengere sulfide (Walraven and Chabu, 1994)
Kinsenda sulfide (Walraven and Chabu, 1994)
Kipushi gabbro (Walraven and Chabu, 1994)
Kipushi galena (Kamona et al., 1999)
Kipushi sulfide (Schneider et al., 2007)
Kolwezi sulfide (Walraven and Chabu, 1994)
Lombe sulfide (Walraven and Chabu, 1994)
Musochi feldspar (Richards et al., 1988b)
Tsumeb galena (Kamona et al., 1999)

Figure 5.6: Plumbotectonics model as in Zartman and Doe (1981) for the potential Pb source reservoirs. **A)** Total field to show location for all deposits. **B)** Zoomed-in to show detail in ROI containing a high density of deposits.

6) Oxygen Isotope Geochemistry

6.1 Background

Stable isotopes can reveal much information regarding the formation of mineral deposits. Often, C and O isotopes are used for fluid source tracing purposes, especially when the deposit contains carbonate phases grown in equilibrium with the ores. One common application, which has also been explored herein, is to use oxygen isotopes to estimate fluid temperature and the time length of ore formation via diffusion.

There are three sequences of carbonate mineralization at the Kipushi deposit. The host rock (Kakontwe Formation) is dolomitic and precedes any ore mineralization. A later syn-ore dolomite was precipitated alongside the Cu-Pb-Zn minerals. The ore formation was followed by a post-ore calcite. Extensive petrographic and paragenetic information detailing these carbonates can be found in (Heijlen et al., 2008; Van Wilderode et al., 2013).

6.2 Sampling and Isotope Analysis

Hand samples (as explained above) taken from core cuttings were used to sample these three carbonate generations. Each carbonate was identified under binocular microscope and marked for future collection (Figure 6.1). Dolomite was distinguished from calcite due to a less vigorous reaction with HCl. In addition, calcite displayed a characteristic light green reflectance, and often formed euhedral crystals. The carbonates were removed from hand sample with a Dremel drill press and stored in glass vials. Replicates were done on those samples where enough material was able to be extracted from the same drill site. Samples from the same generation are from different drill sites. The carbonate was accurately weighed to masses ranging from 100 to 500 μg and load into a glass vial. Atmospheric gases were removed by purging for 10 minutes with high-purity helium gas ($He_{(g)}$). The carbonate sample was allowed

to react with ~1 ml of 103 % H_3PO_4 (phosphoric acid) at 72°C for at least 1 hour, producing carbon dioxide gas ($CO_{2(g)}$) (McCrea, 1950). The produced $CO_{2(g)}$ was sent via $He_{(g)}$ to a Gasbench II system, and then to a Thermo Scientific MAT 253 isotope ratio mass spectrometer (IRMS). All C and O isotopic measurements were made in the Stable Isotope Geochemistry Laboratory at the University of Alberta. The measured CO_2 masses were 44, 45, and 46 for $^{12}C^{16}O^{16}O$, $^{13}C^{16}O^{16}O$, and $^{12}C^{18}O^{16}O$ respectably. Each analysis consisted of 10 separate on-peak measurements, with the mean value taken and used in the proceeding data reduction. Faraday cup calibration was performed at the beginning of each analytical session. Instrumental drift was accounted for by intermittent measurement of two in-house standards. Samples were normalized to international standard NBS-18. For dolomite samples, an equilibration fractionation factor was applied (Sharma and Clayton, 1965; Kim et al., 2015). Values are reported in the δ notation relative to the V-PDB standard for $\delta^{13}C$ and to both V-PDB and V-SMOW for $\delta^{18}O$.

6.3 Results

The results can be found in Table 6.1 (Coplen et al., 1983). For replicate analyses, the reported value is the mean of the two measurements unless the absolute difference exceeds 0.5 ‰. In other words, $|\Delta^A X| = \delta^A X_2 - \delta^A X_1$, where $|\Delta^A X| \leq 0.5$ ‰. If the difference exceeds the 0.5 ‰ threshold, then the isotopic value from both analyses are reported. All isotopic measurement was performed over two days. The 2 σ analytical errors are 0.28 ‰ ($\delta^{13}C$) and 0.25 ‰ ($\delta^{18}O$) for Day 1, and 0.14 ($\delta^{13}C$) ‰, and 0.16 ‰ ($\delta^{18}C$) for Day 2. The reduction in error is attributed to an approximate doubling of sample mass-improving the signal strength.

6.4 Discussion

6.4.1 Oxygen Diffusion

Pre-existing stable isotope data from the Kipushi deposit provided in Van Wilderode et al. (2013) have been compared to the results from this study (Figure 6.2). The depths of the samples taken for the study conducted by Van Wilderode et al. (2013) are located between 725-850 m for the host rock, while ore-stage (syn-ore) carbonate came from a lower depth (~942 m). All samples from this study are taken a much more restricted depth, ranging from 557-573 m. This improved spatial variability allows for the isotopic data from one carbonate generation to another to be more meaningfully compared, as the distance between samples is significantly reduced. Indeed, the host rock $\delta^{13}C$ from 725-850 m shows a ~ 5 ‰ difference when compared to the host rock from 557-573 m. Similarly, the $\delta^{18}O$ shows ~10 ‰ for the same depths. Interestingly, the gangue, or syn-ore carbonate are very similar. Therefore, there are likely significant differences in the Kakontwe Formation host rock at Kipushi, while the dolomite produced from the ore fluid was relatively homogenous. This implies that wall-rock interaction did not have a significant effect on the syn-ore dolomite.

The apparent mixing of both host rock dolomite and syn-ore dolomite endmembers (Figure 6.2) indicates that some fraction of both was sampled. The distance between the centres of each drill pit is 1 mm, as the radius of each drill pit is 0.5 mm. At the interface between these two carbonate endmembers (± 0.5 mm) lies the location of the intermediate (isotopically mixed) samples. There would not be any isotopic fractionation between these two carbonate generations, as they are of the same phase. Isotopic equilibrium would be reached when the $\delta^{18}O$ of both endmembers is equivalent ($\delta^{18}O_{Phase\ A} = \delta^{18}O_{Phase\ B}$)-occuring at t_{EQ}. (O'Neil and Epstein, 1966) (Figure 6.3). This median value would be found at the ± 0.5 mm interface. For example, the median $\delta^{18}O$ value for both endmembers is -13.3 ± 0.3 ‰, while the measured diffusion

profile in Figure 6.4 at 0.5 mm produces a $\delta^{18}O$ of -13.2 ± 0.6 ‰. These nearly identical values correspond to the location of the endmember interface, and is taken to be correct.

While the results from this study are scrutinized below, it must be stated that diffusion is a complicated process, with many variables and parameters. There are several assumptions that were made or omitted, including grain size and ensuing geometry of diffusion (ex: circle, rectangle, and their 3D counterparts) (Dodson, 1979), isotopic homogeneity and constant temperature throughout the entire mineralization from the ore-stage fluid, interpolation of intermediate points when constructing the measured diffusion profile, available D_0 not at desired temperatures, and the lack of D_0 for wet dolomite.

The latter of these complicating factors was considered, however, despite the paucity of diffusion rates for carbonate. Oxygen diffusion rates for both dry dolomite (Anderson, 1972) and wet calcite (Kronenberg et al., 1984) were used. Additionally, it is unknown which of these two carbonates experiences faster diffusion. Oxygen diffusion in dry dolomite has been shown to be ~100 times faster than for dry calcite over a temperature range of 650-800°C (Anderson, 1972). Conversely, Northrup and Clayton (1966) determined calcite had a greater oxygen diffusion rate. Given that both the host rock, and the syn-ore carbonates at Kipushi were deposited underwater, and from a hydrothermal fluid respectably, the diffusion modelling herein assumed wet conditions. Wet dolomite was simulated by using the oxygen diffusion rate of Anderson (1972), and modifying it per Kronenberg et al. (1984). Oxygen diffusion for wet calcite (Kronenberg et al., 1984) was also modelled. Experimental data from Anderson (1972), and Kronenberg et al. (1984) was extrapolated to temperatures expected for greenschist facies as obtained through conventional means (Figure 6.5). The oxygen diffusion rate for simulated wet dolomite was calculated by multiplying the oxygen diffusion rate for dry dolomite determined

from Figure 6.5A by 10^2 as explained above. The oxygen diffusion rates for wet calcite, dry dolomite, and simulated wet dolomite are provided in Table 6.2. Chlorite-quartz geothermometry for Kipushi places a temperature range on the ore fluid ranging from 287-331°C (Chabu, 1995), while chlorite-sphalerite geothermometry yielded temperatures from 290-380°C (Heijlen et al., 2008). Homogenization temperatures from primary fluid inclusion assemblages at Kipushi yielded $T_{h(bubble)}$ 339°C, and up to $T_{h(halite)}$ 360°C (Heijlen et al., 2008). These temperatures represent minimums, and the true trapping temperature may be higher.

Diffusion between two phases in disequilibrium with respect to some concentration ($\delta^{18}O$) can be modelled using a polynomial function (Hume-Rothery, 1966) (Figures 6.3 and 6.4). The concentration therefore is a function of both distance and time and can be determined following Fick's Second Law:

$$\frac{\partial c}{\partial t} = D\frac{\partial^2 c}{\partial x^2}. \qquad \textit{EQ. 6.1}$$

The concentration C, ($\delta^{18}O$) changes with respect to the diffusion coefficient (D) time and area x^2 (distance). The diffusion length (L) is the one-dimensional distance in which the more concentrated phase will have diffused into the less concentrated phase. This distance assumes that the more concentrated phase remained in stasis (closed system), and can be determined using Equation 6.2 below.

$$L = \sqrt{(Dt)} \qquad \textit{EQ. 6.2}$$

The actual $\delta^{18}O$ concentration at some location and time c(x, t) is calculable using Equation 6.3, after Crank (1956), and Kronenberg et al. (1984).

$$\frac{c_1 - c(x,t)}{c_1 - c_0} = \mathrm{erf}\left(\frac{x}{2\sqrt{Dt}}\right), \qquad \textit{EQ. 6.3}$$

where the more concentrated phase c_1 (syn-ore) diffuses into the less concentrated phase c_0 (host rock). Rearranging for c(x, t) and simplifying, Equation 6.3 becomes:

$$c(x,t) = -\operatorname{erf}\left(\frac{x}{2L}\right)(-(c_1 - c_0) + c_1\ ). \qquad \textit{EQ. 6.4}$$

The error function (erf(x)) must be computed over a positive (absolute) distance $0 \leq x_1 \leq x_2$, as diffusion will only occur from c_1 to c_0. That is, for a uniform $\delta^{18}O$ c_1 (syn-ore) reservoir, the isotopic flux is zero, instead, the isotopic flux progresses in one direction to c_0. The error function over some domain may either be calculated using Equation 6.5, or by referencing an Error Function Table (Hahn and Özişik, 2012).

$$\operatorname{erf}(x) = \frac{2}{\sqrt{\pi}}\int_0^x e^{-t^2}\,dt. \qquad \textit{EQ. 6.5}$$

Important parameters such as the temperature and the residence time of the hydrothermal fluid can be constrained by iteratively changing these variables and producing theoretical diffusion profiles (using Equation 6.5), which are then compared to the measured diffusion profile. When the theoretical profile (with the interpolated points-determined by 2nd order polynomial line of best fit between the three measured points; syn-ore, syn-ore+host-rock, and host-rock) matches the measured profile, the corresponding variables used to construct the theoretical profile are a reasonable estimate for the mineralizing fluid (Figures 6.6-6.7). These profiles were made for both wet calcite, and for simulated wet dolomite.

For wet calcite, when T = 500°C, and t = 5 Ma$\leq t_r \leq$ 10 Ma, the theoretical diffusion profile best matches the measured diffusion profile (Figures 6.6B-C). These conditions produce a theoretical profile that is very close to the measured profile. At temperatures below 500°C, and residence times (t_r) below 5 Ma, oxygen diffusion is very minimal. When the expected temperatures (350-400°C) are used (Figure 6.6F-I) with time up to 10 Ma, the theoretical

diffusion profile is dissimilar to the measured profile. For the two profiles to match, either the time and/or the temperature must be set to values far in excess of what would be geologically reasonable for the Kipushi deposit.

For simulated wet dolomite, when T = 350°C, and t = 1 Ma $\leq t_r \leq$ 5 Ma, the theoretical diffusion profile best matches the measured diffusion profile (Figure 6.7F-G). This temperature is in excellent agreement with pre-existing temperatures for the Kipushi deposit determined through chlorite-quartz geothermometry (287-331°C), and chlorite-sphalerite geothermometry (290-380°C), Chabu, 1995 and Heijlen et al. (2008) respectably. The 350°C estimate is also supported by 339-360°C homogenization temperatures from Kipushi (Heijlen et al., 2008).

In either case, the time and temperature conditions for the Kipushi deposit support a relatively high temperature of at least 350°C, and possibly up to 500°C. While the latter temperature is higher than reported by conventional means (Chabu, 1995; Heijlen et al., 2008), it is not an unreasonable estimate. Timing of ore formation in the Kipushi deposit consistently returns ages of ~450 Ma, which have been linked to a nearby amphibolite grade (~750°C) syenite intrusion-also dated at ~450 Ma (Cosi, et al., 1992; Walraven and Chabu, 1994; Kamona et al., 1999; John et al., 2004; Schneider et al., 2007). Annels (1989), notes that a temperature range of 300-510°C is reasonable for the late-stage vein mineralization at Chambishi. The high temperature is attributed to amphibolite grade gabbro intrusion. The estimated temperature window from 350-500°C corroborates pre-existing temperature data, and temperatures associated with the greenschist facies observed at Kipushi (Annels, 1989; Heijlen et al., 2008).

Again, solid-state oxygen diffusion in dry dolomite would be essentially non-existent. As an example, at a constant temperature of 400°C, the diffusion rate is 10^7 times slower in dry dolomite than for wet calcite. For a constant temperature of 350°C, oxygen diffusion in dry

dolomite is 10^9 times slower. For temperatures proposed by Annels (1989) for sediment-hosted mineralization (<200°C), dry dolomite is 10^4 times slower than simulated wet dolomite. Measured oxygen diffusion is the result of the time of length of mineralization, or residence time of the hydrothermal fluid, and not the result of a passive, solid-state. There is no evidence that the ores are remobilized from a previous mineralization event, as the host rock isotopic value should record homogenization during the later syn-ore mineralization event. Coupled with the theoretical modelling that solid-state diffusion has not produced the measured oxygen diffusion profile, the isotopic signature of the host rock is likely original.

For either a 350°C, or a 500°C hydrothermal fluid, the residence time is estimated to be less than 10 Ma. This shorter period of mineralization does not support a protracted time of ~100 Ma (Hitzman et al., 2005; Hitzman et al., 2010). At a small x_n of 0.01 mm, where diffusion would be most noticeable, with an upper T estimate for sediment-hosted deposits of 200°C (Annels, 1989), and t of 100 Ma (Hitzman et al., 2010) the theoretical $\delta^{18}O$ is -13.2 ‰ V-PDB. At all x_n beyond 0.1 mm, the theoretical $\delta^{18}O$ is -13.9 ‰ V-PDB (the same value of the host rock). This indicates that essentially zero diffusion will occur under these conditions and that a protracted mineralization at a low temperature is incorrect for this sediment-hosted ore.

In summary, these data do not support a remobilized syngenetic/diagenetic origin for Kipushi ore, but a purely epigenetic one. Isotopic homogenization of a syngenetic/diagenetic carbonate with the syn-ore carbonate is not viable, as the host rock carbonate was not homogenized as its isotopic composition is unique. For a syngenetic/diagenetic origin, there should be isotopic evidence of this ore fluid. Instead, the isotopic value for the host rock carbonate seems to be unaltered-ruling out an early mineralization. The bracketed temperature range of 350-500°C is also in discord with a syngenetic/diagenetic origin. Fluid inclusion

homogenization temperatures associated with a diagenetic to pre-Lufilian fluid from the Chambishi deposit (also in CAC) were found to be 160-170°C (Annels, 1989), while a T_h of ~230°C was found for the similar, sediment-hosted Cu-Ag Spar Lake deposit (Hayes, 1990). For the minimum temperature of 350°C, this produces a difference of at least 180°C for Chambishi, and 120°C for Spar Lake. Temperatures proposed for sediment-hosted deposits under a protracted time of mineralization cannot produce the measured diffusion profile, and are not reasonable for this deposit either.

6.4.2 Identification of a Separate, Post-Ore Fluid

The existence of a post-ore calcite at Kipushi is well established in published paragenetic studies (Heijlen et al., 2008; Van Wilderode et al., 2013). In these studies, the post-ore calcite post-dates the syn-ore dolomite, and is not associated with any sulphide mineralization. The observed isotopic difference for both of these carbonate generations can be the result from either temperature evolution of a single fluid, or two separate fluids precipitating one of these carbonates apiece. If both carbonates are from a single fluid, then the syn-ore dolomite and post-ore calcite are in isotopic equilibrium, and the observed fractionation is phase dependent. If it can be shown that the observed isotopic fractionation cannot be accounted for under this assumption, then these two carbonate generations did not derive from a single fluid, but from two discrete fluids. In a single fluid, a pair of minerals in isotopic equilibrium has only phase dependent fractionation as shown below;

$$\delta^{18}O_A - \delta^{18}O_B = \Delta_{A-B} \approx 10^3 ln\alpha. \qquad EQ.\ 6.6$$

Equation 6.6 shows that the difference between two phases, $\delta^{18}O_A$ (syn-ore dolomite) from $\delta^{18}O_B$ (post-ore calcite) is accounted for by the fractionation factor ($10^3 \ln\alpha$). This fractionation factor is unique to the mineral pair in question, and is temperature sensitive. Fortunately, as both

carbonates' oxygen isotopic values have been measured, the theoretical value for either phase may be calculated. The theoretical oxygen values for $\delta^{18}O_B$ are provided in Table 6.3. A temperature range from 250°C to 600°C was used for calculations. While temperatures below 250°C are reasonable for the post-ore calcite, the isotopic fractionation only becomes more severe at lower temperatures. This can be seen in Table 6.3, as the isotopic fractionation increases inversely with temperature decrease. At 250°C, the theoretical $\delta^{18}O$ for post-ore calcite is 15.9 ‰ V-SMOW, a difference of 4.5 ‰ from the measured $\delta^{18}O$ value of 20.4 ‰ V-SMOW. Since the theoretical values are not realized at any reasonable temperature, the assumption required for single-fluid-phase-dependent fractionation as per Equation 6.6 fails. Therefore, these two carbonate generations could not have been derived from a single fluid.

Modifying Equation 6.6 for a mineral-fluid pair, the $\delta^{18}O$ of the fluid may be calculated. In the calcite-H_2O system;

$$\delta^{18}O_{H2O} = -\Delta_{Calcite-H2O} + \delta^{18}O_{Calcite} \qquad EQ.\ 6.7$$

and for the dolomite-H2O system;

$$\delta^{18}O_{H2O} = -\Delta_{Dolomite-H2O} + \delta^{18}O_{Dolomite}. \qquad EQ.\ 6.8$$

The $\delta^{18}O$ of the fluid can be calculated as in either Equations 6.7 or 6.8 because the $\delta^{18}O$ value for calcite and dolomite have been measured via IRMS, and the fractionation factor between Phase A and Phase B are known for a given temperature. Similar to the assumption made in Equation 6.6, both fluids in Equations 6.7-6.8 are in isotopic equilibrium if the calculated $\delta^{18}O$ values overlap at some temperature. If the $\delta^{18}O$ values overlap, then the two minerals were derived from a singular fluid. If the $\delta^{18}O$ values are unique at all temperatures, then the two minerals were derived from two separate fluids. That is, Equations 6.7-6.8 are invalid as the mineral-fluid pairs were not in equilibrium irrespective of temperature. Calculated $\delta^{18}O$ values

of the fluids in both mineral-fluid pairs is provided in Table 6.4 for a temperature range from 100-600°C. Over this temperature range, an isotopic fractionation of 3.3 to 8.2 ‰ is observed. This large variability is much larger than the 2σ instrumental uncertainty of 0.2 ‰ for $\delta^{18}O$, indicating that these discrepancies are geological. Due to this large isotopic difference between the two fluids, they cannot have been in equilibrium over this temperature range, and must be two distinct fluids with unique isotopic composition.

6.4.3 Fluid Source Tracing

The sensitivity of oxygen isotope fractionation to changes in temperature, makes assigning a singular fluid source difficult. Mixed-signals may result from two or more endmember fluid sources at different temperatures contributing to the overall, intermediary isotopic value. If, the post-ore calcite ($\delta^{18}O$ of 20.4 ‰ V-SMOW) precipitated from a fluid at 100°C, than the corresponding fluid would have a $\delta^{18}O$ value of 7.3 ‰ V-SMOW-an igneous source (Campbell and Larson, 1998). At a temperature of 500°C, the $\delta^{18}O$ value of the fluid equals 18.8 ‰ V-SMOW-indicative of fluid contributed from deep marine sediments (Campbell and Larson, 1998). Clearly, temperature constraint must precede fluid source tracing, as vastly different fluid resevoirs, with vastly differing geological interpretations result if this parameter is unknown.

For the estimated temperature of 350°C for the syn-ore dolomite, the corresponding fluid would have a $\delta^{18}O$ of - 15.3 ‰ V-SMOW (Equation 6.8). A likely mixing of igneous (ex: syenite $\delta^{18}O$ 6 ‰ V-SMOW) and atmospheric O_2 (23.5 ‰ V-SMOW) endmembers could produce the intermediary value above (Taylor, 1968; Kroopnick and Craig, 1972; Campbell and Larson, 1998; Fricke and O'Neill, 1999). The hydrothermal fluids of sediment-hosted deposits, are associated with an igneous source (Kamona et al., 1999; Frimmel et al., 2004; Hitzman et al.,

2010). Hitzman et al. (2010) notes that both fluid and metal is supplied to sediment-hosted deposits by a mafic source. For Tsumeb-type deposits, located in the Damaran-Lufilian orogenic belt (includes CAC), a magmatic fluid origin is proposed (Kamona et al., 1999). Additionally, in the Neoproterozoic Gariep Belt of Namibia, Pb is intimately associated with syenite intrusions (Frimmel et al., 2004).

For an estimated temperature of 500°C for the syn-ore dolomite, the corresponding fluid would have a $\delta^{18}O$ of 17.5 ‰ V-SMOW-indicative of a deep marine sediment (Campbell and Larson, 1998). However, this is not a likely fluid source as the Kipushi deposit it well-linked to an intrusion and the Kakontwe Formation host rock experienced basin inversion and metamorphism. Instead, a mixing of the same endmembers as mentioned at T = 350°C would accommodate this value, although the atmospheric component of the fluid would be relatively larger. In lieu of a magmatic source, a meteoric source ($\delta^{18}O \leq 0$ ‰ V-SMOW) is reasonable. Regardless, a source with a high $\delta^{18}O$ value (atmospheric O_2 $\delta^{18}O > 23.5$ ‰ V-SMOW) is required to compensate for the relatively high syn-ore and post-ore carbonates.

Finally, the post-ore calcite appears to be associated with a separate, supergene enrichment event. Additionaly evidence for this can be found from the ~300 Ma with the Re-Os, and leachate Pb data, as well as the lower shear strain in the calcite. The temperature of the fluid in isotopic equilibrium with the post-ore calcite would have a $\delta^{18}O$ of 13.0 ‰ V-SMOW at 200°C, decreasing to ≤ 7.3 ‰ V-SMOW at ≤ 100°C. These values alone suggest an igneous fluid source (Campbell and Larson, 1998), although at ~300 Ma, the CAC and the Katangan Basin is quiescent (Guiraud et al., 2005). Instead, a fluid mixing between an atmospheric source and a groundwater/meteoric source may yield the ~10 ‰ values. This type of fluid source is also

the most geologically reasonable for the CAC during the Paleozoic, and may be linked to fluid mobilization due due to the tectonic front at southern Gondwana ca 250 Ma (Daly et al., 1992).

6.5 Conclusion

Oxygen diffusion has been shown to provide reasonable estimates for T-t fluid conditions. One advantage to this approach is the ability to estimate the entire time length of mineralization. When coupled with geochronology, a more complete understanding of the fluid history is possible. An absolute time in history can be assigned to ore formation, but the length of time in which that ore formation occurred can also be estimated. The 350-500°C temperature estimates are in close agreement with by pre-existing data determined from fluid inclusions, and geothermometry. Temperatures expected for syngenetic/diagenetic mineralization are not supported, nor is a protracted mineralization time. Instead, mineralization is epigenetic, and occurred for <10 Ma at high temperatures, not for 100 Ma at low temperatures. Equilibrium calculations prove that the post-ore calcite generation could not have crystallized from the syn-ore dolomite generation at any geologically reasonable temperature. That is, these two carbonate generations are discrete and highlight a possible major time discrepancy in the paragenesis from ore mineralization, to some (much?) later mineralization event. The hydrothermal fluid for both the syn-ore and post-ore carbonates is the result of endmember mixing. Given the relatively high $\delta^{18}O$ values, an atmospheric source is required at least in part for both the syn-ore and post-ore fluids, while a magmatic component (and source of metal) is reasonable as Kipushi is linked to nearby intrusions.

6.6 References

Anderson, T.F., 1972, Self-diffusion of carbon and oxygen in dolomite, Journal of Geophysical Research, v. 77, p. 857-861

Annels, A.E., Vaughn, D.J., and Craig, J.R., 1983, Conditions of ore mineral formation in certain Zambian Copperbelt deposits with special reference to the role of cobalt, Mineralium Deposita, v. 18, p. 71-88

Campbell, A.R., and Larson, P.B., 1998, Introduction to stable isotope applications in hydrothermal systems, *In:* Richards, J.P., and Larson, P.B., (Eds), Techniques in Hydrothermal Ore Deposits Geology, Reviews in Economic Geology, v. 10, Society of Economic Geologists, Littleton, USA

Chabu, M., 1995, The geochemistry of phlogopite and chlorite from the Kipushi Zn-Pb-Cu deposit, Shaba, Zaire, The Canadian Mineralogist, v. 33, p. 547-558

Chacko, T., Deines, P., 2008, Theoretical calculation of oxygen isotope fractionation factors in carbonate systems, Geochimica et Cosmochimica Acta, v. 72, p. 3642-3660

Coplen, T.B., Kendall, C., and Hopple, J., 1983, Comparison of stable isotope reference samples, Nature, v. 302, p. 236-238

Cosi, M., De Bonis, A., Gosso, G., Hunziker, J., Martinotti, G., Moratto, S., Robert, J.P., and Ruhlman, F., 1992, Late Proterozoic thrust tectonics, high-pressure metamorphism and uranium mineralization in the Domes Area, Lufilian Arc, northwestern Zambia, Precambrian Research, v. 58, p. 215-240

Crank, J., 1956, The Mathematics of Diffusion, Oxford University Press, London, p. 414

Daly, M.C., Lawrence, S.R., Diemu-Tshiband, K., and Matouana, B., 1992, Tectonic evolution of the Cuvette Centrale, Zaire, Journal of the Geological Society, London, v. 149, p. 539-546

Dodson, M.H., 1979, Theory of cooling ages, *In:* Jäger, E., and Hunziker, J.C., (Eds), Lectures in Isotope Geology, Springer-Verlag, Berlin, Germany

Fricke, H.C., and O'Neill, J.R., 1999, The correlation between $^{18}O/^{16}O$ ratios of meteoric water and surface temperature: its use in investigating terrestrial climate change over time, Earth and Planetary Science Letters, v. 170, p. 181-196

Frimmel, H.E., Jonasson, I.R., and Mubita, P., 2004, An Eburnean base metal source for sediment-hosted zinc-lead deposits in Neoproterozoic units of Namibia: Lead isotopic and geochemical evidence, Mineralium Deposita, v. 39, p. 328-343

Guiraud, R., Bosworth, W., Thierry, J., and Delplanque, A., 2005, Phanerozoic geological evolution of Northern and Central Africa: An overview, Journal of African Earth Sciences, v. 43, p. 83-143

Hayes, T.S., 1990, A preliminary study of thermometry and metal sources of the Spar Lake strata-bound copper-silver deposit, Belt Supergroup, Montana, United States Geological Survey Open-File Report 90-0484, p. 1-30

Heijlen, W., Banks, D.A., Muchez, P. Stensgard, B.M., and Yardley, B.W.D., 2008, The nature of the mineralizing fluids of the Kipushi Zn-Cu deposit, Katanga, Democratic Republic of Congo: Quantitative fluid inclusion analysis using laser ablation ICP-MS and bulk crush-leach methods, Economic Geology, v. 103, p. 1459-1482

Hitzman, M.W., Kirkham, R., Broughton, D., Thorson, J., and Selley, D., 2005, The sediment-hosted stratiform copper ore system, *In:* Hedenquist, J.W., Thompson, J.F.H., Goldfarb, R.J., and Richards, J.P., (Eds), Economic Geology One Hundredth Anniversary Volume 1905-2005, Society of Economic Geologists, Littleton, USA

Hitzman, M.W., Selley, D., and Bull, S., 2010, Formation of sedimentary copper deposits through Earth history, Economic Geology, v. 105, p. 627-639

Hu, G., and Clayton, R.N., 2003, Oxygen isotope salt effects at high pressure and high temperature and the calibration of oxygen isotope geothermometers, Geochimica et Cosmochimica Acta, v. 67, p. 3227-3246

Hume-Rothery, W., 1966, The Structure of Alloys or Iron: An Elementary Introduction, Pergamon Press, p. 347

Jacobsen, S.B., and Kaufman, A.J., 1999, The Sr, C and O isotopic evolution of Neoproterozoic seawater, Chemical Geology, v. 161, p. 37-57

John, T., Schenk, V., Mezger, K., and Tembo, F., 2004, Timing and PT evolution of whiteschist metamorphism in the Lufilian Arc-Zambezi Belt Orogen (Zambia): Implications for the assembly of Gondwana, Journal of Geology, v. 112, p. 71-90

Kamona, A.F., Lévêque, J., Friedrich, G., and Haack, U., 1999, Lead isotopes of the carbonate-hosted Kabwe, Tsumeb, and Kipushi Pb-Zn-Cu sulfide deposits in relation to Pan African orogenesis in the Damaran-Lufilian fold belt of Central Africa, Mineralium Deposita, v. 34, p. 273-283

Kaufman, A.J., Hayes, J.M., Knoll, A.H., and Germs, G.J.B., 1991, Isotopic compositions of carbonates and organic carbon from upper Proterozoic successions in Namibia: stratigraphic variation and the effects of diagenesis and metamorphism, Precambrian Research, v. 49, p. 301-327

Kaufman, A.J., Hayes, J.M., Knoll, A.H., and Germs, G.J.B., 1991, Isotopic compositions of carbonates and organic carbon from upper Proterozoic successions in Namibia: stratigraphic variation and the effects of diagenesis and metamorphism, Precambrian Research, v. 49, p. 301-327

Kim, S,T., Coplen, T.B., and Horita, J., 2015, Normalization of stable isotope data for carbonate minerals: Implementation of IUPAC guidelines, Geochimica et Cosmochimica Acta, v. 158, p. 276-289

Kronenberg, A.K., Yund, R.A., and Giletti, B.J., 1984, Carbon and oxygen diffusion in calcite: Effects of Mn content and P_{H2O}, Physics and Chemistry of Minerals, v.11, p. 101-112

Kroopnick, P., and Craig, H., 1972, Atmospheric oxygen: Isotopic composition and solubility fractionation, Science, v. 175, p. 54-55

McCrea, J.M., 1950, On the isotopic chemistry of carbonates and a paleotemperature scale, Journal of Chemical Physics, v. 18, n. 6, p. 849-857

Northrop, D.A., and Clayton, R.N., 1966, Oxygen-isotope fractionations in systems containing dolomite, The Journal of Geology, v. 74, p.174-196

O'Neil, J.R., and Epstein, S., 1966, Oxygen isotope fractionation in the system dolomite-calcite-carbon dioxide, Science, v. 152, p. 198-201

Selley, D., Broughton, D., Scott, R., Hitzman, M., Bull, S., Large, R., McGoldrick, P., Croaker, M., and Pollington, N., 2005, A new look at the geology of the Zambian Copperbelt, Economic Geology 100th Anniversary Volume, v. 29, p. 485-522

Schneider, J., Melcher, F., and Brauns, M., 2007, Concordant ages for the giant Kipushi base metal deposit (DR Congo) from direct Rb-Sr and Re-Os dating of sulfides, Mineralium Deposita, v. 42, p. 791-797

Sharma, T., and Clayton, R.N.,1965, Measurement of O^{18}/O^{16} ratios of total oxygen of carbonates, Geochimica et Cosmochimica Acta, v. 29, p. 1347-1353

Sillitoe, R, H., Perelló, J., and García, A., 2010, Sulphide-bearing veinlets throughout the stratiform mineralization of the Central African Copperbelt: Temporal and genetic implications, Economic Geology Express Letter, v. 105, p. 1361-1368

Taylor, H.P., 1968, The oxygen isotope geochemistry of igneous rocks, Contributions to Mineralogy and Petrology, v. 19, p. 1-71

Van Wilderode, J., Heijlen, W., De Muynck, D., Schneider, J., Vanhaecke, and Muchez, P., 2013, The Kipushi Cu-Zn deposit (DR Congo) and its host rocks: A petrographical, stable isotope (O, C) and radiogenic isotope (Sr, Nd) study, Journal of African Earth Sciences, v. 79, p. 143-156

Walraven, F., and Chabu, M., 1994, Pb-isotope constraints on base-metal mineralization at Kipushi (Southeastern Zäire), Journal of African Earth Sciences, v. 18, p. 73-82

Zheng, Y.F., 1999, Oxygen isotope fractionation in carbonate and sulfate minerals, Geochemical Journal, v. 33, p. 109-126

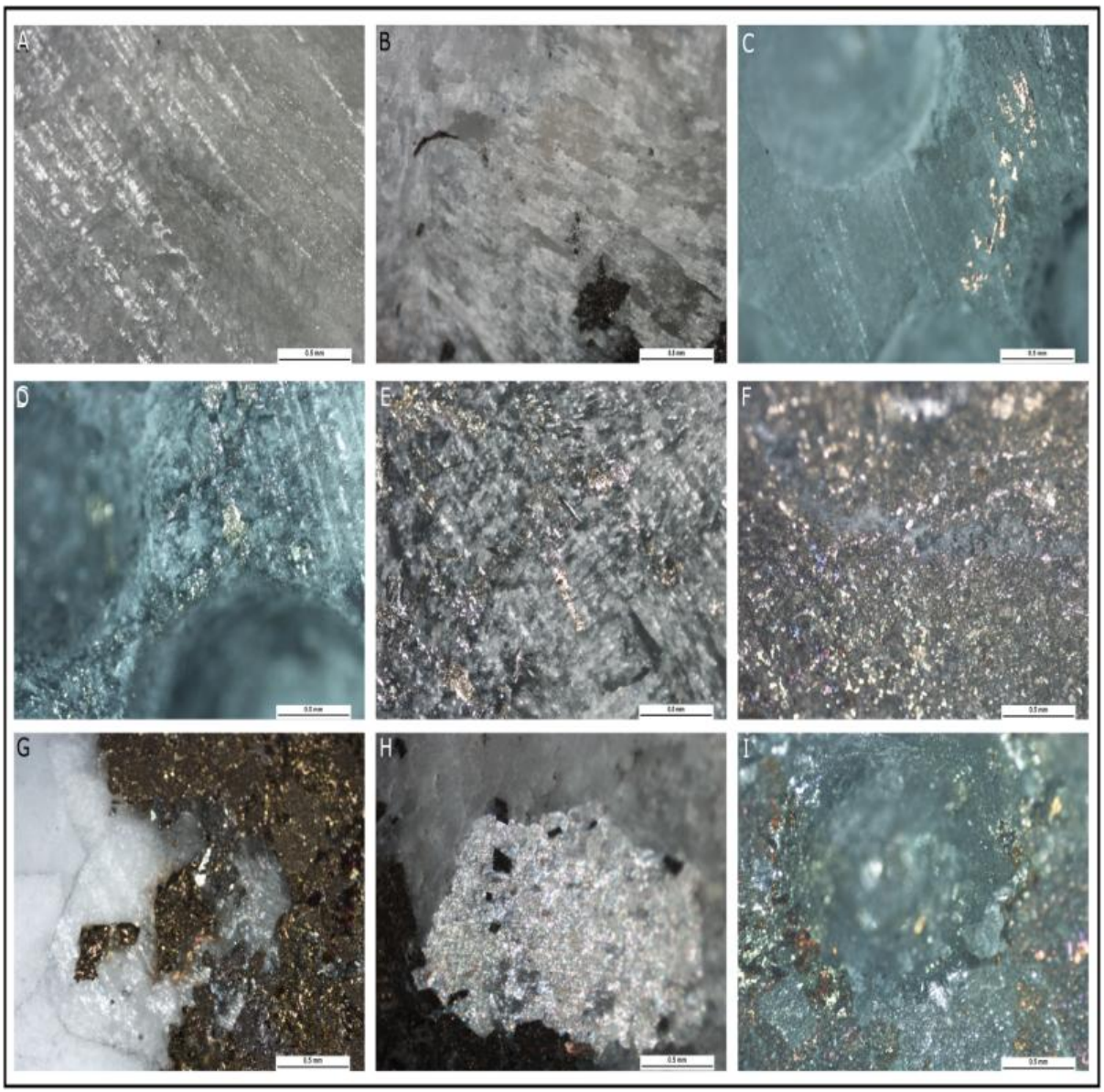

Figure 6.1: Photomicrographs of Kipushi hand samples. Each image at 50X under RL. **A)** KPU-081/557.3. Dolomite host rock of the Kakontwe Formation . **B)** Kipushi KPU-081/573.85 host rock displaying shistose texture. **C)** Kipushi KPU-081/557.3 host rock with sampling drill site locations. **D)** Kipushi KPU-081/557.3 syn-ore dolomite with drill site location. This dolomite can be seen in crosscutting relations with the host rock. **E)** Kipushi KPU-081/557.3 syn-ore dolomite with ore stage quartz (darker grey), sulphides are frequently lathe shaped-

especially arsenopyrite. **F)** Kipushi KPU-081/573.85 syn-ore dolomite. This carbonate is found cross-cutting sulphide. It precipitated throughout ore formation. **G)** Kipushi KPU-081/557.3 post-ore calcite replacing sulphide. Calcite is distinguished from dolomite due to its more vigorous reaction with HCL **H)** Kipushi KPU-081/573.85 post-ore calcite, note euhedral crystal penetrating into sulphide at bottom left. **I)** Kipushi KPU-081/573.85 post-ore calcite drill site location.

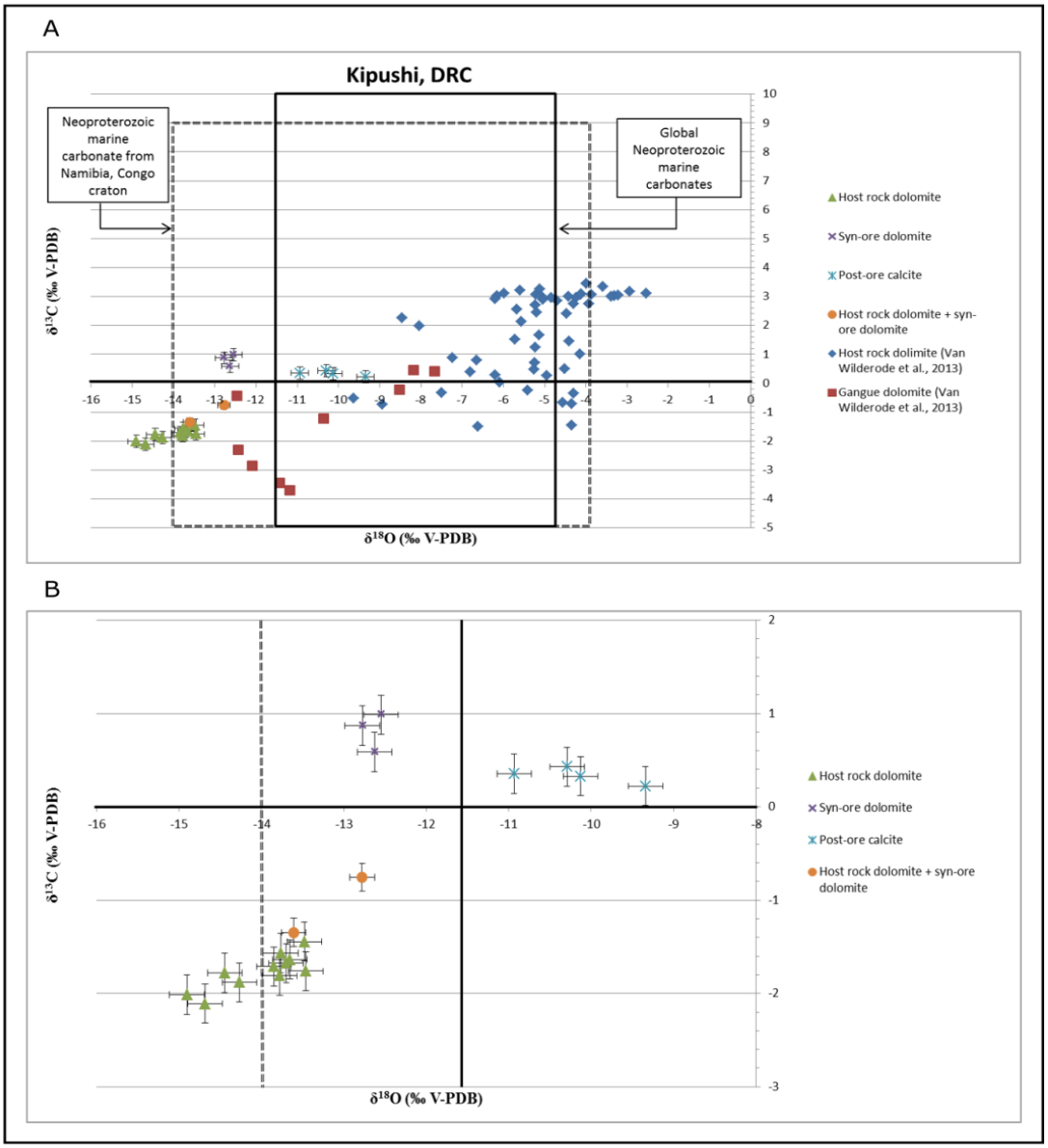

Figure 6.2. Carbon and oxygen isotopic IRMS results. The double-dashed line shows the range in $\delta^{13}C$ and $\delta^{18}O$ for marine carbonates from the Neoproterozoic Otavi Group, Namibia, Congo craton (Kaufman et al., 1991; Jacobsen and Kaufman, 1999). **A)** The heavy box denotes the carbon and oxygen range for Neoproterozoic marine carbonates (Jacobsen and Kaufman, 1999; Selley et al., 2005). The dashed line (also in **B**) denotes the carbon and oxygen range for marine carbonates from the Neoproterozoic Otavi Group, Namibia. This isotopic window

pertains to carbonates from the Congo Craton and is liklely a better representation of seawater in which the Kakontwe Formation was deposited. Included data taken from Van Wilderode et al. (2013) plot with higher $\delta^{13}C$ and $\delta^{18}O$ than the data from this study. **B)** Blanket 2σ instrumental error bars applied to newly data from this study.

Sample Name	Deposit	Dominant Phase	Paragenetic Context	$\delta^{13}C$ (VPDB) ‰	Calcite $\delta^{18}O$	
					(VPDB) ‰	(VSMOW) ‰
KPU-081/557.3Carb1-1	Kipushi	Dolomite	Host rock	-2.1		
KPU-081/557.3Carb1-1-rpt				-2.2		
Mean				**-2.1**		
KPU-081/557.3Carb1-2	Kipushi	Dolomite	Host rock	-1.6		
KPU-081/557.3Carb1-2-rpt				-1.6		
Mean				**-1.6**		
KPU-081/557.3Carb1-3	Kipushi	Dolomite	Host rock	-2.0		
KPU-081/557.3Carb1-4	Kipushi	Dolomite	Host rock	-1.9		
KPU-081/557.3Carb1-5	Kipushi	Dolomite	Host rock	-1.7		
KPU-081/557.3Carb1b-1	Kipushi	Dolomite	Host rock	-1.6		
KPU-081/557.3Carb1b-2	Kipushi	Dolomite	Host rock	-1.8		
KPU-081/557.3Carb1c-1	Kipushi	Dolomite	Host rock	-1.8		
KPU-081/557.3Carb1c-2	Kipushi	Dolomite	Host rock	-1.7		
KPU-081/557.3Carb1c-3	Kipushi	Dolomite	Host rock	-1.4		
KPU-081/557.3Carb1c-4	Kipushi	Dolomite	Host rock	-1.8		
KPU-081/573.85Carb4-1	Kipushi	Dolomite	Syn-ore	0.9		
KPU-081/573.85Carb4-1-rpt				0.9		
Mean				**0.9**		
KPU-081/573.85Carb4-2	Kipushi	Dolomite	Syn-ore	1.0		
KPU-081/573.85Carb4-2-rpt			Syn-ore+ Host rock	-0.8		
Mean				N/A		
KPU-081/573.85Carb4-3	Kipushi	Dolomite	Syn-ore	0.6		
KPU-081/573.85Carb4-3-rpt			Syn-ore+ Host rock	-1.3		
Mean				N/A		
KPU-081/573.85Carb2-1	Kipushi	Calcite	Post-ore	0.4	-10.3	20.1
KPU-081/573.85Carb3b-1	Kipushi	Calcite	Post-ore	0.4	-10.9	19.6
KPU-081/573.85Carb3c-1	Kipushi	Calcite	Post-ore	0.3	-10.1	20.5
KPU-081/573.85Carb3d-1	Kipushi	Calcite	Post-ore	0.2	-9.3	21.3

$\delta^{18}O$ Dolomite		$\delta^{13}C$ (2σ)	$\delta^{18}O$ (2σ)	Mass used (ug)	$\lvert D^{13}C \rvert$ (VPDB) ‰	$\lvert D^{18}O \rvert$ (VPDB) ‰
(VPDB) ‰	(VSMOW) ‰					
-14.5	16.0	0.28	0.25	482	0.1	0.4
-14.9	15.6	0.14	0.16	495		
-14.7	**15.8**	**0.21**	**0.21**			
-13.8	16.7	0.28	0.25	256	0.0	0.0
-13.8	16.7	0.14	0.16	320		
-13.8	**16.7**	**0.21**	**0.21**			
-14.9	15.6	0.28	0.25	291		
-14.3	16.2	0.28	0.25	241		
-13.8	16.6	0.14	0.16	367		
-13.7	16.8	0.14	0.16	401		
-13.8	16.7	0.14	0.16	403		
-13.5	17.0	0.14	0.16	523		
-13.7	16.8	0.14	0.16	461		
-13.5	17.0	0.14	0.16	427		
-14.4	16.0	0.14	0.16	418		
-12.9	17.6	0.28	0.25	251	0.0	0.2
-12.7	17.8	0.14	0.16	420		
-12.8	**17.7**	**0.21**	**0.21**			
-12.5	18.0	0.28	0.25	243	1.7	0.2
-12.8	17.7	0.14	0.16	423		
N/A	N/A	N/A	N/A			
-12.6	17.9	0.28	0.25	466	1.9	1.0
-13.6	16.9	0.14	0.16	502		
N/A	N/A	N/A	N/A			
		0.28	0.25	255		
		0.14	0.16	666		
		0.14	0.16	492		
		0.14	0.16	583		

Table 6.1: Phase corrected $\delta^{13}C$, and $\delta^{18}O$ IRMS results. For samples with repeats, no mean value is taken for those that exceed an absolute difference of 0.5 ‰ between both analyses.

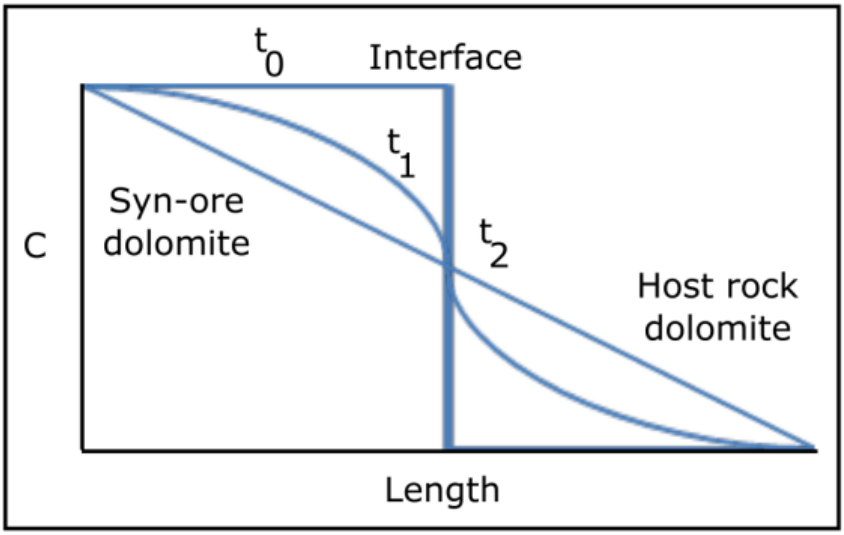

Figure 6.3: A typical two phase diffusion profile. At t_0 zero diffusion has occurred across the interface boundary between the syn-ore dolomite and the host rock dolomite. As t_n increases towards equilibrium, the concentration gradient between both endmembers becomes more gradual as $t \propto x$.

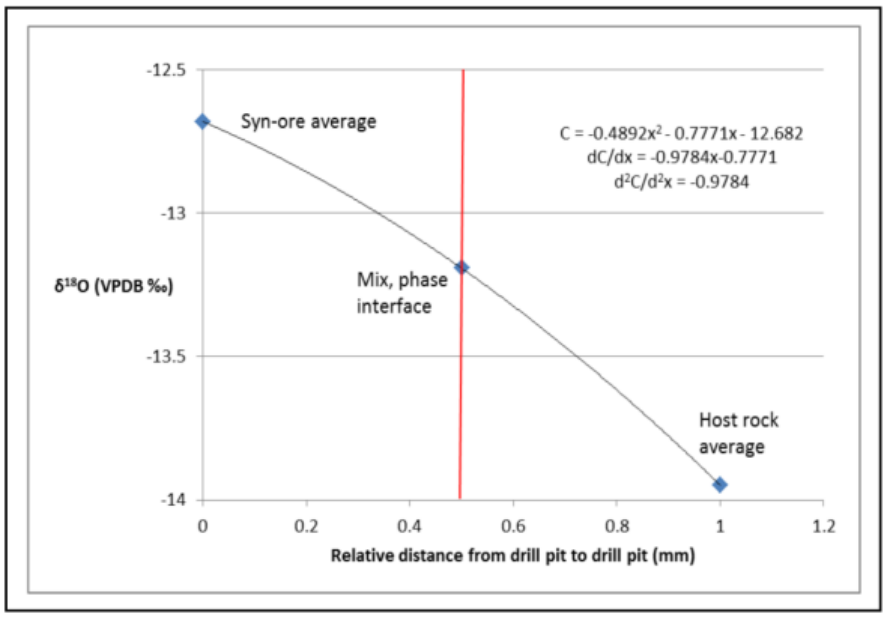

Figure 6.4: Measured $\delta^{18}O$ profile across syn-ore dolomite and host rock dolomite for a second-order polynomial. The line bisecting both endmembers at 0.5 mm is the interface at which oxygen diffusion occurs from the more highly concentrated syn-ore dolomite into the less concentrated host rock dolomite. When these two endmembers crystallize at t_0, they are in isotopic disequilibrium. This disequilibrium is maintined for all t_n until t_{EQ} in which both endmembers will be in isotopic equilibrium and the flux becomes zero across the interface.

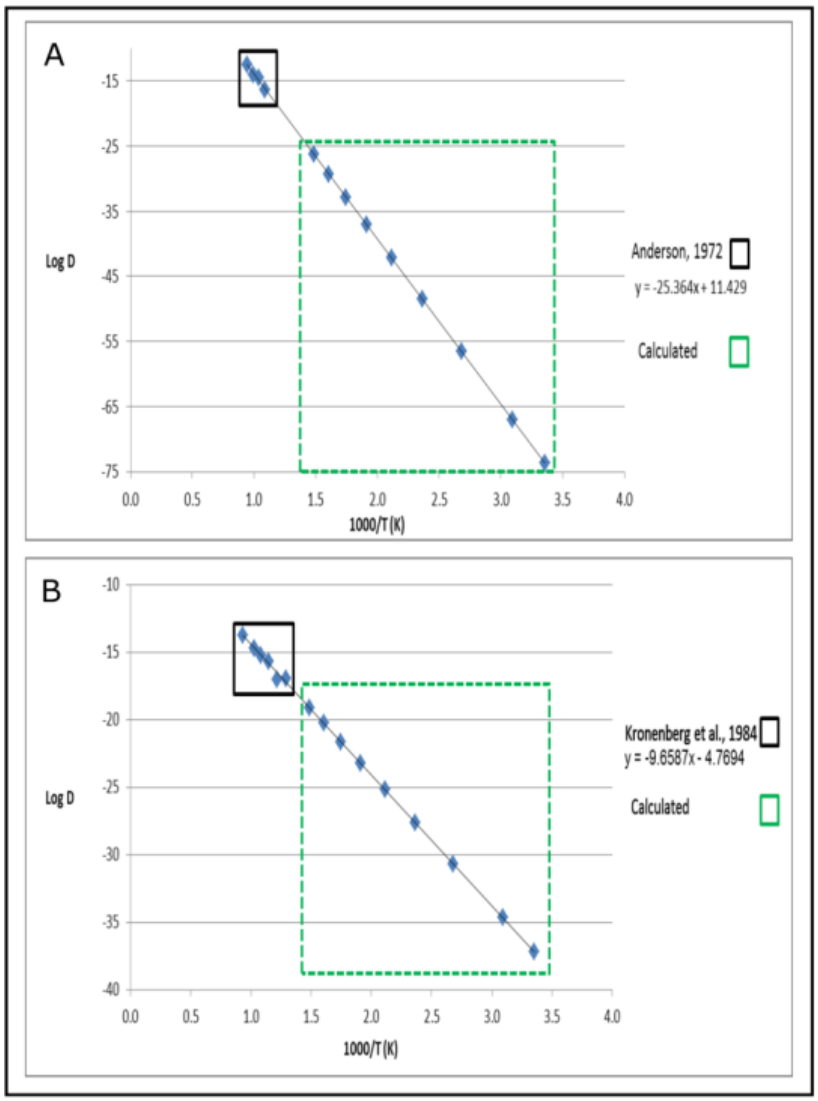

Figure 6.5: Diffusion rates for both dry dolomite and wet calcite. Data points in the upper right solid box are taken from experimental studies of oxygen diffusion in carbonate. A line of best fit was applied to these data and are extended to temperatures expected for Kipushi. **A)** Oxygen diffusion rates in dry dolomite from Anderson, 1972. **B)** Oxygen diffusion rates in wet calcite from Kronenberg et al., 1984.

Wet Calcite				
T (C)	T (K)	1000/T (K)	D (cm^2/sec)	LogD (cm^2/sec)
800	**1073**	**0.9**	**1.9E-14**	**-14**
700	**973**	**1.0**	**2.1E-15**	**-15**
650	**923**	**1.1**	**5.9E-16**	**-15**
600	**873**	**1.1**	**2.0E-16**	**-16**
550	**823**	**1.2**	**9.6E-18**	**-17**
500	**773**	**1.3**	**1.2E-17**	**-17**
450	723	1.4	7.5E-19	-18
400	673	1.5	7.6E-20	-19
350	623	1.6	5.4E-21	-20
300	573	1.7	2.4E-22	-22
250	523	1.9	5.9E-24	-23
200	473	2.1	6.6E-26	-25
150	423	2.4	2.5E-28	-28
100	373	2.7	2.2E-31	-31
50	323	3.1	2.2E-35	-35
Dry Dolomite				
T (C)	T (K)	1000/T (K)	D (cm^2/sec)	LogD (cm^2/sec)
785	**1058**	**0.9**	**3.E-13**	**-12**
735	**1008**	**1.0**	**1.E-14**	**-14**
690	**963**	**1.0**	**3.E-15**	**-15**
645	**918**	**1.1**	**4.E-17**	**-16**
400	673	1.5	6.E-27	-26
350	623	1.6	5.E-30	-29
300	573	1.7	1.E-33	-33
250	523	1.9	9.E-38	-37
200	473	2.1	7.E-43	-42
150	423	2.4	3.E-49	-49
100	373	2.7	3.E-57	-57
50	323	3.1	9.E-68	-67
25	298	3.4	2.E-74	-74
Simulated Wet Dolomite				
T (C)	T (K)	1000/T (K)	D (cm^2/sec)	LogD (cm^2/sec)
800	**1073**	**0.9**	**2E-12**	**-12**
700	**973**	**1.0**	**2E-13**	**-13**
650	**923**	**1.1**	**6E-14**	**-13**

600	**873**	**1.1**	**2E-14**	**-14**
550	**823**	**1.2**	**1E-15**	**-15**
500	**773**	**1.3**	**1E-15**	**-15**
450	723	1.4	7E-15	-16
400	673	1.5	8E-16	-17
350	623	1.6	5E-17	-18
300	573	1.7	2E-18	-20
250	523	1.9	6E-20	-21
200	473	2.1	7E-22	-23
150	423	2.4	3E-24	-26
100	373	2.7	2E-27	-29
50	323	3.1	2E-31	-33

Table 6.2: Experimentally determined (bold) and calculated oxygen diffusion rates for wet calcite (Kronenberg et al., 1984), and dry dolomite (Anderson, 1972) respectively at 50°C intervals. To best model conditions at Kipushi during ore formation, the diffusion rates of dry dolomite are multiplied by 10^2 to simulate wet dolomite.

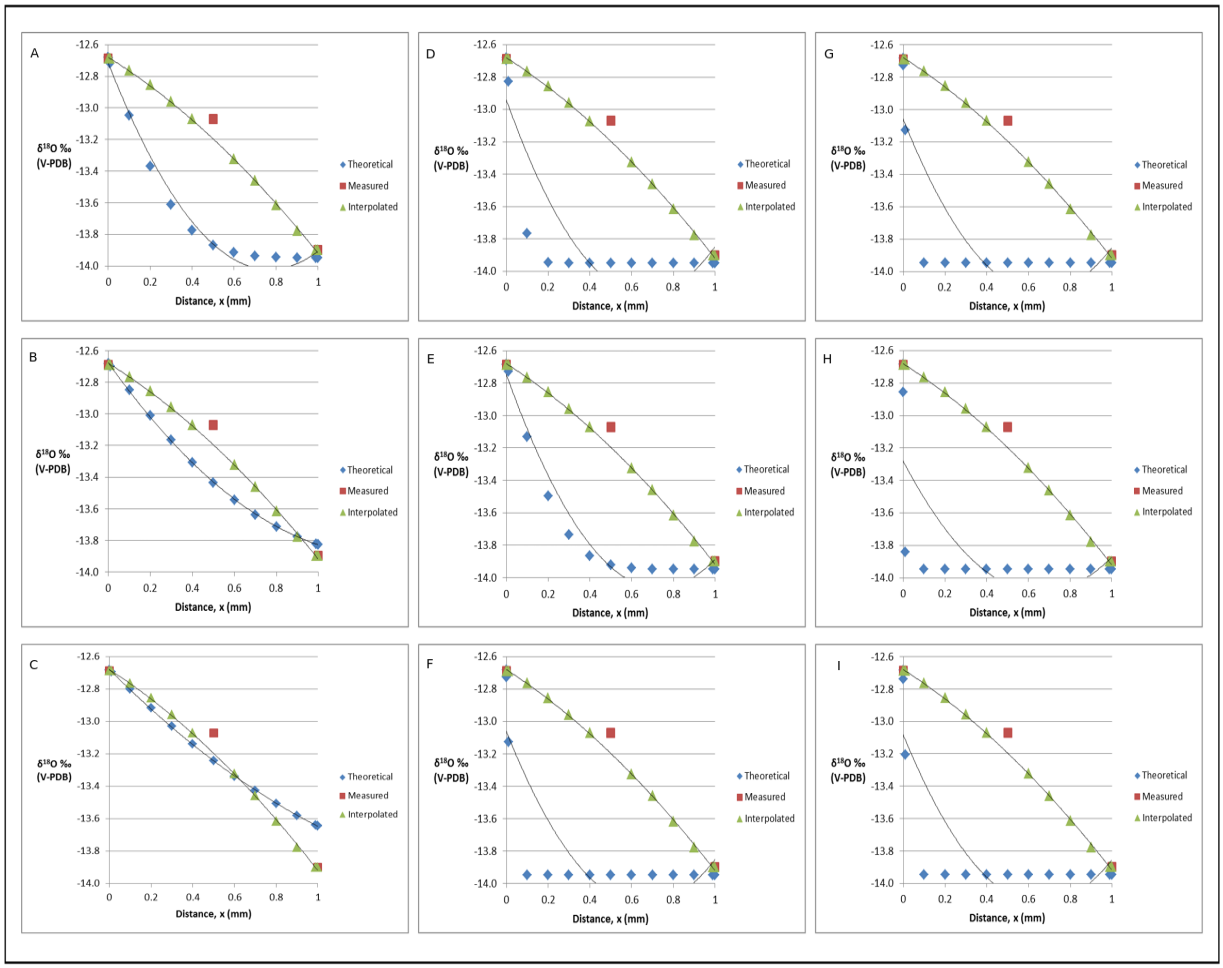

Figure 6.6: Theoretical oxygen diffusion profiles for wet calcite compared to the measured diffusion profile. Interpolated points are ponts intermittent of the three measured data points (syn-ore, syn-ore + host rock, and host rock). The $\delta^{18}O$ of the interpolated points were determined according to the line of best fit through the three measured data points. The C (concentration, or $\delta^{18}O$) in these theoretical profiles are produced for a variety of T, t, and x (temperature, time, and diffusion length (L) respectively) conditions. **A)** 500°C, 1 Ma. **B)** 500°C, 5 Ma. **C)** 500°C, 10 Ma. **D)** 450°C, 1 Ma. **E)** 450°C, 10 Ma. **F)** 400°C, 1 Ma. **G)** 400°C, 10 Ma. **H)** 350°C, 1 Ma. **I)** 350°C, 10 Ma.

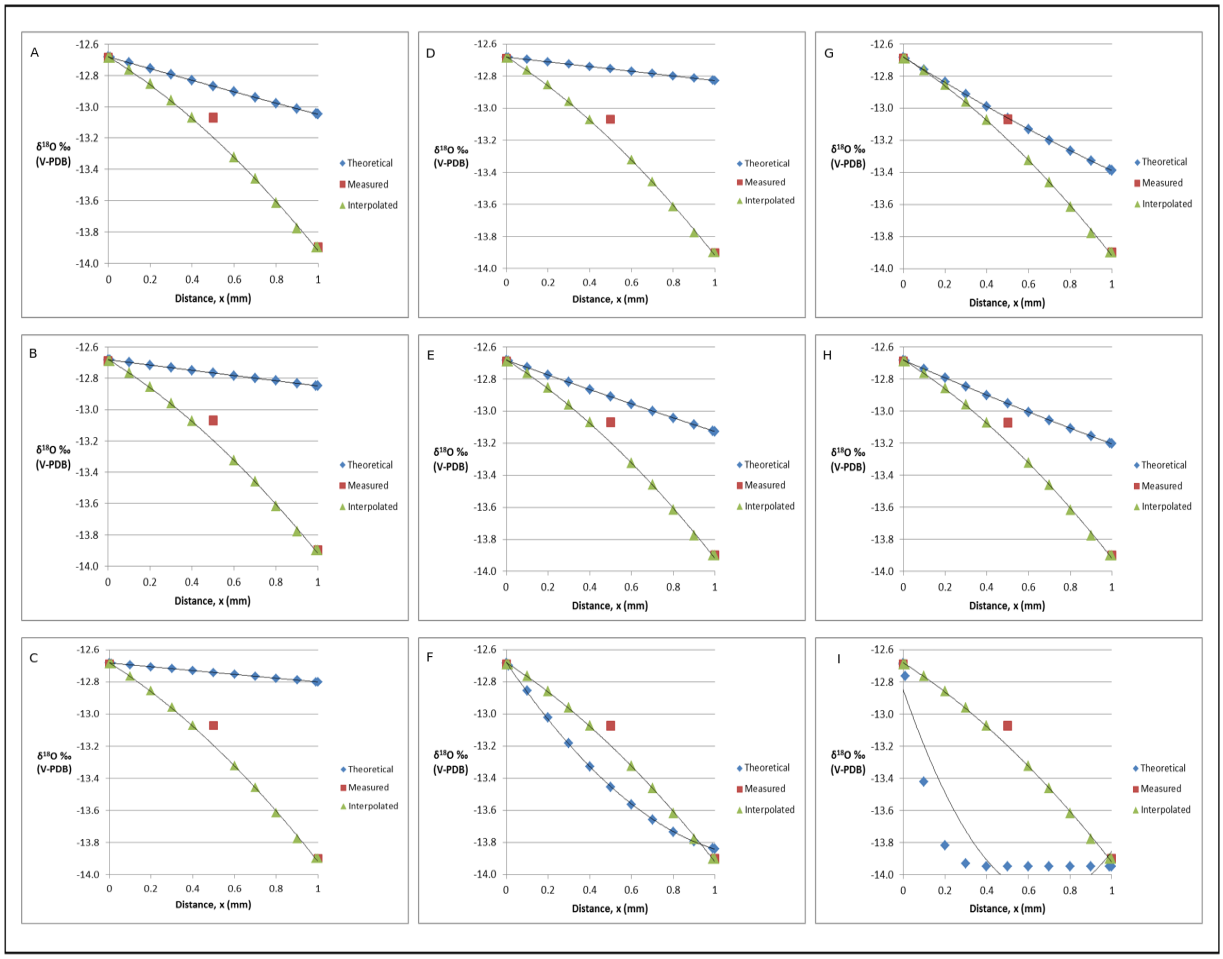

Figure 6.7: Theoretical oxygen diffusion profiles for simulated wet dolomite compared to the measured diffusion profile. Interpolated points, and the measured profile is the same as in Figure 6.6. The C (concentration, or $\delta^{18}O$) in these theoretical profiles are produced for a variety of T, t, and x (temperature, time, and diffusion length (L) respectively) conditions. **A)** 500°C for 1 Ma. **B)** 500°C for 5 Ma. **C)** 500°C for 10 Ma. **D)** 450°C for 1 Ma. **E)** 400°C for 1 Ma. **F)** 350°C for 1 Ma. **G)** 350°C for 5 Ma. **H)** 350°C for 10 Ma. **I)** 300°C for 1 Ma.

T (C)	1000ln(α) Dolomite-Calcite	Theoretical calcite $\delta^{18}O$ ‰ (V-SMOW)
250	1.9	15.9
275	1.7	16.1
300	1.6	16.2
325	1.5	16.3
350	1.4	16.4
375	1.3	16.5
400	1.2	16.6
425	1.1	16.7
450	1.0	16.8
475	1.0	16.8
500	0.9	16.9
525	0.9	16.9
550	0.8	17.0
575	0.8	17.0
600	0.7	17.1
Measured calcite $\delta^{18}O$ = 20.4 ‰ (V-SMOW)		

Table 6.3: Theoretical $\delta^{18}O$ post-ore calcite calculated over a temperature range of 250-600°C if in isotopic equilibrium with dolomite. For the provided temperatures, the measured calcite ($\delta^{18}O$ of 20.4 ‰) is not in isotopic equilibrium, and cannot have been sourced from the same fluid. The dolomite-calcite fractionation factor used in calculations is from Chacko and Deines (2008).

	Calcite-H_2O		Dolomite-H_2O		
T (C)	**$1000\ln(\alpha)_{Calcite-H2O}$ Calcite = A_1, H_2O = B_1**	**$\delta^{18}O_{B1}$ ‰ (V-SMOW)**	**$1000\ln(\alpha)_{Dolomite-H2O}$ Dolomite = A_2, H_2O = B_2**	**$\delta^{18}O_{B2}$ ‰ (V-SMOW)**	**$\delta^{18}O_{(B1-B2)}$ ‰ (V-SMOW)**
100	12.7	7.3	18.4	1.5	5.9
125	10.9	9.2	15.6	4.3	4.8
150	9.5	10.6	13.4	6.6	4.0
175	8.2	12.0	11.5	8.6	3.4
200	7.2	13.0	10.0	10.1	2.9
225	6.3	13.9	8.7	11.5	2.5
250	5.6	14.7	7.7	12.5	2.2
275	4.9	15.4	6.7	13.5	1.9
300	4.3	16.0	6.0	14.2	1.8
325	3.8	16.5	5.3	15.0	1.5
350	3.4	16.9	4.7	15.6	1.3
375	3.0	17.3	4.2	16.1	1.2
400	2.7	17.6	3.8	16.5	1.1
425	2.4	18.0	3.4	16.9	1.0
450	2.1	18.3	3.0	17.3	0.9
475	1.8	18.6	2.7	17.6	0.9
500	1.6	18.8	2.5	17.9	0.9
525	1.4	19.0	2.3	18.1	0.9
550	1.2	19.2	2.1	18.3	0.9
575	1.0	19.4	1.9	18.5	0.9
600	0.9	19.5	1.7	18.7	0.8

Table 6.4: Calculated $\delta^{18}O$ fluid values for both calcite-fluid, and dolomite-fluid systems. Differences of at least 0.9 ‰ V-SMOW would occur between the fluids in these two systems (with an increase in fractionation between the fluids as T decreases), evidence of isotopic disequilibria. That is, the post-ore calcite, and syn-ore dolomite are from two separate fluids B_1 and B_2), and the measured oxygen values are not simply the result from temperature evolution. The oxygen isotopic fractionation factors are from Hu and Clayton (2003) and Zheng (1999) for the calcite-H_2O, and dolomite-H_2O systems respectively.

7) Synthesis and Summary

7.1 Future Development & Improvement

Improving the purity of a mineral separate may reveal better geochronological results. One promising methodology is to disaggregate minerals using high voltage (Giese et al., 2007). Traditionally grains are mechanically fractured, meaning that a single grain is often composed of more than one phase. This new method separates a bulk sample is along the constituent mineral grains' cleavage planes, resulting in monomineralic grains. Unless a sample is pure, it is, to some degree a bulk analysis.

Determination of suitable geochronometers for Re-Os analysis can also improve future results. While some minerals may have potential, there is also considerable variability in their precision (ex: bornite). Recent developments have shown that Cu-Co ore may be successfully directly dated using carrolite (Saintilan et al., 2018). Evaluating the closure temperature, and solubility of sulphide minerals are specific examples of future possible research.

7.2 Final Conclusions

Preenrichment of Pb into the Grand Conglomerate may have occurred due to the Sturtian ice sheet scoured the 2.0 Ga U-rich basement rock. Radiogenic Pb is also found in the detrital (pre-ore grains) at Chibuluma West. Radiogenic Pb likely is the cause for apparent diagenetic ages, and must be considered for meaningful interpretations of the common Pb data.

A Lufilian timing and crustal metal source is found for the bulk of ore mineralization. Ore-stage pyrite from Chibuluma West which must be coeval with the hydrothermal gangue, yielded an isochron timing of ~536 Ma, and is in close agreement with the ore-stage pyrite isochron age of ~537 Ma. A Pb-Pb isochron age of ~552 Ma obtained from ore-stage pyrite independently confirms the Re-Os age results. Sulphide and hydrothermal gangue contains

radiogenic Pb derived from detrital grains (zircon) and produces apparent >600 Ma ages. There is no evidence of a magmatic or pre-Lufilian timing of ore formation. At the unmetamorphosed Kamoa deposit, Pb-Pb model ages of stratiform pyrite yielded late-stage/cooling Lufilian ages (~510-480 Ma). There is no difference between core and rim (leachate) Pb-Pb model ages from Kamoa pyrite, and suggests a single event of Pb mineralization. A sub-population of ore-stage pyrites yield ~460 Ma Re-Os model ages, and are within error of the Pb-Pb model ages. Diagenetic Re-Os ages are not feasible for Kamoa, even if a CHUR Os_i is used. Thus, the Lufilian timing must represent the true age of the primary sulphide mineralization at Kamoa, since the ores are solely stratiform.

The Kipushi deposit formed after the Lufilian orogeny ended, possibly resultant from an post-Lufilian extension-related event (Schneider et al., 2007), probably an intrusion (Haset and Muchez, 2011). Common lead model ages are varied and discontinuous-suggestive of open system behaviour or more than one fluid pulse. In either case, all common ore-stage lead model ages are constrained between 478 Ma to 387 Ma. A novel approach in which estimates for both temperature and length of mineralization has been applied to syn-ore dolomite from Kipushi. Oxygen diffusion has shown that the one pulse of ore fluid at Kipushi ranged from 350-500° C. This temperature determination is in good agreement to geothermometry data collected from traditional methods. This estimate is independently supported by temperature estimates determined from petrographic analysis of carbonate twins (T > 200° C). The shear strain of these syn-ore dolomite supports a tectonic environment with a greater stress regime than that for the calcite, providing further evidence for a Lufilian timing of ore emplacement. The time of length of mineralization at Kipushi is also placed at ~10 Ma. These temperatures and mineralization time length estimates pertain only to a single stage of ore formation (as there may be more than

one pulse of fluid); however, they may be reasonable conditions for other CAC deposits similar to Kipushi, like Chibuluma West. Finally, the ore-stage fluid was likely affected by an igneous source, although constraining all fluid to a single source reservoir is not possible.

A fourth and final stage of mineralization occurred in the Permian. Molybdenite is found in veins that cross-cut pre-existing ore and infilling fractures. A pyrite Re-Os isochron age of 282 Ma from Kamoa, is supported by a pyrite and arsenopyrite Re-Os isochron age of 327 Ma, and a within-error radiogenic Os (ignoring initial Os) age of 290 Ma from Kipushi. Additionally, both core and rim (leachate) Pb-Pb ages from sulphide and gangue minerals at Kipushi are (428-390 Ma), and (338-294 Ma) respectively. Oxygen isotope equilibration calculations prove that a separate carbonate generation precipitated after the Lufilian-aged, syn-ore carbonate at Kipushi. This post-ore calcite generation is very likely also coeval with the molybdenite found by EPMA and LAICPMS in the late forming fractures and cross-cutting veins. Shear strain calculations in post-ore calcite confirm these findings, as the stress which produced the measured strain in the calcite is lower than that of the syn-ore, Lufilian dolomite. A supergene enrichment is known for both Kamoa and Kipushi deposits. These Re-Os, Pb-Pb, O, shear strain, and petrographic (limonite and native copper) lines of evidence prove that a regional (likely atmospheric O_2-rich) fluid containing Mo and Pb existed in the Nguba Group during the Late Paleozoic. The supergene fluid was most likely generated by a collisional event at the southern margin of the Gondwana in the Late Paleozoic.

The realization that it is sub-micron sized molybdenite inclusions, not pyrite or arsenopyrite which is providing most if not all of the Re and thus radiogenic Os in an age highlights the need to interpret Re-Os ages with care. The molybdenite may in fact be the entire

source of the geochronological age. Preliminary imaging provides evidence for or against the existence of molybdenite in a sample.

7.3 References

Giese, J., Seward, D., Gnos, E., and Kurz, D., 2007, Comparative apatite fission track study of conventionally versus selFrag Lab fragmented samples, Goldschmidt Conference Abstracts, Geochimica et Cosmochimica Acta, v. 71, Supplement, p. A302-A366

Haest, M., and Muchez, P., 2011, Stratiform and vein-type deposits in the Pan-African orogen in central and southern Africa: Evidence for multiphase mineralization, Geologica Belgica, v. 14, p. 23-44

Saintilan, N.J., Selby, D., Creaser, R.A., and Dewaele, S., 2018, Sulphide Re-Os geochronology links orogenesis, salt and Cu-Co ores in the Central African Copperbelt, Nature Scientific Reports, v. 8, p. 1-8

References

Albarede, F., and Juteau, M., 1984, Unscrambling the lead model ages, Geochimica et Cosmochimica Acta, v. 48, p. 207-212

Allégre, C.J., and Luck, J.M., 1980, Osmium isotopes as petrogenetic and geological tracers, Earth and Planetary Science Letters, v. 48, p. 148-154

Anderson, T.F., 1972, Self-diffusion of carbon and oxygen in dolomite, Journal of Geophysical Research, v. 77, p. 857-861

Annels, A.E., Vaughn, D.J., and Craig, J.R., 1983, Conditions of ore mineral formation in certain Zambian Copperbelt deposits with special reference to the role of cobalt, Mineralium Deposita, v. 18, p. 71-88

Armstrong, R.A., Master, S., and Robb, L.J., 2005, Geochronology of the Nchanga Granite, and constraints on the maximum age of the Katanga Supergroup, Zambian Copperbelt, Journal of African Earth Sciences, v. 42, p. 32-40

Barra, F., Broughton, D., Ruiz, J., and Hitzman, M., 2004, Multi-stage mineralization in the Zambian Copperbelt based on Re-Os isotope constraints, Geological Society of America Abstracts with Programs, v. 36, n. 5., p. 516

Batumike, M.J., Cailteux, J.L.H., Kampunzu, A.B., 2007, Lithostratigraphy, basin development, base metal deposits, and regional correlations of the Neoproterozoic Nguba and Kundelungu rock successions, central African Copperbelt, Gondwana Research, v. 11, p. 432-447

Begley, I.S., and Sharp, B.L., 1997, Characterization and correction of instrumental bias in inductively coupled plasma quadrupole mass spectrometry for accurate measurement of lead isotope ratios, Journal of Analytical Atomic Spectrometry, v. 12, p. 395-402

Binda, P.L., and Mulgrew, J.R., 1974, Stratigraphy of copper occurrences in the Zambian copperbelt, *In:* Bartholomé, P (Ed), Gisements Stratiformes et Provinces Cupriféres. Soc. Géol., Liège, Belgique, p. 215-233

Birck, J.L., Roy-Barman, M., and Capmas, F., 1997, Re-Os isotopic measurements at the femtomole level in natural samples, Geostandards Newsletter, v. 20, n.1, p. 19-27

Box, S.E., Syusyura, B., Seltmann, R., Creaser, R.A., Dolgopolova, A., and Zeintek, M.L., 2012, Dzhezkazgan and associated sandstone copper deposits of the Chu-Sarysu Basin, Central Kazakhstan, Economic Geology, Special Publication 16, p. 303-328

Broughton, D., and Rogers, R., 2010, Discovery of the Kamoa copper district, Central Africa Copperbelt, DRC, Society of Economic Geologists Special Publication 15, v. 1, p. 287-298

Brown, A.C., 1997, World-class sediment-hosted stratiform copper deposits: Characetistics, genetic concepts and metallotects, Australian Journal of Earth Sciences, v. 44, p. 317-328

Brown, A.C., and Bartholomé, P., 1972, Inhomogeneities in cobaltiferous pyrite from the Chibuluma Cu-Co deposit, Zambia, Mineralium Deposita, v. 7, p. 100-105

Cailteux, J., 1994, Lithostratigraphy of the Neoproterozoic Shaba-type (Zaire) Roan Supergroup and metallogenesis of associated stratiform mineralization, Journal of African Earth Sciences, v. 19, p. 279-301

Cailteux, J., Binda, P.L., Katekesha, W.M., Kampunzu, A.B., Intiomale, M.M., Kapenda, D., Kaunda, C., Ngongo, K., Tshiauka, T., and Wendorff, M., 1994, Lithostratigraphical correlation of the Neoproterozoic Roan Supergroup from Shaba (Zaire) and Zambia, in the central African copper-cobalt metallogenic province, Journal of African Earth Sciences, v. 19, n. 4., p. 265-278

Cailteux, J.L.H., Kampunzu, A.B., Lerouge, C., Kaputo, A.K., and Milesi, J.P., 2005, Genesis of sediment-hosted stratiform copper-cobalt deposits, central African Copperbelt, Journal of African Earth Sciences, v. 42, p. 134-158

Campbell, A.R., and Larson, P.B., 1998, Introduction to stable isotope applications in hydrothermal systems, *In:* Richards, J.P., and Larson, P.B., (Eds), Techniques in Hydrothermal Ore Deposits Geology, Reviews in Economic Geology, v. 10, Society of Economic Geologists, Littleton, USA

Chabu, M., 1995, The geochemistry of phlogopite and chlorite from the Kipushi Zn-Pb-Cu deposit, Shaba, Zaire, The Canadian Mineralogist, v. 33, p. 547-558

Chacko, T., Deines, P., 2008, Theoretical calculation of oxygen isotope fractionation factors in carbonate systems, Geochimica et Cosmochimica Acta, v. 72, p. 3642-3660

Coplen, T.B., Kendall, C., and Hopple, J., 1983, Comparison of stable isotope reference samples, Nature, v. 302, p. 236-238

Cosi, M., De Bonis, A., Gosso, G., Hunziker, J., Martinotti, G., Moratto, S., Robert, J.P., and Ruhlman, F., 1992, Late Proterozoic thrust tectonics, high-pressure metamorphism and uranium mineralization in the Domes Area, Lufilian Arc, northwestern Zambia, Precambrian Research, v. 58, p. 215-240

Crank, J., 1956, The Mathematics of Diffusion, Oxford University Press, London, p. 414

Creaser, R.A., Papanastassiou, D.A., and Wasserburg, G.J., 1991, Negative thermal ion mass spectrometry of osmium, rhenium, and iridium, Geochimica et Cosmochimica Acta, v. 55, p. 397-401

Creaser, R.A., Sannigrahi, P., Chacko, T., and Selby, D., 2002, Further evaluation of the Re-Os geochronometer in organic-rich sedimentary rocks: a test of hydrocarbon maturation effects in the Exshaw Formation, Western Canada Sedimentary Basin, Geochimica et Cosmochimica Acta, v. 66, i. 19, p. 3441-3452

Creaser, R.A., 2015, Crustal sulfide minerals (Re-Os), *In:* Rink, W.J., Thompson, J.W., (Eds); Heaman, L.M., Jull, A.J. Timothy, Paces, J.B. (Ass. Eds). Encyclopedia of Scientific Dating Methods, Springer, Dordrecht, Netherlands

Cumming, G.L., and Richards, J.R., 1975, Ore lead isotope ratios in a continuously changing Earth, Earth and Planetary Science Letters, v. 28, p. 155-171

Daly, M.C., Lawrence, S.R., Diemu-Tshiband, K., and Matouana, B., 1992, Tectonic evolution of the Cuvette Centrale, Zaire, Journal of the Geological Society, London, v. 149, p. 539-546

De Magnée, I., and Francois, A., 1988, The origin of the Kipushi (Cu, Zn, Pb) deposit in direct relation with a Proterozoic salt diaper, Copperbelt of Central Africa, Shaba, Republic of Zaire, *In:* Friedrich, G.H., and Herzig, P.M., (Eds), Base Metal sulfide Deposits, Springer-Verlag, Berlin, Germany

Dewaele, S., Muchez, P., Vets, J., Fernandez-Alonzo, M., and Tack, L., 2006, Multiphase origin of the Cu-Co ore deposits in the western part of the Lufilian fold-and-thrust belt, Katanga (Democratic Republic of Congo), Journal of African Earth Sciences, v. 46, p. 455-469

Dickin, A.P., 1995, Radiogenic Isotope Geology, Cambridge University Press, UK

Dodson, M.H., 1979, Theory of cooling ages, *In:* Jäger, E., and Hunziker, J.C., (Eds), Lectures in Isotope Geology, Springer-Verlag, Berlin, Germany

El Desouky, H.A., Muchez, P., Boyce, A.J., Schneider, J., Cailteux, J.L.H., Dewaele, S., and Von Quadt, A., 2010, Genesis of sediment-hosted stratiform copper-cobalt mineralization at Luiswishi and Kamoto, Katanga Copperbelt (Democratic Republic of Congo), Mineralium Deposita, v. 45, p. 735-763

Fairbairn, H.W., and Hawkes, H.E., JR, 1941, Dolomite orientation in deformed rocks, American Journal of Science, v. 239, p. 617-632

Faure, G., and Mensing, T.M., 2005, Isotopes: Principles and Applications, Wiley, Hoboken, USA

Ferrill, D.A., Morris, A.P., Evans, M.A., Burkhard, M., Groshong, R.H., JR, and Onasch, C.M., 2004, Calcite twin morphology: A low-temperature deformation geothermometer, Journal of Structural Geology, v. 26, p. 1521-1529

Flinter, B.H., 1959, The magnetic separation of some alluvial minerals in Malaya, American Mineralogist, v. 44, p. 738-751

Fricke, H.C., and O'Neill, J.R., 1999, The correlation between $^{18}O/^{16}O$ ratios of meteoric water and surface temperature: its use in investigating terrestrial climate change over time, Earth and Planetary Science Letters, v. 170, p. 181-196

Frimmel., H.E., Jonasson, I.R., and Mubita, P., 2004, An Eburnean base metal source for sediment-hosted zinc-lead deposits in Neoproterozoic units of Namibia: Lead isotopic and geochemical evidence, Mineralium Deposita, v. 39, p. 328-343

Giese, J., Seward, D., Gnos, E., and Kurz, D., 2007, Comparative apatite fission track study of conventionally versus selFrag Lab fragmented samples, Goldschmidt Conference Abstracts, Geochimica et Cosmochimica Acta, v. 71, Supplement, p. A302-A366

Goldstein, J.I., Newbury, D.E., Joy, D.C., Lyman, C.E., Echlin, P., Lifshin, E., Sawyer, L., and Michael, J.R., 2003, Scanning Electron Microscopy and X-Ray Microanalysis, Kluwer Academic/Plenum Publishers, New York, USA, p. 673

Groshong, R.H., JR, 1972, Strain calculated from twinning in calcite, Geological Society of America Bulletin, v. 83, p. 2025-2038

Guiraud, R., Bosworth, W., Thierry, J., and Delplanque, A., 2005, Phanerozoic geological evolution of Northern and Central Africa: An overview, Journal of African Earth Sciences, v. 43, p. 83-143

Haest, M., and Muchez, P., 2011, Stratiform and vein-type deposits in the Pan-African orogen in central and southern Africa: Evidence for multiphase mineralization, Geologica Belgica, v. 14, p. 23-44

Hayes, T.S., 1990, A preliminary study of thermometry and metal sources of the Spar Lake strata-bound copper-silver deposit, Belt Supergroup, Montana, United States Geological Survey Open-File Report 90-0484, p. 1-30

Heijlen, W., Banks, D.A., Muchez, P. Stensgard, B.M., and Yardley, B.W.D., 2008, The nature of the mineralizing fluids of the Kipushi Zn-Cu deposit, Katanga, Democratic Republic of Congo: Quantitative fluid inclusion analysis using laser ablation ICP-MS and bulk crush-leach methods, Economic Geology, v. 103, p. 1459-1482

Hitzman, M.W., Broughton, D., Selley, D., Woodhead, J., Wood, D., and Bull, S., 2012, The Central African Copperbelt: Diverse stratigraphic, structural, and temporal settings in the world's largest sedimentary copper district, Society of Economic Geologists, Special Publication 16, p. 487-514

Hitzman, M.W., Kirkham, R., Broughton, D., Thorson, J., and Selley, D., 2005, The sediment-hosted stratiform copper ore system, *In:* Hedenquist, J.W., Thompson, J.F.H., Goldfarb, R.J., and Richards, J.P., (Eds), Economic Geology One Hundredth Anniversary Volume 1905-2005, Society of Economic Geologists, Littleton, USA

Hitzman, M.W., Selley, D., and Bull, S., 2010, Formation of sedimentary copper deposits through Earth history, Economic Geology, v. 105, p. 627-639

Hu, G., and Clayton, R.N., 2003, Oxygen isotope salt effects at high pressure and high temperature and the calibration of oxygen isotope geothermometers, Geochimica et Cosmochimica Acta, v. 67, p. 3227-3246

Hume-Rothery, W., 1966, The Structure of Alloys or Iron: An Elementary Introduction, Pergamon Press, p. 347

Intiomale M, Oosterbosch R (1974) Géologie et Géochemie du gisement de Kipushi Zaire, *In:* Bartholomé, P., (Ed), Gisements stratiformes et provinces cupriféres, Centenaire Société Géologique Belgique, Liége, p 123-164

Jackson, M.P.A., Warin, O.N., Woad, G.M., and Hudec, M.R., 2003, Neoproterozoic allochthonous salt tectonics during the Lufilian orogeny in the Katangan Copperbelt, central Africa, Geological Society of America Bulletin, v. 115, p. 314-320

Jacobsen, S.B., and Kaufman, A.J., 1999, The Sr, C and O isotopic evolution of Neoproterozoic seawater, Chemical Geology, v. 161, p. 37-57

Jaffey, A.H., Flynn, K.F., Glendenin, L.E., Bentley, W.C., and Essling, A.N., 1971, Precision measurement of half-lives and specific activities of ^{235}U and ^{238}U, Physical Review C, v. 4, p. 1889-1906

John, T., Schenk, V., Mezger, K., and Tembo, F., 2004, Timing and PT evolution of whiteschist metamorphism in the Lufilian Arc-Zambezi belt orogen (Zambia): Implications for the assembly of Gondwana, The Journal of Geology, v.112, p. 71-90

Kamona, A.F., Lévêque, J., Friedrich, G., and Haack, U., 1999, Lead isotopes of the carbonate-hosted Kabwe, Tsumeb, and Kipushi Pb-Zn-Cu sulfide deposits in relation to Pan African orogenesis in the Damaran-Lufilian fold belt of Central Africa, Mineralium Deposita, v. 34, p. 273-283

Kampunzu, A.B., and Cailteux, J., 1999, Tectonic evolution of the Lufilian Arc (Central Africa Copper Belt) during Neoproterozoic Pan African orogenesis, Gondwana Research, v. 2, p. 401-421

Kampunzu, A.B., Cailteux, J.L.H., Kamona, A.F., Intiomale, M.M., and Melcher, F., 2009, Sediment-hosted Zn-Pb-Cu deposits in the Central African Copperbelt, Ore Geology Reviews, v. 35, p. 263-297

Kaufman, A.J., Hayes, J.M., Knoll, A.H., and Germs, G.J.B., 1991, Isotopic compositions of carbonates and organic carbon from upper Proterozoic successions in Namibia: stratigraphic variation and the effects of diagenesis and metamorphism, Precambrian Research, v. 49, p. 301-327

Kaufman, A.J., Hayes, J.M., Knoll, A.H., and Germs, G.J.B., 1991, Isotopic compositions of carbonates and organic carbon from upper Proterozoic successions in Namibia:

stratigraphic variation and the effects of diagenesis and metamorphism, Precambrian Research, v. 49, p. 301-327

Kim, S,T., Coplen, T.B., and Horita, J., 2015, Normalization of stable isotope data for carbonate minerals: Implementation of IUPAC guidelines, Geochimica et Cosmochimica Acta, v. 158, p. 276-289

Köppel, V., and Grünenfelder, M., 1979, Isotope geochemistry of lead, *In:* Jäger, E., and Hunziker, J.C. (Eds), Lectures in Isotope Geology, Springer, Berlin, Germany

Kronenberg, A.K., Yund, R.A., and Giletti, B.J., 1984, Carbon and oxygen diffusion in calcite: Effects of Mn content and P_{H2O}, Physics and Chemistry of Minerals, v.11, p. 101-112

Kroopnick, P., and Craig, H., 1972, Atmospheric oxygen: Isotopic composition and solubility fractionation, Science, v. 175, p. 54-55

Kullerud, L., 1991, On the calculation of isochrons, Chemical Geology, v. 87, p. 115-124

Kuo, K. K., and Acharya, R., 2012, Appendix D: Particle Size–U.S. Sieve Size and Tyler Screen Mesh Equivalents, in Applications of Turbulent and Multiphase Combustion, John Wiley & Sons, Inc., Hoboken, NJ, USA

LeRoux, L.J., and Glendenin, L.E., 1963, Half-life of thorium-232, Proc. Natl. Conf. on Nuclear Energy, Pretoria, p. 83-94

Levasseur, Birck, and Allégre, 1999, Osmium isotopic composition of corals: Evidences for multiple sources, Geochimica et Cosmochimica Acta, v. 63, p. 1335-1345

Lhoest, J.J., 1995, The Kipushi mine, Mineralogical Record, v. 26, p. 163-192

Ludwig, K.R., 2003, Isoplot/Ex version 3.76, A geochronological toolkit for Microsoft Excel, Berkeley Geochron Canter Special Publication, v. 4, p. 1-43

Makishima, A., Nakanishi, M., and Nakamura, E., 2001, A group separation method for Ruthenium, Palladium, Rhenium, Osmium, Iridium, and Platinum using their bromo complexes and an anion exchange resin, Analytical Chemistry, v. 73, p. 5240-5246

Manton, W.I., 1988, Separation of Pb from young zircons by single-bead ion exchange, Chemical Geology, v. 73, p. 147-152

McCrea, J.M., 1950, On the isotopic chemistry of carbonates and a paleotemperature scale, Journal of Chemical Physics, v. 18, n. 6, p. 849-857

Morgan, J.W., Golightly, D.W., and A.F., Dorrzapf, 1991, Methods for the separation of rhenium, osmium and molybdenum applicable to isotope geochemistry, Talanta, v. 38, p. 259-265

Morelli, R.M., Creaser, R.A., Selby, D., Kontak, D.J., and Horne, R.J., 2005, Rhenium-osmium geochronology of arsenopyrite in Meguma Group gold deposits, Meguma Terrane, Nova Scotia, Canada: Evidence for multiple gold-mineralizing events, Economic Geology, v. 100, p. 1229-1242

Morelli, R.M., Bell, C.C., Creaser, R.A., and Simonetti, A., 2010, Constraints on the genesis of gold mineralization at the Homestake Gold Deposit, Black Hills, South Dakota from rhenium-osmium sulfide geochronology, Mineralium Deposita, v. 45, p. 461-480

Muchez, P., André-Mayer, A.S., El Desouky, H.A., and Reisberg, L., 2015, Diagenetic origin of the stratiform Cu-Co deposit at Kamoto in the Central African Copperbelt, Mineralium Deposita, v. 50, p. 437-447

Muchez, P., Brems, D., Clara, E., De Cleyn, A., Lammens, L., Boyce, A., De Muynck, D., Mukumba, W., and Sikazwe, O., 2010, Evolution of Cu-Co mineralizing fluids at Nkana Mine, Central African Copperbelt, Zambia, Journal of African Earth Sciences, v. 58, n. 457-474

Northrop, D.A., and Clayton, R.N., 1966, Oxygen-isotope fractionations in systems containing dolomite, The Journal of Geology, v. 74, p.174-196

O'Neil, J.R., and Epstein, S., 1966, Oxygen isotope fractionation in the system dolomite-calcite-carbon dioxide, Science, v. 152, p. 198-201

Paul, M., Reisberg, L., and Vigier, N., 2009, A new method for analysis of osmium isotopes and concentrations in surface and subsurface water samples, Chemical Geology, v. 258, p. 136-144

Pearson, D.G., and Woodland, S.J., 2000, Solvent extraction/anion exchange separation and determination of PGEs (Os, Ir, Pt, Pd, Ru) and Re–Os isotopes in geological samples by isotope dilution ICP-MS, Chemical Geology, v. 165, i. 1-2, p. 87-107

Porada, H., and Berhorst, V., 2000, Towards a new understanding of the Neoproterozoic-Early Palæzoic Lufilian and northern Zambezi Belts in Zambia and the Democratic Republic of the Congo, Journal of African Earth Sciences, v. 30, n. 3, p. 727-771

Potts, P.J., 1992, A Handbook of Silicate Rock Analysis, Blackie, Glasgow, UK, p. 622

Poty B., 1989, Geological conditions governing the use of dating methods, *In:* Roth, E., Poty, B., and Menager, M.T. (Eds), Nuclear Methods of Dating, Kluwer Academic Publishers, Dordrecht, Netherlands

Rainaud, C., Master, S., Armstrong, R.A., and Robb, L.J., 2005, Geochronology and nature of the Palaeoproterozoic basement in the Central African Copperbelt (Zambia and the Democratic Republic of Congo), with regional implications, Journal of African Earth Sciences, v. 42, p. 1-31

Richards, J.P., Cumming, G.L., Krstic, D., Wagner, P.A., and Spooner, E.T.C., 1988a, Pb isotope constraints on the age of sulfide ore deposition and U-Pb age of late uraninite veining at the Musoshi stratiform copper deposit, Central African Copper Belt, Zaire, Economic Geology, v. 83, p. 724-741

Richards, J.P., Krogh, T.E., and Spooner, E.T.C., 1988b, Fluid inclusion characteristics and U-PB rutile age of late hydrothermal alteration and veining at the Musoshi stratiform copper deposit, Central African Copper Belt, Zaire, Economic Geology, v. 83, p. 118-139

Richards, J.P., and Noble, S.R., 1998, Application of radiogenic isotope systems to the timing and origin of hydrothermal processes, *In:* Richards, J.P., and Larson, J.B., (Eds), Techniques in Hydrothermal Ore Deposits Geology, Reviews in Economic Geology, v. 10, Society of Economic Geologists, Littleton, USA

Rooney, A.D., Strauss, J.V., Brandon, A.D., and Macdonald, F.A., 2015, A Cryogenian chronology: Two long-lasting synchronous Neoproterozoic glaciations, v. 43, p. 459-462

Roy-Barman, M., 1993, Mesure du rapport $^{187}Os/^{186}Os$ dans les basaltes et péridotites: Contributionàla systematique $^{187}Re/^{186}Os$ dans le manteaux, Thesis, Univ. Paris 7

Saintilan, N.J., Selby, D., Creaser, R.A., and Dewaele, S., 2018, Sulphide Re-Os geochronology links orogenesis, salt and Cu-Co ores in the Central African Copperbelt, Nature Scientific Reports, v. 8, p. 1-8

Schmandt, D., Broughton, D., Hitzman, M.W., Plink-Bjorklund, P. Edwards, D., and Humphrey, J., 2013, The Kamoa copper district, Democratic Republic of the Congo: Stratigraphy, diagenetic and hydrothermal alteration, mineralization, Economic Geology, v. 108, p. 1301-1324

Schneider, J., Melcher, F., and Brauns, M., 2007, Concordant ages for the giant Kipushi base metal deposit (DR Congo) from direct Rb-Sr and Re-Os dating of sulfides, Mineralium Deposita, v. 42, p. 791-797

Selby, D., and Creaser, R.A., 2003, Re–Os geochronology of organic rich sediments: an evaluation of organic matter analysis methods, Chemical Geology, v. 200, I, 3-4, p. 225-240

Selley, D., and Cooke, D., 2001, Mineral zonation and sulfur isotope systematics of the Chibuluma West copper-cobalt deposit, Zambia, AMIRA P544 Progress Report, December, p. 133-169

Selley, D., Broughton, D., Scott, R., Hitzman, M., Bull, S., Large, R., McGoldrick, P., Croaker, M., and Pollington, N., 2005, A new look at the geology of the Zambian Copperbelt, Economic Geology 100th Anniversary Volume, v. 29, p. 485-522

Sharma, T., and Clayton, R.N.,1965, Measurement of O^{18}/O^{16} ratios of total oxygen of carbonates, Geochimica et Cosmochimica Acta, v. 29, p. 1347-1353

Shirey, S.B., and Walker, R.J., 1995, Carius tube digestions for low-blank rhenium–osmium chemistry analysis, Analytical Chemistry, v. 67, p. 2136-2141

Sillitoe, R.H., Perelló, J., and Garcia, A., 2010, Sulfide-bearing veinlets throughout the stratiform mineralization of the Central African Copperbelt: Temporal and genetic implications, Economic Geology, v. 105, p. 1361-1368

Sillitoe, R.H., Perelló, J, Creaser, R.A., Wilton, J., and Dawborn, T., 2015, Two ages of copper mineralization in the Mwombezhi Dome, Northwestern Zambia: Metallogenic implications for the Central African Copperbelt, Economic Geology, v. 110, p. 1917-1923

Sillitoe R.H., Perelló, J, Creaser, R.A., Wilton, J., Wilson, A.J., and Dawborn, T., 2017, Age of the Zambian Copperbelt, Mineralium Deposita, v. 52, p. 1245-1268

Stacey, J.C., and Kramers, J.D., 1975, Approximation of terrestrial lead isotope evolution by a two-stage model, Earth and Planetary Science Letters, v. 26, p. 207-221

Stein, H.J., Morgan, J.W., and Scherstén, A., 2000, Re-Os Dating of Low-Level Highly Radiogenic (LLHR) sulfides: The Harnäs Gold Deposit, Southwest Sweden, Records Continental-Scale Tectonic Events, Economic Geology, v. 95, n. 8, p. 1657-1671

Stein, H.J., Sundblad, K., Markey, R.J., Morgan, J.W., and Motuza, G., 1998, Re-Os ages for Archaen molybdenite and pyrite, Kuittila-Kivisuo, Finland and Proterozoic molybdenite, Kabeliai, Lithuania: Testing the chronometer in a metamorphic and metasomatic setting, Mineralium Deposita, v. 33, p. 329-345

Sun, W., Bennett, V.C., Eggins, S.M., Kamenetsky, V.S., and Arculus, R.J., 2003, Enhanced mantle-to-crust rhenium transfer in undegassed arc magmas, Nature, v. 422, p. 294-297

Sweeney, M.A., Binda, P.L., and Vaughn, D.J., 1991; Genesis of the ores of the Zambian Copperbelt, Ore Geology Reviews, v. 6, p. 51-76

Tatsumoto, M., Knight, R.J., Allégre, C.J., 1973, Time differences in the formation of meteorites as determined from the ratio of lead-207 to lead-206, Science, v. 180, p. 1279-1283

Taylor, H.P., 1968, The oxygen isotope geochemistry of igneous rocks, Contributions to Mineralogy and Petrology, v. 19, p. 1-71

Torrealday, H.I., Hitzman, M.W., Stein, H.J., Markley, R.J., Armstrong, R., and Broughton, D., Re-Os and U-Pb dating of the vein-hosted mineralization at the Kansanshi copper deposit, northern Zambia, Economic Geology, v. 95, p. 1165-1170

Turner, E.C., Broughton, D.W., and Brooks, T., 2018, Neoproterozoic carbonate lithofacies and ore distribution at the Kipushi Cu-Zn deposit, Democratic Republic of Congo, and Gayna River Zn Camp, Northwest Territories, Canada, Economic Geology, v. 113, p. 779-788

Van Acken, D., Su, W., Gao, J., and Creaser, R.A., 2014, Preservation of Re-Os isotope signatures in pyrite throughout low-T, high-P eclogite facies metamorphism, Terra Nova, v. 26, p. 402-407

Van Wilderode, J., Heijlen, W., De Muynck, D., Schneider, J., Vanhaecke, and Muchez, P., 2013, The Kipushi Cu-Zn deposit (DR Congo) and its host rocks: A petrographical, stable isotope (O, C) and radiogenic isotope (Sr, Nd) study, Journal of African Earth Sciences, v. 79, p. 143-156

Völkening, J., Walczyk, T., and Heumann, K.G., 1991, Osmium isotope ratio determinations by negative thermal ionization mass spectrometry, International Journal of Mass Spectrometry and Ion Processes, v. 105, p. 147-159

Voudouris, P., Melfos, V., Spry, P.G., Bindi, L., Moritz, R., Ortelli, M., and Kartal, T., 2013, Extremely Re-rich molybdenite from porphyry Cu-Mo-Au prospects in Northeastern

Greece: Mode of occurrence, causes of enrichment, and implications for gold exploration, Minerals, v. 3, p. 165-191

Vugrinovich, R.G., 1981, A distribution-free alternative to least-squares regression and its application to Rb/Sr isochron calculations, Mathematical Geology, v. 13, p. 443-454

Walker, R.J., and Morgan, J.W., 1989, Rhenium-Osmium isotope systematics of carbonaceous chondrites, Science, v. 243, n. 4890, p. 519-522

Walraven, F., and Chabu, M., 1994; Pb-isotope constraints on base-metal mineralisation at Kipushi (Southeastern Zaïre,), Journal of African Earth Sciences, v. 18, p. 73-82

Whyte, R.J., and Green, M.E., 1971, Geology and palaeogeography of Chibuluma West orebody, Zambian Copperbelt, Economic Geology, v. 66, p. 400- 424

Wilson, S.A., Ridley, W.I., and Koenig, A.E., 2002, Development of sulfide calibration standards for the laser ablation inductively-coupled plasma mass spectrometry technique, Journal of Analytical Atomic Spectrometry, v. 17, p. 406-409

Winfield, O., 1961, Chibuluma, *In:* Mendelsohn, F., (Ed), The Geology of the Northern Rhodesian Copperbelt, Macdonald, London, UK

Zartman, R.E., and Doe, B.R., 1981, Plumbotectonics, the model, Tectonophysics, v. 75, p. 135-162

Zheng, Y.F., 1999, Oxygen isotope fractionation in carbonate and sulfate minerals, Geochemical Journal, v. 33, p. 109-126

Appendix

Magnetic Separation Notes

The K_m or magnetic susceptibility of a mineral is a quantitative measure of when it "becomes" magnetic with respect to the side slope (perpendicular to grain movement), and current (I). This relationship is expressed using Appendix Equation 1 below (Flinter, 1959). As,

$$K_m = \frac{20 * sin(\alpha)}{I^2} * 10^{-6} cgs. \qquad Appendix\ EQ.1$$

For example, chalcopyrite tends to be more susceptible to magnetic fields than arsenopyrite, and it would have a higher K_m value. This means that chalcopyrite's greater Km value would become magnetic at less favorable conditions (steeper slope or lower current) than arsenopyrite (which would need either a shallower slope or a higher current to overcome gravity and enter the magnetic chute). As such, assuming operating conditions of a 9° side slope perpendicular to grain movement, and 0.6 A, the resulting Km would be 8.69E-6. Chalcopyrite and arsenopyrite have shown (in this study) to have Km values of 1.9E-5, and 4.5E-6 respectably. In this example, chalcopyrite would be magnetic as its susceptibility is greater than that from the separator, while arsenopyrite will be non-magnetic as its susceptibility is lower than the operating conditions. The most magnetic minerals (ex: magnetite) will be in the magnetic chute up until the weakest magnetic field and highest gravitational force is induced (high slope, low current), whereas the least susceptible minerals (ex: zircon) will require the greatest current and lowest slope for them to enter the magnetic chute.

For those researchers or technicians interested in maintaining a constant K_m value, but at differing operating conditions, Appendix Figure 1 may serve as a point of reference. It should be mentioned however, that for those currents in excess of 1.3 A, the relationship in Appendix Equation 1 is not accurate (Flinter, 1959). Nonetheless, K_m may be approximated for a range of operating conditions. Potential uses include when the electromagnet overheats and the desired K_m needs to be maintained for successful mineral separation. In this case, the side slope must be decreased to compensate for the reduction in current. The Km value of the magnetic field prior to decreasing the side slope may be found in Appendix Table 1. For example, if the desired mineral enters magnetic chute with a 10° side slope and current of 0.2 A, than the corresponding K_m is 8.68E-5. A similar Km (8.68E-5) is also found when a side slope of 23° and a current of 0.3 A is used.

Carbonate Dissolution Experiments

Particles in the MI light fraction contain both readily soluble carbonate, and more robust sulphide and silicate minerals. The carbonate phases are predominately composed of dolomite as both the host rock (Kakontwe Formation), and hydrothermal dolomite are present at the Kipushi deposit. Dolomite will react with HCl as expressed in the following chemical reaction,

$$(Ca,Mg)(CO_3)_2 + 4HCl \xrightarrow{80^oC} CaCl_2 + MgCl_2 + 2H_2CO_3. \qquad \textit{Appendix EQ. 2}$$

Further simplifying Equation 8.2 as the carbonic acid dissociates,

$$(Ca,Mg)(CO_3)_2 + 4HCl \xrightarrow{80^oC} CaCl_2 + MgCl_2 + 2H_2O + 2CO_2. \qquad \textit{Appendix EQ. 3}$$

The carbonate phases (mostly dolomite) were dissolved as follows;

1) Weigh 22 mL glass vial, tare

2) Weigh MI light

3) Add 0.2 N HCl in 11 mL/100 mg carbonate ratio (ex: for 150 mg carbonate use 16.5 ml 0.2 N HCl) to 22 mL vial, cap, place on hotplate for ~16 hours at 80°C

4) Decant solution into 50 mL centrifuge vial and centrifuge

5) Remove excess HCl with fine-tip pipette (leaving undissolved material in 50 mL vial)

6) Rinse undissolved material in 50 mL vial with MQ back into 22 mL vial

7) Dry undissolved material in 22 mL vial, weigh

8) Undissolved material mass = pre-dissolution mass – post-dissolution mass

The results are provided in Appendix Table 2. For 12 experimental runs, a total of 25.00 mg was recovered from 1950 mg, or a ~1.28 % yield. While the % yield for these samples is very low and time consuming, for those MI light fractions that are either less carbonate or more sulphide, higher yields may be possible. Additionally, it may serve as a useful screening procedure to remove carbonate or phosphate minerals prior to magnetic separation.

Pairwise Elemental Correlation

While this procedure may (and was) applied to a series of elements, Re and Mo are used throughout as an example. In short, this procedure determined the percentage that one discrete location in the 1mm^2 ROI contained both Re and Mo. More precisely, for any cell (the smallest packet of raw data, each cell is assigned to a single location along a raster) containing either Re or Mo at a cps greater than the mean background value, is considered valid. Cells are invalid and ignored if neither Re nor Mo are found at a cps greater than the mean background value. For cells containing both Re and Mo at cps greater than the mean background value, a "hit" is counted. More simply,

$$if\, cell_n(cps) > \bar{E}(cps) \rightarrow hit.$$

The probability (P) % is the ratio of the total number of hits to the total number of valid Re (ex: Re_v) and Mo cells. That is,

$$P = \frac{\sum hit}{\sum Re_v + \sum Mo_v} * 100\% \qquad \textit{Appendix EQ 4}$$

Equation 8.6 is a measure of the likelihood that both Re and Mo are found together. At P = 100 %, every cell contains both elements above the set threshold. The threshold may be a background subtraction, or σ_n above the mean background. A clear relationship between σ_n and P is exists (Figure 4.4), as P decreases exponentially as σ_n increases. This is likely caused by the dramatic decrease in valid cells-and by extension, hits-as the threshold (or confidence) is increased. In other words, for trace elements, such as Mo and Re, the probability that both are located in the same cell diminish due to their relative rarity, especially when compared together (ex: Re:Mo).

References

Flinter, B.H., 1959, The magnetic separation of some alluvial minerals in Malaya, American Mineralogist, v. 44, p. 738-751

Current (A)																			
More Favorable Conditions →																			
Least Magnetic Minerals →																			
0.1	0.2	0.3	0.4	0.5	0.6	0.7	0.8	0.9	1.0	1.1	1.2	1.3	1.4	1.5	1.6	1.7	1.8	1.9	2.0

Slope ⊥ to grain movement	**Less Favorable Conditions ↓**	**Most Magnetic Minerals ↓**	1
			2
			3
			4
			5
			6
			7
			8
			9
			10
			11
			12
			13
			14
			15
			16
			17
			18
			19
			20
			21
			22
			23
			24
			25
			26
			27
			28
			29
			30
			31
			32
			33
			34
			35

3.5E-05	8.7E-06	3.9E-06	2.2E-06	1.4E-06	9.7E-07	7.1E-07	5.5E-07	4.3E-07	3.5E-07
7.0E-05	1.7E-05	7.8E-06	4.4E-06	2.8E-06	1.9E-06	1.4E-06	1.1E-06	8.6E-07	7.0E-07
1.0E-04	2.6E-05	1.2E-05	6.5E-06	4.2E-06	2.9E-06	2.1E-06	1.6E-06	1.3E-06	1.0E-06
1.4E-04	3.5E-05	1.6E-05	8.7E-06	5.6E-06	3.9E-06	2.8E-06	2.2E-06	1.7E-06	1.4E-06
1.7E-04	4.4E-05	1.9E-05	1.1E-05	7.0E-06	4.8E-06	3.6E-06	2.7E-06	2.2E-06	1.7E-06
2.1E-04	5.2E-05	2.3E-05	1.3E-05	8.4E-06	5.8E-06	4.3E-06	3.3E-06	2.6E-06	2.1E-06
2.4E-04	6.1E-05	2.7E-05	1.5E-05	9.7E-06	6.8E-06	5.0E-06	3.8E-06	3.0E-06	2.4E-06
2.8E-04	7.0E-05	3.1E-05	1.7E-05	1.1E-05	7.7E-06	5.7E-06	4.3E-06	3.4E-06	2.8E-06
3.1E-04	7.8E-05	3.5E-05	2.0E-05	1.3E-05	8.7E-06	6.4E-06	4.9E-06	3.9E-06	3.1E-06
3.5E-04	8.7E-05	3.9E-05	2.2E-05	1.4E-05	9.6E-06	7.1E-06	5.4E-06	4.3E-06	3.5E-06
3.8E-04	9.5E-05	4.2E-05	2.4E-05	1.5E-05	1.1E-05	7.8E-06	6.0E-06	4.7E-06	3.8E-06
4.2E-04	1.0E-04	4.6E-05	2.6E-05	1.7E-05	1.2E-05	8.5E-06	6.5E-06	5.1E-06	4.2E-06
4.5E-04	1.1E-04	5.0E-05	2.8E-05	1.8E-05	1.2E-05	9.2E-06	7.0E-06	5.6E-06	4.5E-06
4.8E-04	1.2E-04	5.4E-05	3.0E-05	1.9E-05	1.3E-05	9.9E-06	7.6E-06	6.0E-06	4.8E-06
5.2E-04	1.3E-04	5.8E-05	3.2E-05	2.1E-05	1.4E-05	1.1E-05	8.1E-06	6.4E-06	5.2E-06
5.5E-04	1.4E-04	6.1E-05	3.4E-05	2.2E-05	1.5E-05	1.1E-05	8.6E-06	6.8E-06	5.5E-06
5.8E-04	1.5E-04	6.5E-05	3.7E-05	2.3E-05	1.6E-05	1.2E-05	9.1E-06	7.2E-06	5.8E-06
6.2E-04	1.5E-04	6.9E-05	3.9E-05	2.5E-05	1.7E-05	1.3E-05	9.7E-06	7.6E-06	6.2E-06
6.5E-04	1.6E-04	7.2E-05	4.1E-05	2.6E-05	1.8E-05	1.3E-05	1.0E-05	8.0E-06	6.5E-06
6.8E-04	1.7E-04	7.6E-05	4.3E-05	2.7E-05	1.9E-05	1.4E-05	1.1E-05	8.4E-06	6.8E-06
7.2E-04	1.8E-04	8.0E-05	4.5E-05	2.9E-05	2.0E-05	1.5E-05	1.1E-05	8.8E-06	7.2E-06
7.5E-04	1.9E-04	8.3E-05	4.7E-05	3.0E-05	2.1E-05	1.5E-05	1.2E-05	9.2E-06	7.5E-06
7.8E-04	2.0E-04	8.7E-05	4.9E-05	3.1E-05	2.2E-05	1.6E-05	1.2E-05	9.6E-06	7.8E-06
8.1E-04	2.0E-04	9.0E-05	5.1E-05	3.3E-05	2.3E-05	1.7E-05	1.3E-05	1.0E-05	8.1E-06
8.5E-04	2.1E-04	9.4E-05	5.3E-05	3.4E-05	2.3E-05	1.7E-05	1.3E-05	1.0E-05	8.5E-06
8.8E-04	2.2E-04	9.7E-05	5.5E-05	3.5E-05	2.4E-05	1.8E-05	1.4E-05	1.1E-05	8.8E-06
9.1E-04	2.3E-04	1.0E-04	5.7E-05	3.6E-05	2.5E-05	1.9E-05	1.4E-05	1.1E-05	9.1E-06
9.4E-04	2.3E-04	1.0E-04	5.9E-05	3.8E-05	2.6E-05	1.9E-05	1.5E-05	1.2E-05	9.4E-06
9.7E-04	2.4E-04	1.1E-04	6.1E-05	3.9E-05	2.7E-05	2.0E-05	1.5E-05	1.2E-05	9.7E-06
1.0E-03	2.5E-04	1.1E-04	6.3E-05	4.0E-05	2.8E-05	2.0E-05	1.6E-05	1.2E-05	1.0E-05
1.0E-03	2.6E-04	1.1E-04	6.4E-05	4.1E-05	2.9E-05	2.1E-05	1.6E-05	1.3E-05	1.0E-05
1.1E-03	2.6E-04	1.2E-04	6.6E-05	4.2E-05	2.9E-05	2.2E-05	1.7E-05	1.3E-05	1.1E-05
1.1E-03	2.7E-04	1.2E-04	6.8E-05	4.4E-05	3.0E-05	2.2E-05	1.7E-05	1.3E-05	1.1E-05
1.1E-03	2.8E-04	1.2E-04	7.0E-05	4.5E-05	3.1E-05	2.3E-05	1.7E-05	1.4E-05	1.1E-05
1.1E-03	2.9E-04	1.3E-04	7.2E-05	4.6E-05	3.2E-05	2.3E-05	1.8E-05	1.4E-05	1.1E-05

2.9E-07	2.4E-07	2.1E-07	1.8E-07	1.6E-07	1.4E-07	1.2E-07	1.1E-07	9.7E-08	8.7E-08
5.8E-07	4.8E-07	4.1E-07	3.6E-07	3.1E-07	2.7E-07	2.4E-07	2.2E-07	1.9E-07	1.7E-07
8.7E-07	7.3E-07	6.2E-07	5.3E-07	4.7E-07	4.1E-07	3.6E-07	3.2E-07	2.9E-07	2.6E-07
1.2E-06	9.7E-07	8.3E-07	7.1E-07	6.2E-07	5.4E-07	4.8E-07	4.3E-07	3.9E-07	3.5E-07
1.4E-06	1.2E-06	1.0E-06	8.9E-07	7.7E-07	6.8E-07	6.0E-07	5.4E-07	4.8E-07	4.4E-07
1.7E-06	1.5E-06	1.2E-06	1.1E-06	9.3E-07	8.2E-07	7.2E-07	6.5E-07	5.8E-07	5.2E-07
2.0E-06	1.7E-06	1.4E-06	1.2E-06	1.1E-06	9.5E-07	8.4E-07	7.5E-07	6.8E-07	6.1E-07
2.3E-06	1.9E-06	1.6E-06	1.4E-06	1.2E-06	1.1E-06	9.6E-07	8.6E-07	7.7E-07	7.0E-07
2.6E-06	2.2E-06	1.9E-06	1.6E-06	1.4E-06	1.2E-06	1.1E-06	9.7E-07	8.7E-07	7.8E-07
2.9E-06	2.4E-06	2.1E-06	1.8E-06	1.5E-06	1.4E-06	1.2E-06	1.1E-06	9.6E-07	8.7E-07
3.2E-06	2.7E-06	2.3E-06	1.9E-06	1.7E-06	1.5E-06	1.3E-06	1.2E-06	1.1E-06	9.5E-07
3.4E-06	2.9E-06	2.5E-06	2.1E-06	1.8E-06	1.6E-06	1.4E-06	1.3E-06	1.2E-06	1.0E-06
3.7E-06	3.1E-06	2.7E-06	2.3E-06	2.0E-06	1.8E-06	1.6E-06	1.4E-06	1.2E-06	1.1E-06
4.0E-06	3.4E-06	2.9E-06	2.5E-06	2.2E-06	1.9E-06	1.7E-06	1.5E-06	1.3E-06	1.2E-06
4.3E-06	3.6E-06	3.1E-06	2.6E-06	2.3E-06	2.0E-06	1.8E-06	1.6E-06	1.4E-06	1.3E-06
4.6E-06	3.8E-06	3.3E-06	2.8E-06	2.5E-06	2.2E-06	1.9E-06	1.7E-06	1.5E-06	1.4E-06
4.8E-06	4.1E-06	3.5E-06	3.0E-06	2.6E-06	2.3E-06	2.0E-06	1.8E-06	1.6E-06	1.5E-06
5.1E-06	4.3E-06	3.7E-06	3.2E-06	2.7E-06	2.4E-06	2.1E-06	1.9E-06	1.7E-06	1.5E-06
5.4E-06	4.5E-06	3.9E-06	3.3E-06	2.9E-06	2.5E-06	2.3E-06	2.0E-06	1.8E-06	1.6E-06
5.7E-06	4.8E-06	4.0E-06	3.5E-06	3.0E-06	2.7E-06	2.4E-06	2.1E-06	1.9E-06	1.7E-06
5.9E-06	5.0E-06	4.2E-06	3.7E-06	3.2E-06	2.8E-06	2.5E-06	2.2E-06	2.0E-06	1.8E-06
6.2E-06	5.2E-06	4.4E-06	3.8E-06	3.3E-06	2.9E-06	2.6E-06	2.3E-06	2.1E-06	1.9E-06
6.5E-06	5.4E-06	4.6E-06	4.0E-06	3.5E-06	3.1E-06	2.7E-06	2.4E-06	2.2E-06	2.0E-06
6.7E-06	5.6E-06	4.8E-06	4.2E-06	3.6E-06	3.2E-06	2.8E-06	2.5E-06	2.3E-06	2.0E-06
7.0E-06	5.9E-06	5.0E-06	4.3E-06	3.8E-06	3.3E-06	2.9E-06	2.6E-06	2.3E-06	2.1E-06
7.2E-06	6.1E-06	5.2E-06	4.5E-06	3.9E-06	3.4E-06	3.0E-06	2.7E-06	2.4E-06	2.2E-06
7.5E-06	6.3E-06	5.4E-06	4.6E-06	4.0E-06	3.5E-06	3.1E-06	2.8E-06	2.5E-06	2.3E-06
7.8E-06	6.5E-06	5.6E-06	4.8E-06	4.2E-06	3.7E-06	3.2E-06	2.9E-06	2.6E-06	2.3E-06
8.0E-06	6.7E-06	5.7E-06	4.9E-06	4.3E-06	3.8E-06	3.4E-06	3.0E-06	2.7E-06	2.4E-06
8.3E-06	6.9E-06	5.9E-06	5.1E-06	4.4E-06	3.9E-06	3.5E-06	3.1E-06	2.8E-06	2.5E-06
8.5E-06	7.2E-06	6.1E-06	5.3E-06	4.6E-06	4.0E-06	3.6E-06	3.2E-06	2.9E-06	2.6E-06
8.8E-06	7.4E-06	6.3E-06	5.4E-06	4.7E-06	4.1E-06	3.7E-06	3.3E-06	2.9E-06	2.6E-06
9.0E-06	7.6E-06	6.4E-06	5.6E-06	4.8E-06	4.3E-06	3.8E-06	3.4E-06	3.0E-06	2.7E-06

9.2E-06	7.8E-06	6.6E-06	5.7E-06	5.0E-06	4.4E-06	3.9E-06	3.5E-06	3.1E-06	2.8E-06
9.5E-06	8.0E-06	6.8E-06	5.9E-06	5.1E-06	4.5E-06	4.0E-06	3.5E-06	3.2E-06	2.9E-06

Appendix Table 1: Calculated K_m values for a range of typical side slopes and currents. The grayscale is proportional to the K_m value, that is, higher $K_m \propto$ darker hue.

Sample name	Initial mass (g)	Volume HCl added (mL)	Non-carbonate mass (g)	% Non-carbonate	% Carbonate	Running total of mass not dissolved (mg)
KPU-081/557.3-Mil-1	0.16	17.6	0.00295	1.8	98.2	5.73
KPU-081/557.3-Mil-2	0.16	17.6	0.00164	1.0	99.0	7.37
KPU-081/557.3-Mil-3	0.17	18.7	0.00247	1.5	98.5	9.84
KPU-081/557.3-Mil-4	0.17	18.7	0.00136	0.8	99.2	11.20
KPU-081/557.3-Mil-5	0.19	20.9	0.00289	1.5	98.5	14.09
KPU-081/557.3-Mil-6	0.16	17.2	0.00104	0.7	99.3	15.13
KPU-081/557.3-Mil-7	0.15	17.0	0.00170	1.1	98.9	16.87
KPU-081/557.3-Mil-8	0.16	17.5	0.00168	1.1	98.9	18.55
KPU-081/557.3-Mil-9	0.15	16.7	0.00187	1.2	98.8	20.42
KPU-081/557.3-Mil-10	0.17	18.4	0.00201	1.2	98.8	22.43
KPU-081/557.3-Mil-11	0.16	18.0	0.00257	1.6	98.4	25.00

Appendix Table 2: Carbonate dissolution experiment data.